Dipartimento di Fisica, Università degli Studi di Milano
Laboratoire Kastler Brossel, Université Pierre et Marie Curie

Phd thesis to obtain the title of Dottore di ricerca in Fisica, Astrofisica e Fisica Applicata
and the title of Docteur de l'Université Pierre et Marie Curie

Experimental Study of Nanocrystals as Single Photon Sources

Stefano Vezzoli

UNIVERSITÀ DEGLI STUDI DI MILANO

UPMC SORBONNE UNIVERSITÉS

Laboratoire Kastler Brossel
Physique quantique et applications

UNIVERSITÉ FRANCO ITALIENNE | UNIVERSITÀ ITALO FRANCESE

Defended on July 12, 2013

Jury:
Francesco Marin, Reviewer
Jean-Philippe Poizat, Reviewer
Agnès Maître, Examinator
Alberto Vailati, Examinator
Alberto Bramati, Ph. D. Advisor
Simone Cialdi, Ph. D. Advisor

Abstract Wet-chemically synthesized colloidal nanocrystals are promising single photon emitters at room temperature, due to the strong quantum confinement induced by the small dimensions. However, their applications have been so far limited by two main drawbacks: the blinking of their photo-luminescence and a non-polarized emission. This manuscript is consecrated to the study of the optical properties of a particular type of colloidal nanocrystals, called dot-in-rod (DR), in which a spherical CdSe core is surrounded by a rod-like CdS shell. We demonstrate for the first time a suppression of the blinking in thick shell DRs. In contrast to spherical nanocrystals, we show that it can be obtained while keeping a good quality of the single photon emission and a high degree of linear polarization. A complete room-temperature characterization of the optical, and especially quantum optical, properties of DRs is provided for several geometrical parameters. In particular, an original approach, based on an ensemble photoluminescence measurement, is developed to assess the quality of a sample of nanocrystals as single photon sources. By studying single DRs in a confocal microscope, we analyze the influence of the core size and of the shell thickness and length on the photon anti-bunching, radiative lifetime and polarization of the emission. This systematic study brings a contribution to the understanding of the interaction processes of the confined carriers in semiconductor nanocrystals. The interplay of radiative and non-radiative recombinations and, in particular, the role of the Auger effect in the photo-luminescence blinking and in the emission of non-classical light are deeply investigated. **Key words**: nanocrystals, quantum dots, semiconductor, single photon source, photo-luminescence blinking, quantum information

Résumé Les nanocristaux colloïdaux synthétisés par voie chimique sont des émetteurs de photons uniques très prometteurs à température ambiante, grâce au fort confinement quantique induit par leur petite taille. Toutefois, leurs applications ont été jusqu'ici limitées par deux problèms: le scintillement de leur photo-luminescence et l'émission non polarisée. Ce manuscrit est consacré à l'étude des propriétés optiques d'un nouveau type de nanocristaux colloïdaux, appelés dots-in-rod (DR), dans lequels un cœur sphérique de CdSe est entouré par une coquille de CdS en forme de cylindre. Nous démontrons pour la première fois une suppression du scintillement dans des DRs à la coquille épaisse. Contrairement aux nanocristaux sphériques, nous montrons que cette suppression peut être obtenue tout en conservant une bonne qualité de l'émission de photons uniques et un degré de polarisation linéaire très elévé. Une caractérisation complète des propriétés optiques et optique quantique des DRs est réalisée à température ambiante pour différents paramètres géométriques. En particulier, nous avons développé une technique originale pour évaluer la qualité d'un échantillon de nanocristaux comme sources de photons uniques, basée sur une mesure de photo-luminescence d'ensemble. Grâce à une étude en microscopie confocale des DRs l'echelle individuelle, nous avons analysé l'influence de la taille du cœur et de l'épaisseur de la coquille et de sa longueur sur les propriétés de dégroupement des photons, de durée de vie radiative et de polarisation de l'émission. Cette étude systématique apporte une contribution à la compréhension des processus d'interaction entre les porteurs confinés dans les nanocristaux semi-conducteurs. L'interaction entre les recombinaisons radiative et non radiative et, en particulier, le rôle de l'effet Auger dans le scintillement de la photo-luminescence et dans l'émission de lumière non-classique sont étudiés en détail. **Mots-clés**: nanocristaux, quantum

dot, semiconducteurs, photons uniques, photo-luminescence, information quantique

Prefazione I nanocristalli colloidali sintetizzati chimicamente sono dei promettenti emettitori di singolo fotone a temperatura ambiente, grazie al forte confinamento quantistico indotto dalle piccole dimensioni. Tuttavia la loro applicazione è stata finora limitata da due problemi principali: lintermittenza (*blinking*) della foto-luminescenza e un'emissione di luce non polarizzata. Questo manoscritto è dedicato allo studio delle proprietà ottiche di un particolare tipo di nanocristalli colloidali, detto *dot-in-rod* (DR), in cui un *core* sferico di CdSe è circondato da una *shell* di CdS di forma cilindrica. Una riduzione del blinking in DR di shell spessa è dimostrata in questa tesi per la prima volta. Rispetto ai nanocristalli di forma sferica, tale riduzione pu essere ottenuta mantenendo una buona qualità dell'emissione a singolo fotone e un alto grado di polarizzazione lineare. Una caratterizzazione completa a temperatura ambiente delle proprietà ottiche e quantistiche è realizzata per DR con diverse caratteristiche geometriche. In particolare, abbiamo sviluppato un approccio originale per valutare la qualità di un campione di nanocristalli come sorgenti a singolo fotone, basato su una misura d'insieme della foto-luminescenza. Attraverso uno studio su singoli DR in microscopia confocale, viene analizzata l'influenza della dimensione del core e dello spessore e della lunghezza della shell sui tempi di vita radiativi, sulla polarizzazione e sulle proprietá quantistiche della luce emessa. Questo studio sistematico apporta un contributo alla comprensione dei processi di interazione dei portatori di carica confinati nei nanocristalli semiconduttori. L'interazione fra i canali di ricombinazione radiativa e non radiativa e, in particolare, il ruolo dell'effetto Auger nel blinking della foto-luminescenza e nell'emissione di luce non classica sono ampiamente discussi. **Parole chiave**: nanocristalli, quantum dot, semiconduttori, singoli fotoni, foto-luminescenza, informazione quantistica

Contents

Introduction

Historical and scientific context of colloidal semiconductor nanocrystals During the last 30 years many materials have been scaled down to the nano-scale level. This exceptional technological progress has lead, among many other things, to systems where the charge carriers can be 3-dimensionally confined, the so called quantum dots (QDs). These structures, although made of thousands of atoms, are characterized by discrete energy levels, like individual atoms, and they are often referred to as artificial atoms. Like new artificial atoms, their physico-chemical properties can be very different from those of the bulk material they are made of and often such properties can be widely tuned by choosing the size, shape and surface of the nano-structures.
We will focus on semiconductor QDs, because of their interesting size-dependent optical and quantum optical properties. Of course there are many kinds of QDs, for example metallic nano-particles. Also in this case new properties emerge with respect to the bulk material, like size-dependent plasmonic resonances.
Until the late 90s, one of the most spread and performing methods for building QDs was the Stransky-Krastanov (SK) epitaxial growth, also known as 'layer-plus-islands-growth'. It is the spontaneous nucleation of islands of an original layer of semiconductor (i.e. InAs) deposited on a substrate of another material (i.e. GaAs), due to the lattice constant mismatch between the two crystalline materials. These self-assembled structures are usually pyramidal or lens shaped, with a lateral size in the range of 10-20 nm and vertical dimensions of few nanometers.

Another class of QDs are the colloidal semiconductor nanocrystals, which are synthesized by wet-chemistry methods. The colloidal synthesis of the nanocrystals is based on the classical theory of the nucleation. Its history goes back to the Middle-Age, where it was exploited for the fabrication of colored glasses, the ancestors of modern glass filters (Corning and Schott filters). The glass acts like a very viscous solvent where the atoms (Cadmium or Selenium atoms for instance) diffuse and can form seeds, followed by the growth of crystalline nano-structures. The first researches about the crystalline growth of II/VI semiconductors in a glass matrix were carried on by Efros and Ekimov in the early 80s [1], followed by the groups of L. Brus, P. Alivisatos, M. Bawendi and P. Guyot-Sionnest.
At the beginning, the colloidal synthesis of nanocrystals was limited to inorganic solutions of glass or sol-gels, but in the 90s, new methods of fabrications in organic solutions boosted the development of this field. In fact, colloidal nanocrystals synthesized in a liquid solvent can be easily manipulated by the traditional methods of molecular chemistry: they can be transferred from one solvent to another, embedded in different materials (from natural structures like cells to artificial photonic structures) or diluted in order to be observed individually.

A colloidal QD is thus a semiconductor nanocrystal stabilized by a layer of organic ligands adsorbed to its surface, which assures a colloidal suspension. Since the first organo-metallic synthesis in 1993 [2], many efforts were devoted to develop new fabrication techniques in order to obtain ensembles of nanocrystals of controlled size, shape, dispersion and crystallinity. Currently, nanocrystals of many different shapes and configurations are realized: spheres, rods, tetrapods, core/shell structures, dot-in-rods,...
Among the most studied materials for colloidal QDs, at least in terms of optical properties, there is CdSe (Cadmium Selenide). CdSe nanocrystals can emit photons in almost all the visible spectrum (from 450 to 700 nm), their size can be adjusted with a precision up to about 5% and it is very homogeneous within the ensemble; their emission quantum efficiency is very high and their surface can be easily treated; this is why they are on the market already since 2002.

Being synthesized using wet-chemistry, nanocrystals are free-standing structures dispersed in solution. Therefore, they can be produced in large quantities in a reaction flask and can then be transferred to any desired substrate. Moreover, due to their cheap, easy and high throughput synthesis, the colloidal nanocrystals are highly versatile nano-particles allowing to arbitrarily engineering the grown structure according to the requested optical properties. Thanks to all these characteristics, the nanocrystals have found many applications. The richness of available methods for treating their surface allowed an effective coupling with organic materials, which lead to very bright electroluminescent diodes [3]. The possibility to functionalize the surface, together with their room-temperature stability, has made colloidal QDs among the most used fluorescent markers for biological applications, ranging from multi-color imaging of tissues [4], to tracking of single macro-molecules [5], to tumoral cell targeting [6]. In the field of the optoelectronics, laser emission from self-assembled structures of nanocrystals were reported [7]. This suggest that an ensemble of well organized nanocrystals can provide a very high gain medium for a low threshold laser. In fact, the separation between the discrete energy levels allows to avoid the depopulation of the emission level by thermal activation. For a recent review of the possible applications of colloidal nanocrystals we refer to [9].

In the field of quantum optics, the quantum confinement of the charge carriers in colloidal nanocrystals is responsible for the emission of non-classical light, like bright single photon fluxes or pairs of entangled photons. In the 90s the first studies on single, isolated nanoparticles revealed many new and unexpected effects, which were first hidden in ensemble measurements by time averaging and size inhomogeneities. Some of these new properties, like the photoluminescence fluctuations (blinking) or spectral diffusion confirmed the importance of the surface in nanocrystals, and of its interactions with the environment. Other properties, like the emission of non-classical light or ultra thin spectra at low temperature, reinforced the analogy between quantum confined systems and single atoms. The coupling of single nanocrystal QDs and photonic crystals was demonstrated in 2004 [8]. The possibility to control the interaction between quantum states of light in a cavity and electron-hole states in a single nanocrystal relies on their tunable emission wavelength, their electronic discrete levels and their easiness of manipulation.

Nanocrystals as single photon sources In the past few years, the deterministic generation of single photons on demand has become a field of huge interest for potential applications. The development of reliable sources of quantum light is a major challenge for the field of quantum information, including quantum communication, computing and metrology. Several quantum information protocols are based on the properties of single photons and cannot be achieved with classical light. Such applications include single photon-based quantum cryptography that ensures inviolable exchange of information exploiting the fundamental laws of quantum mechanics. Other promising fields are quantum computation and quantum simulation, where quantum mechanics allows in principle solving hard problems for classical computing. Furthermore, on-demand sources of single- and few-photon number states are required for certain types of photonic quantum logic gates and quantum metrology.

In past years several materials have been suggested as promising single photon emitters. Across 1977 and 1986 isolated mercury, sodium and barium atoms were demonstrated to be able to emit anti-bunched photon fluxes [10]. Single atoms and ions are expensive, difficult to manage and require cryogenic temperatures. An alternative to single atoms are single molecules, and several works have been carried out in past years [11]. The molecules can be easily photo-damaged and they usually photo-bleach in minutes. A robust system to emit single photons at room temperature is provided by individual nitrogen-vacancies in bulk diamond and diamond nanocrystals [12]. This kind of sources are usually limited by the maximal photon flux rate which can be provided, by the fact that the emitted light is not polarized. Also Stransky-Krastanov epitaxial quantum dots are promising nanostuctures for the realization of single photon devices. The large dimension (10-20 nm) and the irregular shape do not allow SK QDs to be single photon emitters at room temperature, due to the low distance between the confined energy states. However, it is well known that they are able to generate stable flux of single photons at cryogenic temperatures.

As already mentioned, the StranskyKrastanov grown QDs are still limited by the operating temperature, far from 300 K [13]. On the other hand, wet-chemically synthesized colloidal core/shell nanocrystals (NCs) are promising single photon emitters for room temperature applications, due to the well separated quantum energy states, the low cost synthesis, the broad tunable emission range, the high quantum efficiency.

The carrier-carrier interactions in colloidal NCs are enhanced by virtue of the strong quantum confinement induced by the small dimensions and this fact is mainly responsible of the single photon emission at room temperature. NCs are cheap to synthesize, easy-to-handle, they show a broad tunable emission range and a high quantum efficiency and they can be easily coupled to other nano-structures or optical cavities in order to improve their emission properties and the collection of light.

After the first demonstration of photon antibunching from a CdSe/ZnS core/shell nanostructure [18], the research activity on colloidal semiconductor nanocrystals has been focused on overcoming several drawbacks experienced by these nanoparticles, such as blinking [19], spectral diffusion [20] and unpolarized emission.

Recent works on the semiconductor nanocrystal synthesis have demonstrated that it is possible to overcome these limitations by properly engineering the nanocrystals band structure by care-

fully controlling their shape and size. In particular Malher and co-workers [21] demonstrated that by growing a giant spherical CdS shell around a CdSe nanocrystal it is possible to strongly reduce the blinking phenomenon. However, this blinking suppression was accompanied by a worse quality of the single photon emission.

Another limiting feature of spherical colloidal nanocrystals is that their light emission is not linearly polarized [14] [15]. To achieve well polarized single-photon emission, a new type of nanocrystal has been proposed recently [16], which is based on an asymmetric core/shell CdSe/CdS dot in a rod (DR). Due to their elongated cylindrical shape, these structures have an optical dipole oriented along the cylinder and therefore emit photons with a good degree of linear polarization.
DRs were shown to emit single polarized photons for the first time by our group [17] in LKB in Paris. However these first samples were still affected by the problem of blinking, since they were characterized by a thin shell.

Subject of this thesis In this thesis we will show how blinking can be suppressed in semiconductor DRs. We will also study the influence of the core size and of the shell thickness and length on the DRs properties of single photon emission, lifetime and polarization of the emission.

The first chapter of this thesis reviews the theoretical background of colloidal nanocrystals, focussing on the optical properties which emerge from the strong quantum confinement. In particular, DRs heterostructures and their specific features are introduced.

In the second chapter we address two phenomena which are a signature of single nanocrystals: the photo-luminescence fluctuations (blinking) and the emission of non classical states of light. These two phenomena are carefully discussed, as well as the experimental tools for their characterization.
We also review the basic principles of confocal microscopy and time correlated single photon counting, which are widely used for the optical study of single nanocrystals.

The third chapter is devoted to the experimental characterization of different kinds of DRs. General properties like photo-luminescence spectra, quantum yield, photo-stability, lifetime, polarization of the emission will be carefully assessed for several combinations of core and shell size. In some cases an original experimental approach has been developed.
By carefully investigating the properties of nanocrystals as a function of their geometrical parameters, we want to select the best candidate for a room temperature, bright and stable single photon source.
This systematic study also brings a contribution to the understanding of the interaction processes of the electrons and the holes in semiconductor nanocrystals.

Chapter 1

Colloidal Nanocrystals: a review

Quantum confinement in semiconductors

Even if the most important properties of bulk crystalline materials are well understood from solid-state physics, when dimensions are reduced to the nano-scale, new, size-dependent properties emerge from the quantum confinement.

Because of their wave-particle nature, electrons in a solid are treated as particles with an effective mass m^* (accounting for the crystal potential)and a linear momentum arising from their wave-like nature $p = \hbar k = h/\lambda$ (λ is the deBroglie wavelength). Because of this wave-like nature the behavior of an electron is very sensitive to the solid dimension.

When the electrons motion in a solid crystal is limited in a volume of the order of λ^3, the electrons start to 'feel' the borders and their energy spectrum is dramatically modified. The quantum confinement changes the density of energy states (DOS), defined as the density of allowed states for a given energy E. Fig. 1.1 schematically illustrates the changes in the density of states from the bulk to one, two or three dimensions electron confinement. This creates different types of structures known as quantum wells (electrons free to move in a plane), quantum wires (electrons confined in two directions), and quantum dots (electrons confined along the three cartesian axes).

A quantum dot (QD) is thus a 3-dimensionally confined system and in this case the quasi-continuous distribution of states collapses into a series of Dirac functions, i.e. the energy levels becomes discrete, like in single atoms (atom-like electronic structure).

Quantum Confinement regimes of the excitons

The 3-dimensional quantum confinement in a QD implies a size-dependent behavior.

In a semiconductor QD the energy gap is the separation between the lowest unoccupied electronic state (conduction band) and the highest occupied state (valence band) at T=0 K. The exciton band gap is given by:

$$E_g = E_{g0} + E_q + E_C$$

E_{g0} is the bulk band gap, E_q the contribution of the confinement (zero-point energy):

$$E_q = \frac{\hbar^2 \pi^2}{2m_e^* a^2} + \frac{\hbar^2 \pi^2}{2m_h^* a^2}$$

where a is the QD diameter and $m^*_{e,h}$ the electron (hole) effective masses. E_C is the contribution of the Coulomb attraction between electrons and holes. It is useful to introduce the concept of (Wannier-Mott) *exciton*, the quasi-particle formed by an electron and a hole state.
In spherical QDs E_C can be estimated (as a first approximation) as [22]:

$$E_C = -1.8\frac{\hbar^2}{\mu r_B a}$$

where $r_B = \frac{\hbar^2\epsilon^2}{\mu e^2}$ is the Bohr radius of the exciton, being μ the reduced mass of the exciton and ϵ the dielectric constant. Therefore, by considering all contributions, the energy gap is given by:

$$E_g = E_{g_0} + \frac{\hbar^2\pi^2}{2m^*_e a^2} + \frac{\hbar^2\pi^2}{2m^*_h a^2} - 1.8\frac{\hbar^2}{\mu r_B a}$$

Coulomb interactions scale with the dimension of the system as $\frac{1}{a}$, while confinement energy as $\frac{1}{a^2}$.

Two regimes can be distinguished, depending on the dimension of the system with respect to the Bohr radius. The Bohr radius of the exciton represents its spatial extension and ranges from few nm to tens of nm (it is 5.6 nm in CdSe).

If $a > r_B$ the confinement effects are perturbative, this is called weak confinement, and it is typical of Stranski-Krastanov epitaxial dots, described in the introduction.
Colloidal nanocrystals (NCs) are usually in the opposite regime which is called *strong confinement* and in this case the Coulomb interaction is treated as a perturbation in computing the energy levels. Typical radii are between 1 and 3 nm.

The fluorescence of a semiconductor quantum dot comes from the relaxation of an excited electron to the ground state combining with the hole. Due to quantum confinement effects, the energy of the emitted photon is determined by the size of the QD.

1.1 Electronic structure of CdSe nanocrystals

In order to understand the optical properties of nanocrystals, it is necessary to understand their electronic structure.

Among the most studied materials for colloidal QDs there is CdSe, especially because these nanocrystals can emit photons on almost all the visible spectrum (from 450 to 700 nm). CdSe nanocrystals have become a model system, both for the fundamental understanding and applications (see also the introduction).

Method of the envelope function Here we refer to CdSe spherical NCs but this model applies to any other material with hexagonal crystallographic structure (wurtzite), and can be extended in the case of cylinder (nano-rods). In our experiments we will use wurtzite nanocrystals, but other structures like Zinc-Blend can be studied using the same approach [23].

Most of the models of the electronic structure in nanocrystals rely on the effective mass approximation, based on the method of the envelope function. The electron or hole wavefunctions

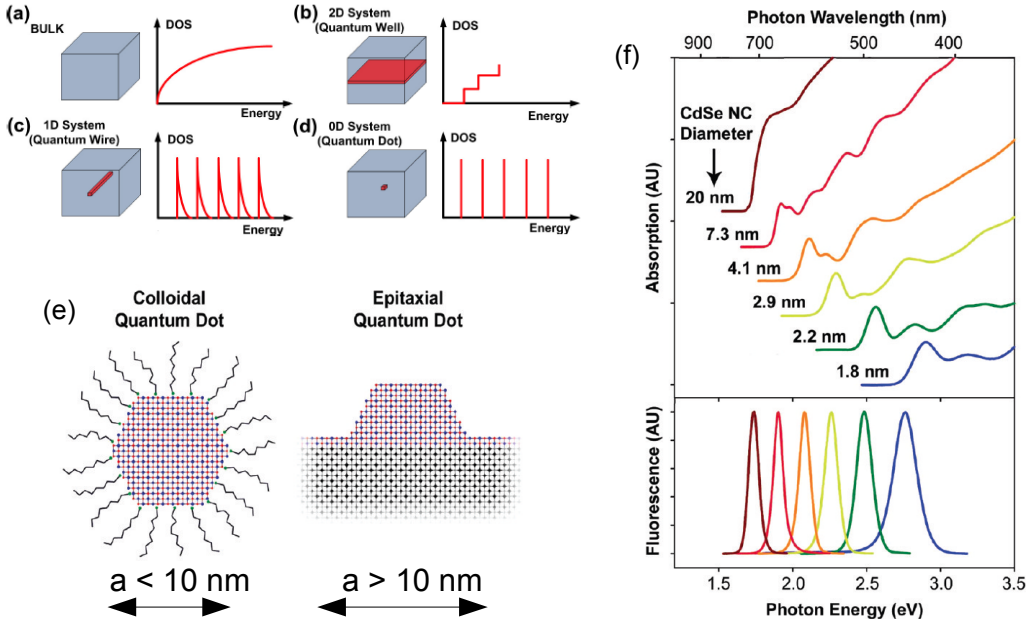

Figure 1.1: a) to d) Quantum confinement and corresponding density of states for quantum wells, quantum wires and quantum dots. e) Strong and weak confinement in colloidal and epitaxial quantum dots, respectively. f) Size dependent absorption and photo-luminescence spectra in CdSe nanocrystals.

can be written as linear combinations of Bloch functions, with a wavenumber $0 < k < 1/a$:

$$\psi(r) = \sum_k c_k e^{ikr} u_k(r)$$

The local part of the Bloch function $u_k(r)$ (periodical with the crystal lattice) is determined only by the atomic structure of the semiconductor, and can be considered independent of the confinement potential. Since the diamater a of colloidal NCs is usually much larger than the lattice constant p (about 0.5 nm), $u_k(r)$ only slightly varies with k for $0 < k < 1/a$ and it can be factorized:

$$\psi(r) = u_0(r) \sum_k c_k e^{ikr} = u_0(r)\phi(r)$$

All confinement effects are contained in the envelope function $\phi(r)$.

CdSe is a direct band gap semiconductor crystal with gap energy $E = 1.75 - 1.8eV$ (688nm). The valence band is constituted essentially by the p orbitals of Selenium electrons, which are completed by the two electrons of the s shell of Cadmium. The conduction band comes from the

s orbital of Cadmium without its electrons. The conduction band is thus unique with effective mass $m_e^* = 0.13m_e$ and it is parabolic (*s-type orbitals*), whereas the valence band is 6 times degenerate (*p-like orbitals*).

This degeneracy is lifted by the spin-orbit interaction in Selenium ($\Delta_{SO} = 420meV$). The total angular momentum of the holes J, which is the sum of the orbital momentum $L = 1$ and of the spin $S = \frac{1}{2}$, becomes a good quantum number. The lowest band $J = \frac{3}{2}$ splits in 2, according to the different projections on the z axis, $J_z = \pm 1/2$ (light holes, $m_{lh}^* = 0.45m_e$) and $J_z = \pm 3/2$ (heavy holes, $m_{hh}^* = 0.90m_e$), as illustrated in Fig. 1.2.

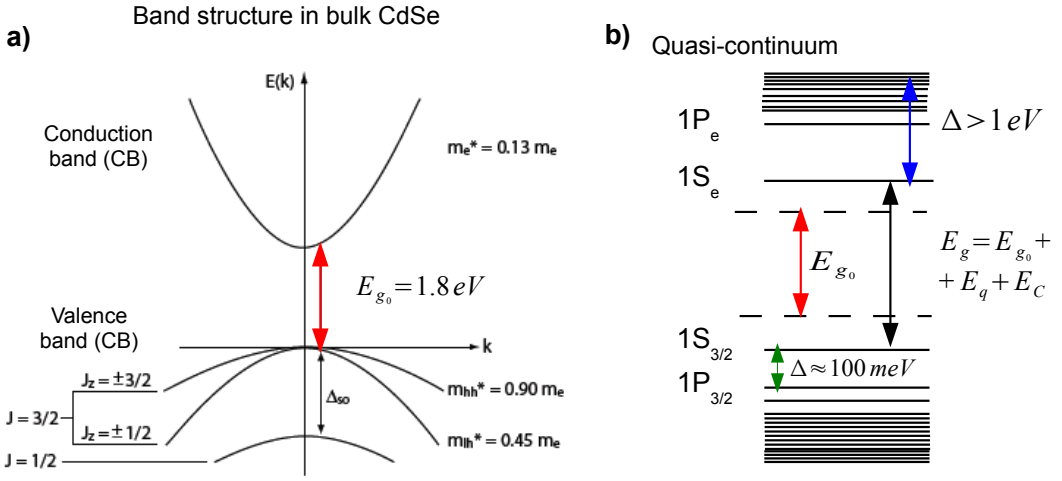

Figure 1.2: a) Band structure in bulk CdSe. b) Schematics of the atomic-like electronic structure in a CdSe nanocrystal, with the spectroscopic notation introduced in the main text. $1S_e$ refers to electronic levels, where $J_e = 1/2$, whereas for holes it is common to indicate the angular momentum J_h as a subscript. For higher energies the levels become a quasi-continuum, because the confinement potential is finite.

Confinement of electrons As they belong to a parabolic band, electrons behave like particles of mass m_e^* in a spherical potential well. Solving the Schrodinger equation for the envelope function $\phi_e(r)$ for a potential well $V(r)$ of diameter a leads to a zero-point energy:

$$E_e(a) = \frac{\hbar^2\pi^2}{2m_e^*a^2}$$

The solutions of the envelope function are hydrogen-like orbitals. In QDs the notation used to name the quantum states follows closely that of an atomic system. Thus the electron ground state shows spherical symmetry (s-orbital) and it is doubly degenerate because of the spin, i.e. $J_e = \frac{1}{2}$. It is commonly referred as $1S_e$.

Confinement of holes Treating the confinement of holes is more complicated because of the degeneracy of heavy and light holes bands.
We just recall here that the first hole level, having a p-symmetry, is four-fold degenerate and it has $J_h = 1 + \frac{1}{2} = \frac{3}{2}$ ($J_z = -\frac{3}{2}, -\frac{1}{2}, \frac{1}{2}, \frac{3}{2}$). It is called $1S_{\frac{3}{2}}$. The hole ground state energy is given by:

$$E_h(\beta, a) = \frac{\hbar^2 \chi^2(\beta)}{2m^*_{hh} a^2}$$

where β is the ratio between light and heavy holes masses $\beta = \frac{m^*_{lh}}{m^*_{hh}}$ and $\chi(\beta)$ is a term related to the spherical Bessel functions [24].

1.1.1 Fine Structure of the band-edge transition

The composition of electron and hole ground states yields the eight-fold degenerate exciton ground state $1S_{\frac{3}{2}}1S_e$, called the exciton band-edge transition. Various effects intervene to lift the degeneracy of this state: the internal crystal field (for wurtzite), shape effects and the electron-hole exchange interaction [22] [24].

The first two effects can be grouped together because they have the common result to split the heavy and the light hole bands, i.e. $J_z = \pm\frac{3}{2}$ and $J_z = \pm\frac{1}{2}$. The crystal field splitting sets the state $|J_z| = \frac{3}{2}$ as the lowest state. It does not depend much on the dimension (it is the same in bulk), but only on the ratio β between light and heavy holes masses, and it is always positive. In CdSe it is 25 meV.

The shape factor, proportional to the ellipticity $\mu = 1 - \frac{c}{b}$ [24] (b is the major and c the minor axis of the ellipse), modifies the energy splitting between the heavy and light holes. In perfectly spherical nanocrystals it is zero. Importantly, the shape factor can be negative, and thus reverse the hole levels. In CdSe nano-rods the inversion of the hole ground state energy depends on the radius of the rod, but not much on its length, as we will see in the following [22]. The shape factor in anisotropic structures, like rods or elliptical nano-particles, is commonly characterized by the ratio between its major axis b and its minor axis c, which is called *aspect ratio* (AR).

It is possible to demonstrate that electron-hole states in a nanocrystal are mixed by their interaction, even if we are in the regime of strong confinement, and their wavefunction is not the simple product of electron and hole wavefunctions. Because of the electron-hole exchange interaction the good quantum number becomes the total angular momentum of the electron-hole pair K.
The ground state results in two degenerate states with $K = 1$ (upper branch) and $K = 2$ (lower branch), because of the contribution of the shape factor and of the crystal field. The exchange interaction removes this degeneracy, according to the projection K_z of the total angular momentum K.

In conclusion, the fundamental transition $1S_{\frac{3}{2}}1S_e$ presents a fine structure, constituted of 5 energetically separated sub-levels, sketched in Fig. 1.3:

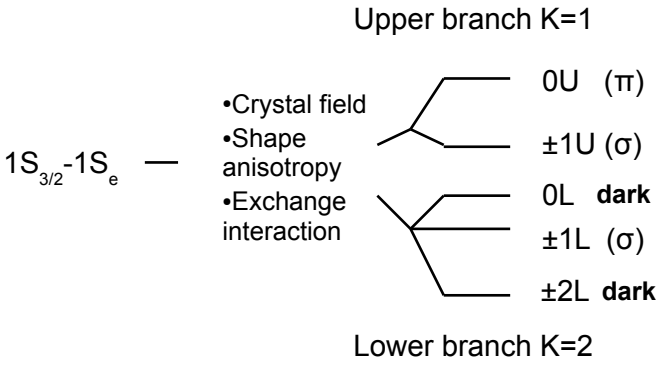

Figure 1.3: Sketch of the band-edge exciton fine structure. The order of the energy levels and their relative energy difference can specifically depend on the nanocrystal shape and size.

- One state with $K_z = \pm 2$ doubly degenerate:

$$|\pm 2\rangle = \Phi_{\pm 1/2,\pm 3/2}$$

  where Φ represents to the factorized electron-hole wavefunction, the first subscript refer to the electron and the second one to the hole angular momentum.

- Two states with $K_z = \pm 1$ (Upper and Lower depending on the branch they originate), each one doubly degenerate:

$$|-1L\rangle = A\Phi_{+1/2,-3/2} - B\Phi_{-1/2,-1/2} \qquad |-1U\rangle = A\Phi_{+1/2,-3/2} - B\Phi_{-1/2,-1/2}$$
$$|+1L\rangle = A\Phi_{-1/2,+3/2} + B\Phi_{+1/2,+1/2} \qquad |+1U\rangle = B\Phi_{-1/2,+3/2} - A\Phi_{+1/2,+1/2}$$

  where A and B are complex constants depending on the size and ellipticity of the nanocrystal.

- Two non degenerate states with $K_z = 0$ (Upper and Lower):

$$|0L\rangle = \Phi_{+1/2,-1/2} - \Phi_{-1/2,+1/2}$$
$$|0U\rangle = \Phi_{+1/2,-1/2} + \Phi_{-1/2,+1/2}$$

Only three of these 5 states are optically active, namely the states $0U$, $\pm 1U$ and $\pm 1L$. The ± 2 states are not coupled to light because photons cannot have an angular momentum = 2, while $0L$ is a dipole transition from $0 \rightarrow 0$ which is forbidden by the transition rules (dark exciton). $0U$, on the other side, is allowed, because of a constructive interference phenomenon between indistinguishable $\Phi_{+1/2,-1/2}$ and $\Phi_{-1/2,+1/2}$ wavefunctions.

The existence of a fine structure has been proposed for the first time in 1996 [24] in order to explain the Stokes shift. This is a red-shift of the photo-luminescence (PL) spectra with respect to the absorption peak. As we will see in the following, the fine structure plays an important role

for the nanocrystals spectral properties, the radiative lifetime, and the polarization properties of the emission.

Even if the existence of a fine structure has been proved by many experimental works, the relative positions of the 5 states and their energy splittings strongly depend on the geometrical parameters of the nano-structure. Examples of calculated fine structures for perfectly spherical wurtzite nanocrystals of different size, prolate nanocrystals and CdSe nano-rods are shown in Fig. 1.4 and in Fig. 1.5.

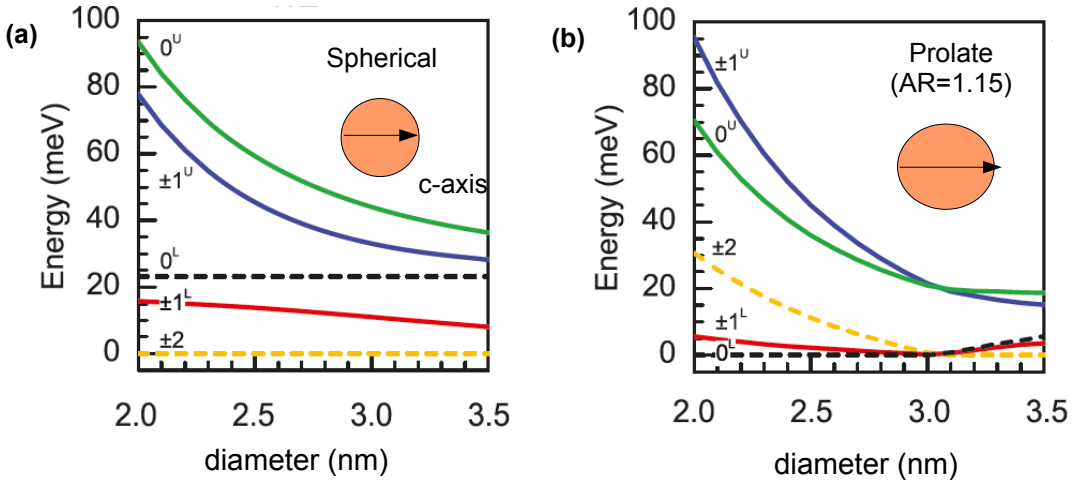

Figure 1.4: Evolution of the fine structure splitting with the size for: a) spherical wurtzite CdSe nanocrystals and b) slightly prolate nanocrystals [23]. Even a low aspect ratio of 1.15 leads to a completely different distribution of the fine structure energy levels.

Fine structure and polarization The fine structure has important consequences on the polarization properties of the emitted light:

$+1U$ and $+1L$ emit σ^+ polarized photons (right, or clockwise, circular polarization)

$-1U$ and $-1L$ emit σ^- polarized photons (left, or anticlockwise, circular polarization)

Every state ± 1 emits at the same time σ^- and σ^+ photons without any coherence relationship. Efros [24] showed that these correspond to 2 dipoles of the same strength and oriented in the plane perpendicular to the c-axis of the hexagonal crystalline structure.

On the other side, the $0U$ transition is linearly polarized π, and it corresponds to a linear dipole oscillating along the nanocrystal c-axis. In the case of a perfectly spherical CdSe nanocrystal only about 20% of photons emitted are linearly polarized, while the rest of the emission comes from a so called degenerate 2 D dipole. In prolate NCs the contribution of linear

polarization can become more important.

1.1.2 CdSe quantum rods

CdSe rods, compared to spherical nanocrystals, show higher photo-luminescence quantum efficiency [59], strongly linear polarized emission [27], an increase of the global Stokes shift [27] (from 40 to 100 meV for an aspect ratio increasing from 0 to $AR = 10$), and significantly faster carrier relaxation. Specific to nano-rods are the influence of the electric field on the optical properties and the high degree of polarization (typically more than 50%) of the emitted light along the wurtzite c-axis.

The sensitivity to external and internal electric fields comes from the elongated shape which allows different degree of overlap of the electron-hole wavefunctions. When nano-rods are subjected to external field they experience a so called quantum confined Stark effect (QCSE), which induces a red-shift of the optical transitions (absorption and emission).
The polarization properties depend on the anisotropic shape of nano-rods, but also on their size. In particular for thin rods, the polarization was shown to increase with the aspect ratio AR, even if a sharp transition from not-polarized to polarized emission was observed for AR of the order of 1.2-1.3, i.e. already for prolate, almost spherical particles [27]. In fact, it is the fine structure which is the dominant factor in defining not only the character of the emission (dark or bright exciton), but also the polarization properties.

Even if the intrinsic level structure is the main responsible for the polarization properties of the band edge transition, the polarization can also be enhanced by the geometrical structure of nano-rods. The dielectric environment of a cylindrical structure where the diameter is much smaller than the light wavelength reduces the component of the electric field perpendicular to the c-axis, like in InP nanowires (waveguide effect). The dielectric confinement is connected with the difference between dielectric constants of the semiconductor crystal, ϵ_s , and the surrounding medium, ϵ_m [28]. In spherical nano-particles it usually does not affect the optical spectra because the charge distributions of an excited electron and hole practically compensate each other at each point of the nanocrystal, leading to a complete cancellation of the carrier electric field outside the nanocrystal. In nano-rods the electron and hole can be at a distance larger than the nano-rods radius and interact predominantly through the surrounding medium.

CdSe rods electronic structure The nano-rods spectral lines are less separated than those measured on spherical QDs, because of reduced quantum confinement in one dimension. In addition, there are more sources of inhomogeneous broadening.

Nearly identical spectra were observed for samples of small diameter (about 3nm) and different lengths (AR from 3 to 10), while significant differences were measured on thicker rods (6nm) [25]. This shows clearly that both the band gap of the rods and also the excited optical transitions depend mainly on their diameter.

In [25] the electronic structure of CdSe rods is calculated starting from the formalism developed for studying quantum wires and a good agreement with experimental data is found. nano-rods are interesting because they provide significant insight on the evolution of the electronic structure from zero dimensional QDs to one dimensional quantum wires.

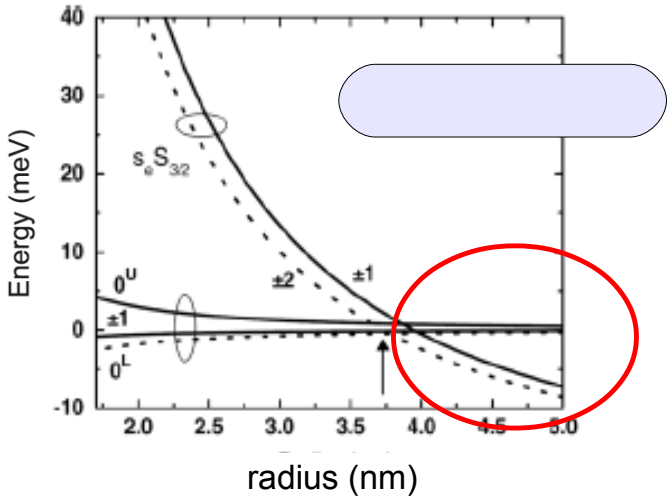

Figure 1.5: Evolution of the fine structure splitting with the diameter for CdSe nano-rods (length $= 20nm$) as calculated in [26]. A red circle show a region of large rod diameters, where the fine structure resembles that of spherical nanocrystals. The effect of the rod length does is negligible for $AR \gtrapprox 2$ [25] [26].

The fine structure of CdSe nano-rods was calculated by Woggon [26] and it is shown in Fig. 1.5. It is very interesting to remark that the fine structure of CdSe quantum rods is similar to that found for slightly prolate spherical nanocrystals [24] [23], as illustrated in Fig.1.4 b). In nano-rods an inversion of the hole ground state, i.e. a transition to a z-oriented p-type wavefunction for holes, occurs below a critical radius of $R = 2.1nm$ according to [31] and 3.7nm according to [26], as shown in Fig. 1.5.

This is induced by the shape factor, which can exchange the heavy hole $J_z = \frac{3}{2}$ and the light hole $J_z = \frac{1}{2}$ levels. The cylindrical shape of rods also reduce the exchange interaction because the electrons and the holes are less strongly confined, and thus the energy splitting between the levels in the fine structure is smaller (compare the energy scales in Fig. 1.5 and Fig. 1.4).

A similar transition in the electronic structure with the rod diameter was also observed by Hu [27] by studying the polarization of the emission and the Stokes shift as a function of the rod aspect ratio. It was found that already an AR of 1.2-1.3 is enough to swap the dark and bright excitons.

Moreover the fine structure in rod-like nanocrystals can be influenced by external or intrinsic (e.g. due to charge localization in trap states or piezo-electric effects) electric fields, by means of the Stark effect.

1.2 Optical transitions

The optical properties of nanocrystals rely on their electronic structure, which results in a mixture of quantum confinement effects and semiconductor properties.
Three spectral domains can be distinguished according to the energy above the bandgap: very excited states (about 1 eV), quantized energy states(< 1 eV) and the fine structure of the first energy state (< 100 meV).

Very excited states Very excited states, typically more than 1eV above the band gap, see Fig. 1.2 b), are important for the absorption. Absorption experiments show that for these states the quantum confinement is negligible and the nanocrystals behavior can be described by the theory of classical interactions between light and small particles [29].

For spherical CdSe nanocrystals, absorption cross sections of $10\mathring{A}^2$ ($0.1 * 10^{-14} cm^2$) [30] were reported, much larger than non-resonant cross sections of atoms or molecules (for comparison, resonant cross section of Rhodamine $6G$ is about $4\mathring{A}^2$ at 532nm).
We will see that in core/shell structures this value can be even larger, since significant absorption is provided by the shell, whose volume can be very large especially in rod shaped nanocrystals. For example, giant shell nanocrystals (radius$\simeq$ 6 nm) have an absorption cross section of $4 * 10^{-14} cm^2$ at 350 nm.

We will excite nanocrystal with a diode laser at 405 nm (= 3.06 eV). At high energies, electrons and holes present a quasi-continuous distribution of states, as shown in Fig. 1.2 b) and absorption can be modelled as a random process, where the probability to create N_{eh} electron-hole pairs is a Poisson distribution with average number $\langle N_{eh} \rangle$:

$$P(N_{eh}, \langle N_{eh} \rangle) = e^{-\langle N_{eh} \rangle} \frac{\langle N_{eh} \rangle^{N_{eh}}}{N_{eh}!}$$

The average number of electron-hole pairs $\langle N_{eh} \rangle$ is proportional to the excitation intensity via the absorption cross section.

Quantum states The energy of the interband optical transitions are given by the sum of the band-gap energy and the confinement energies of electrons and holes, while Coulomb interaction is treated as a perturbation.

The strength of each transition is proportional to the electric dipole matrix element between the electron and the hole states, according to the Fermi's Golden rule, like in atomic systems:

$$P = |< \psi_e(r)|V|\psi_h(r) >|^2$$

where V is given by the product of the electric field and the dipole moment operators. Since the envelope function varies much slower than the local part of the Bloch function, this product can be factorized as:

$$P = |p_{cv}|^2 \left| \int \phi_e(r)\phi_h(r) d^3r \right|^2 = |p_{cv}|^2 P_{eh}$$

p_{cv} is the dipole matrix element in the bulk material. Thus the strength of a transition depends on the superposition of envelope wavefunctions of electron and hole P_{eh}

The photo-luminescence spectra at room temperature show only one emission peak, corresponding to the ground state transition. This is because the difference between energy levels (about 100 meV) is much larger than the thermal energy at room temperature (about 25meV), because of the strong level of quantum confinement, as illustrated in Fig. 1.2 b). Therefore, many optical properties of colloidal QDs are often determined by the fine structure of the band-edge exciton transition.

1.2.1 Radiative decay rate

The radiative decay rates depend both on the strength of the dipole transitions and on the density of electromagnetic modes of the environment. Both the electronic levels structure and the available electromagnetic states play a role.
For instance, the radiative rate can be changed by changing the density of states of radiation, by inserting an emitter in a cavity or by using proper interfaces, i.e. by controlling the dielectric environment where a quantum emitter is placed. An important case is the Purcell effect, where the emitter is 'forced' to emit photons in the state (momentum, energy, polarization) chosen by the cavity.

In this thesis we will only study the case of the vicinity of a dielectric interface, because it is our typical experimental condition: single nanocrystals are usually deposited on a microscope glass coverslip.
In the case where the density of electromagnetic modes $\rho(\lambda)$ is smooth around the emission wavelength of the dipole transition (no resonances, like surface plasmons,...), the radiative lifetime is just reduced by a (small) constant factor, since the electron can be treated like in a damped oscillator. For our purpose it is enough to consider that γ_R is proportional to the electron and hole wavefunctions:

$$\gamma_R \propto |\langle \phi_e(r) | \phi_h(r) \rangle|^2 = P_{eh}$$

Photo-luminescence and fine structure The photo-luminescence depends on the fine structure, and this dependence can determine an evolution of lifetime with temperature and explain the observed spectral Stokes shift.

At room temperature $T = 300K$ the thermal energy $E = kT$ is usually enough to populate several states of the fine structure. The contribution of each transition to the total fluorescence signal at $T > 0$ is evaluated by considering that each level of energy ϵ_i above the fundamental transition is populated according to Boltzmann statistics. The recombination probability $p_i(T)$, i.e. the fraction of photons coming from transition i, is given by the strength of the transition f_i and by its probability to be populated:

$$p_i(T) = \frac{f_i e^{-\frac{\epsilon_i}{KT}}}{\sum_j f_j e^{-\frac{\epsilon_i}{KT}}}$$

The strength of the transition f_i is just proportional to the radiative rate $\gamma_{R,i}$.

Fig. 1.6 a) shows the relative strength f_i of the three bright states (i.e. optically allowed) of the fine structure, as a function of the radius for a perfectly spherical NC.

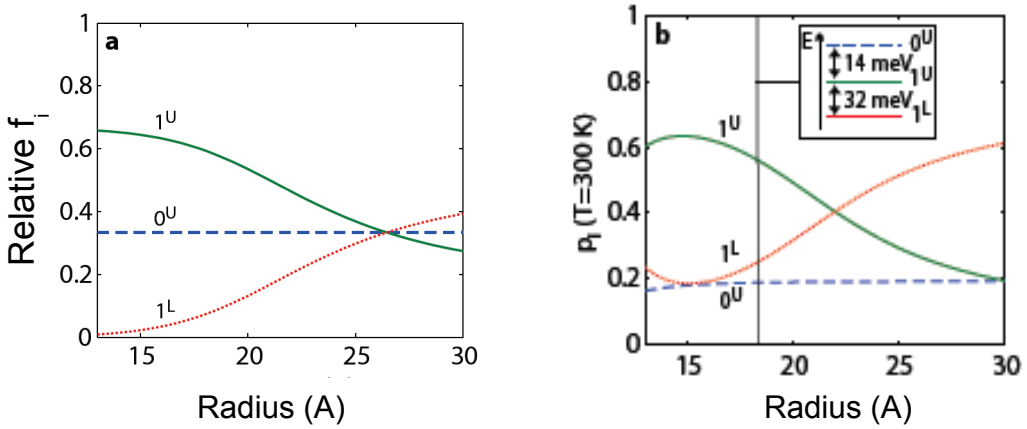

Figure 1.6: a) Relative oscillator strengths f_i for the 3 bright states of the fine structure in a spherical CdSe nanocrystal. b) Room temperature radiative recombination probabilities p_i as a function of the radius. In the inset, the position and the energy difference of $1L$, $1U$ and $0U$ is shown.

The lowest state in energy $1L$ (see the inset of Fig. 1.6 b)) is the less coupled to the electromagnetic field. This is why the absorption is made prevalently by $1U$ and $0U$. The emission, on the other hand, depends also on the thermal population of the levels, and so an important contribution at $T = 300K$ comes from the lowest energy state $1L$, especially for large dots, as illustrated in Fig. 1.6 b). This model well explains the spectral Stokes shift, introduced before: the PL emission is red-shifted with respect to the absorption at room temperature.

This model also allows to reproduce the observed behavior of the lifetime as a function of the temperature: the lifetime increases at low temperature because photons come more and more frequently from $1L$, which is not well coupled to the electromagnetic field. The average radiative rate at a temperature T can be calculated from the probability $p_i(T)$:

$$\gamma_R(T) = \sum p_i(T)\gamma_{R,i}$$

where $\gamma_{R,i}$ are the decay rates for each transition i.

Here we just considered the example of perfectly spherical CdSe nanocrystals, since they are the most well-known. As we already explained, large variations of the fine structure, and even a swapping of the energy levels, may be induced just by slightly changing the shape and the size of the nano-structure.

1.3 Non-radiative recombinations in nanocrystals

After the excitation, the charge carriers inside a nanocrystal tend to restore the initial state of equilibrium by losing their excess energy. Like in bulk semiconductors, nanocrystals undergo several possible relaxation pathways.

The main distinction is between radiative (relaxation by emission of 1 photon) or non-radiative processes. We already discussed the radiative recombination of the band-edge exciton state.

Here we review the main non-radiative relaxation processes in a quantum confined system which are:

(1) Auger recombination, i.e. multi-carrier scattering processes

(2) Creation of phonons (i.e. lattice vibrations) via carrier-phonon interactions, which lead to heating of the material

(3) Charge trapping in defect states

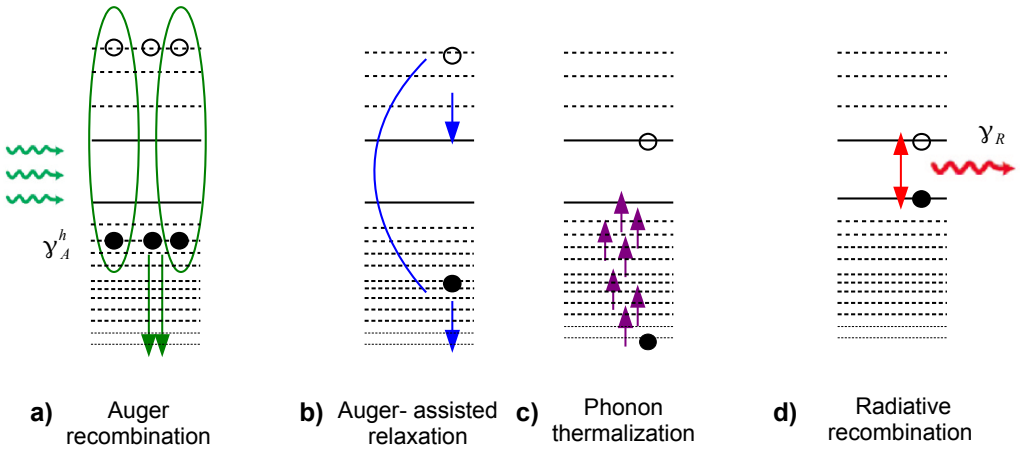

Figure 1.7: Non-radiative and radiative recombinations in nanocrystals. Schematics of the excitation and relaxation processes. 1) Excitation of $N_{eh} = 3$ e-h pairs and Auger recombination via energy transfer to one spectator hole with rate γ_A^h. 2) and 3) Auger-assisted and thermal relaxation to the band-edge fundamental transition. Purple arrows represents phonon scattering. 4) Radiative recombination of the remaining electron-hole pair.

1.3.1 Auger recombination

The Auger effect is essential in colloidal QDs, and its efficiency is strictly connected to the strong quantum confinement. Auger effect deserves special attention because it plays a central role in different effects which are specific to nanocrystals, from quenching of the emission (acting as a non-radiative channel in competition with radiative recombination), photo-ionization and thermalization of hot carriers, to single photon emission. All these phenomena will be considered in detail in this manuscript, at different stages. Here we just define what is the Auger effect and how it can give non-radiative recombination.

The *Auger recombination* consists in the transfer of the energy of an e-h pair to a third particle (electron, hole or exciton) because of the Coulomb interaction. In a QD, the Auger effect is a 3 particles process, while in 1D confined systems like quantum wires or rods it is a 2 particles process because e-h pairs organize themselves in 1D excitons.
An Auger rate can be defined as γ_A, which gives the efficiency of energy transfer to the third charge, γ_A^h for transfer to holes and γ_A^e for transfer to electrons. Since they can have different rates, γ_A^h and γ_A^e should be considered separately.

The Auger recombination is the main origin for single photon emission at room temperature in nanocrystals, as illustrated in Fig. 1.7 a). When N_{eh} are excited inside a nanocrystal, they recombine non radiatively, until only one e-h pair remains, giving rise to the emission of a single photon (Fig. 1.7 d)).

Actually any energy transfer between carriers via Coulomb interactions (charge scattering) is generically referred to as an Auger effect, even if there is not an electron-hole recombination. This energy exchange plays an important role in charge thermalization, Fig. 1.7 b).

There are two reasons why Auger effect is so efficient in colloidal QDs.
The first reason is an enhancement of Coulomb interactions between the carriers confined in a small volume of the nanocrystal. In 2000 [51], it was demonstrated for the first time that Auger recombination lifetimes of CdSe nanocrystals scale linearly with the volume of the particle. Recently, it was shown that this behavior ('V-scaling') is universal and extends to nanocrystals made from other direct-gap and indirect-gap semiconductors, and also to nano-rods [53]. However, the volume coincides with the physical volume only if carrier are completely confined by a strong potential well, otherwise electron and hole can have different overlap, and a radius of the exciton must be defined.

The second reason is more subtle: the translational momentum is not a good quantum number for electron and hole motion in a strongly confining potential [52]. Since practically the whole annihilation energy of the electron-hole recombination is transferred into kinetic energy of the third charge, a violation of momentum conservation in the scattering process is required. Qualitatively, electrons (or holes) have a higher probability to take up the annihilation energy at a place where their kinetic energy uncertainty has a maximum value. Therefore, it is more probable for carriers to take up the Auger recombination energy in the presence of abrupt hetero-interfaces or defects center, where their position is well defined.

On the other hand, the discreteness of electronic levels should imply a reduced availability of states satisfying the energy conservation condition. The interplay of both contributions determines the net effect in each system, i.e. Auger effect can be very different also for slightly different nanocrystals, or even within a sample with the same nominal characteristics.

1.3.2 Exciton-phonon interactions

Phonons intervene in the thermalization of an exciton towards its band-edge level, Fig. 1.7 c) and also in the band-edge recombination of electrons and holes: relaxation proceeds by exciting one or more phonons.

Intraband relaxations Like the carriers also the phonons are affected by the quantum confinement. In a confined structure both excitons and phonons show discrete energy levels, so that a priori an intraband transition should be inhibited if there are no available phonons with the same energy of the transition.
This fact had lead to the prediction of a phonon-bottleneck for relaxations in nanocrystals. On the contrary, it was observed experimentally that the relaxation is accelerated by the quantum confinement. For example for a CdSe nanocrystal with $R = 1.7nm$, the electron relaxes from the 1P level to the 1S level in 100 fs, 10 times faster than in the bulk material.
This is because the thermalization is mediated by the Auger energy transfer from electrons to holes, Fig. 1.7 b). The density of hole states is high, because of the valence-band degeneracy and high effective mass, so the relaxation by phonons can be efficient.

Since intraband relaxations are much faster than radiative recombinations (hundreds of fs compared to ns), the fluorescence always comes from the ground state. This is why in photoluminescence spectra only one main peak is present.

Interband relaxations Interband relaxations, i.e. electron-hole recombinations, are influenced by phonons. The emission spectrum is broadened by the interactions with the phonons.

The phonon scattering in interband relaxations is a non radiative channel which is in direct competition with the radiative recombination, and its contribution is accounted by a non radiative rate γ_{NR}.

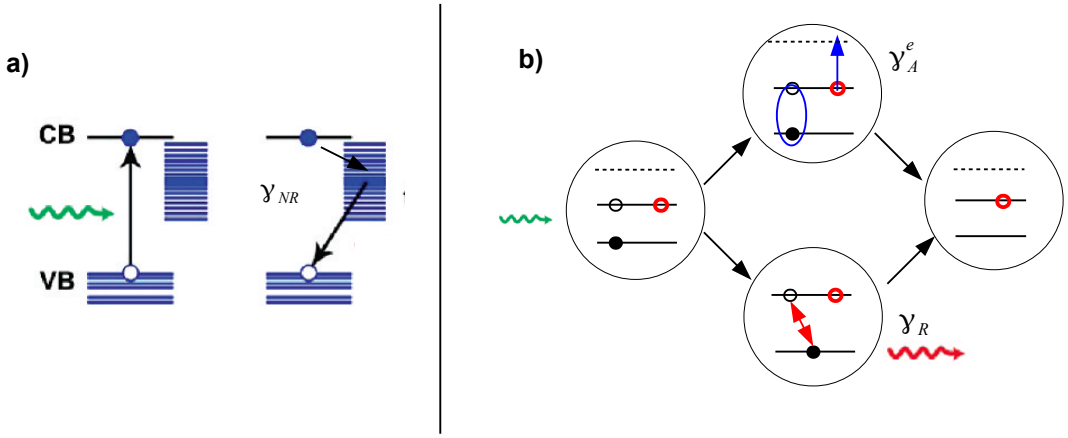

Figure 1.8: a) Non-radiative decay via hole trapping and successive non radiative electron-hole recombination. b) Competition between Auger recombination and radiative recombination of an electron-hole pair in a negatively charged nanocrystal (the extra electron is in red). The blue circle indicates Auger recombination followed by energy transfer to the spectator electron.

1.3.3 Charge trapping and photo-ionization

The charge carrier trapping refers to the localization of the electron or hole at lattice defects within the nanocrystal structure or at unsaturated bonds on the nanocrystal surface atoms. A surface trap is often modeled as an unsaturated anionic dangling bond $Se^{(2-)}$ on the CdSe surface surrounded by organic material (surface traps) or by another semiconductor (interface traps). From an energetic point of view, trap states create energy levels within the semiconductor band gap.
It has been shown that inorganic or organic passivation of the unsaturated bonds on the nanocrystal surface leads to increased fluorescence efficiency due to reduced surface trapping.

Typical timescales for removal of a charge from the conduction band to a trap state are 1 to tens of ps, lifetimes of trap states can be highly distributed from ns to μs. The charges in a trap state can recombine with their countercharge delocalized inside the nanocrystal. This is usually a non-radiative recombination channel and contributes to increase the rate γ_{NR}, as illustrated in Fig. 1.8 a). Sometimes the recombination can also be radiative: a low fluorescence in the infrared spectrum has been attributed to the radiative recombination of trapped charges [54].

When the charge is trapped for long time, the nanocrystal is said to be in a charge-separated state: one charge in a localized trap state, and its counterpart delocalized inside the nanocrystal. As illustrated in Fig. 1.8 b), when a nanocrystal is in a charged state (negative for instance), the emission can be quenched by a competition between Auger and radiative recombinations. This subject will be widely developed in Chapter 2.

A last consideration: the charge trapping is here considered as a reversible process, which is different from chemical reactions, like oxidation or ions diffusion, which are irreversible and lead to permanent bleaching of luminescence, as we will see in Chapter 3, treating the subject of photo-stability.

1.3.4 Definition of Quantum Yield

Unlike single atoms or ions, which are really nearly 2-level systems, the spontaneous emission due to light-matter interaction in complex systems like quantum dots is only one of the possible decay channels. As we discussed before, many other non-radiative decay channels exist, like electron-electron scattering, phonons, trapping of charges, Auger recombination..., which directly compete with radiative emission.

The decay processes in complex systems are thus characterized by a certain probability to transfer energy to the photons.
The Quantum Yield measures the probability of a radiative decay:

$$QY = \frac{\gamma_R}{\gamma_R + \gamma_{NR}}$$

Since in a nanocrystal the Auger effect plays an important role we separate the contribution of non-radiative Auger recombination:

$$QY = \frac{\gamma_R}{\gamma_R + \gamma_{NR} + \gamma_A}$$

1.4 Core/shell nanocrystals

The nanocrystal surface is passivated by the organic ligands adsorbed during the synthesis. However, this protective layer is unstable and it is normally limited to 40-60% of the surface. Therefore many dangling bonds close to the nanocrystal core represent trap states for charges, which, as we saw before, increase the non-radiative recombination of excitons. The main effect of this poor quality passivation is a reduction of the fluorescence Quantum Yield, which in core-only nanocrystals is usually less than 10%.

In order to obtain an effective and durable suppression of surface non-radiative recombination centers, some layers of a usually higher band-gap material (like ZnS, CdS, ZnSe) are deposited around the original core. This shell passivates the dangling bonds at the surface of the core and reduces the influence of external environment on the optical active QDs core. The surface of the shell, in addition, is passivated by organic ligands.

High QYs (measured in solution) can thus be obtained, up to 70-90%. Since the shell physically separates the surface of the optically active core from its surrounding medium, the sensitivity of the optical properties to the changes in the local environment of the nanocrystals surface, induced, for example, by the presence of oxygen or water molecules, is reduced. With respect to core NCs, core/shell systems exhibit generally enhanced stability against photo-degradation. At the same time, the shell growth reduces the number of surface dangling bonds, which can act as trap states for the charge carriers and thereby reduce the fluorescence QY.

The control of the shell growth and thickness is a delicate point.
If the shell is too thin, the passivation is inefficient, resulting in reduced photo-stability and QY. If the shell is too thick, on the other hand, the strain induced by the lattice mismatch between the core and the shell can lead to the generation of interface or internal defects states, which would also reduce QY.

1.4.1 Classification of core/shell heterostructures

In addition to passivation and increased QY, shell engeneering offers the possibility to tune other optical properties, like fluorescence wavelength, polarization and lifetime, which are all linked to an engineering of the electron and hole wavefunctions.

The shell can have different effects on the electron and hole wavefunctions, according to the band gaps and the relative position of electronic energy levels (offset) of core and shell quantum confined semiconductors.

Two main cases can be distinguished, denominated type-I, and type-II band alignment. However, as we will see, the bulk band alignment is not the only parameter and it should be better to speak about type-I and type-II wavefunction localization [32]. A sketch is shown in Fig. 1.9.
In the first case, both electrons and holes are localized either in the core or in the shell (reversed type-I).
In the second case, hole and the electron are spatially separated in different regions of the heterostructure, since normally either the valence-band edge or the conduction band edge of the shell material is located in the band gap of the core.

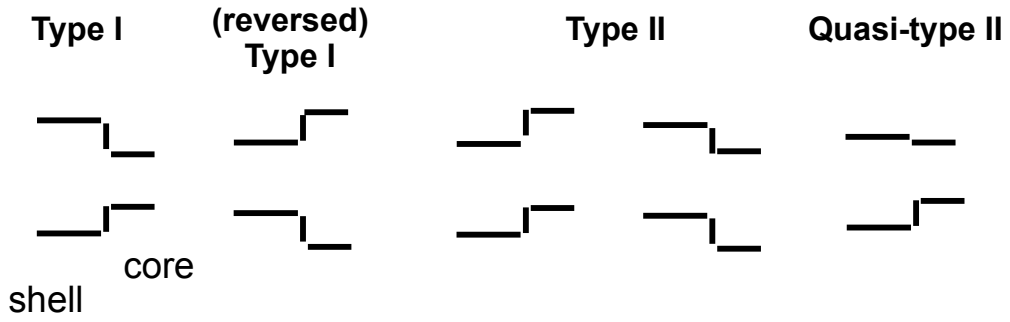

Figure 1.9: Classification of band alignment in core/shell heterostructures.

In type-I nanocrystals, the shell is used to passivate the surface of the core with the goal of improving the photo-luminescence QY and the stability against photo-bleaching, as already described.
Anyway basic optical properties, like lifetime, spectra, polarization and also photo-luminescence blinking are only slightly modified by the presence of the shell. The shell growth is accompanied by a small red shift (5-10 nm, depending on the specific materials) of the excitonic peak in the absorption and in the PL spectrum with respect to the core-only system. This observation is attributed to a partial leakage of the exciton into the shell material.

The first published prototype system was CdSe/ZnS. Its synthesis was first described by Hines and Guyot-Sionnest [33], who overcoated 3-nm CdSe nanocrystals with 1-2 monolayers of ZnS, resulting in a QY of 50%. Since the ZnS shell band gap is much larger than CdSe, complete confinement to the CdSe core is expected for both electrons and holes, as suggested by the absence of any appreciable red shift in the observed optical spectra, after the shell growth.

In type-II systems, the shell growth aims at a significant redshift (typically more than 30nm) of the emission wavelength of the NCs. The band alignment leads to a smaller effective bandgap than each one of the constituting core and shell materials. Type-II NCs have been developed in particular for near-infrared emission, using for example CdTe/CdSe or CdSe/ZnTe. In contrast to type-I systems, the PL decay times are much longer in type-II NCs due to the lower overlap of the electron and hole wavefunctions.

As one of the charge carriers (typically the hole) is located in the core, far from the surface, an overgrowth of type-II core/shell NCs can be used in the same way as in type-I systems to improve the fluorescence QY and photo-stability.

Experimental evidence of type-I or type-II heterostructures The first experimental signature to distinguish between type-I and type-II heterostructures is the red-shift of the absorption and emission spectra with respect to the sole core. Also the lifetime increases in type-II

heterostructure, as a consequence of reduced wavefunction superposition P_{eh} [34] [39].

Another signature of the wavefunction distribution between the core and the shell is the binding energy of the bi-exciton state, i.e. the bound state of two excitons. This binding energy is supposed to be negative for a type-I alignment, because of the global neutrality of charge inside the core (or the shell). The Coulomb interaction becomes repulsive if electrons and holes are localized at different places and thus the binding energy becomes positive for a type-II alignment [46].

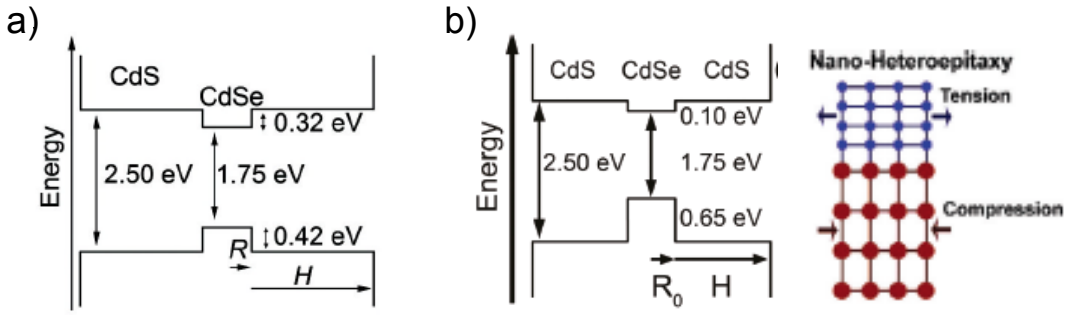

Figure 1.10: a) Band alignment and band offsets in bulk CdSe and CdS. b) Proposed band alignment in CdSe/CdS nanocrystal heterostructures. Strain and change in the lattice constants caused by the shell growth can modify the bulk band alignment.

1.4.2 CdSe/CdS nanocrystals: quasi-type II heterostructures

A CdSe-based system exhibiting a peculiar band alignment is CdSe/CdS. In this case, a large band offset for the holes (about 0.4-0.6 eV) is combined with a relatively small one for the electrons (from 0 to less than 0.3 eV), as can be seen in Fig. 1.10.

An epitaxial growth of the shell is favored by the comparably small lattice mismatch of around 4% between the core and shell material. Peng et al. [34] reported for the first time the synthesis and characterization of a series of CdSe/CdS NCs with core diameters ranging from 2.3 to 3.9nm and QYs above 50%. Since then, this kind of structure has been studied by several groups.

Ab initio calculations [37] have shown recently that, owing to the small conduction band offset between CdSe and CdS in a nanostructure, the wave function of the electron in a spherical CdSe/CdS NC with total radius R_{tot} is almost indistinguishable from that calculated for a CdSe core with $R = R_{tot}$. The hole wave function was instead found [37] to be strongly suppressed at the surface and mostly (but not exclusively) localized in the core region.

Quantum confined band offsets are different than in bulk materials (0.32 meV for the conduction band and 0.42 meV for the valence band, respectively) because of strain or change in the lattice parameter (and so they are expected to change with temperature too). This consideration

is essential when a small offset exists, like in CdSe and CdS. In this case, many parameters may play a role in determining the final band alignment.

Fig. 1.10 a) shows the band alignment of bulk CdSe and CdS, while Fig. 1.10 b) shows a band alignment, which better reproduces the experimental results about the lifetime and the emission spectra in CdSe/CdS heterostructure [44] [55].

Altough different groups use different models for calculating the band alignment, there is a large agreement on the fact that the hole is well localized inside the core, because of the large valence band gap offset between CdSe and CdS and of the large hole effective mass m_h^*. Since the electron wavefunction can be either totally or partially delocalized into the shell, it is common to describe CdSe/CdS nanocrystals as *quasi-type II* structures [39] [49].

1.4.3 Engeneering the wavefunction delocalization

Choice of core and shell materials. The bulk band gap alignment between the core and shell material is the first parameter to determine the localization of the electron and hole wavefunctions.

However not every combination is possible. A general requirement for the synthesis of core/shell nanocrystals with satisfactory optical properties is the epitaxial-type shell growth. Therefore an appropriate band alignment is not the sole criterion for the choice of materials but rather the core and shell materials should crystallize in the same structure and exhibit a small lattice mismatch. In the opposite case, the growth of the shell results in strain and the formation of defect states at the core/shell interface or within the shell. These can act as trap states for photo-generated charge carriers and decrease the fluorescence QY.

This is the reason why thick shells can be realized by low lattice mismatch like CdSe (lattice constant = $4.3\mathring{A}$) and CdS ($4.136\mathring{A}$, mismatch of $\simeq 4\%$), but not with CdSe and ZnS ($5.41\mathring{A}$, mismatch of $\simeq 20\%$)

Core and shell dimension: In the case of quasi-type II heterostructures, because of the small difference between the core conduction ground state and the shell, a transition between a proper type-I and a type-II condition may be obtained by tuning the core and the shell size.

A diagram of the wavefunction localization in CdSe/CdS nanocrystals has been calculated in [39] and it is reported in Fig. 1.11 b). This figure shows the overlap intergral P_{eh} between the electron and the hole as a function of the core and of the shell size.

Shell shape, Electric Field, Dipole moment: An anisotropic, rod-like shell can well separate electrons and holes [47]. In [38] the authors reported that morphological differences of the shell, from cylindrical to arrow-like shaped, can lead to important modifications of the optical properties.

A separation of theelectron and hole wavefunctions can be obtained by applying an external electric field (Stark effect). An intrinsic electric dipole can be present in such an asymmetric structure as well.

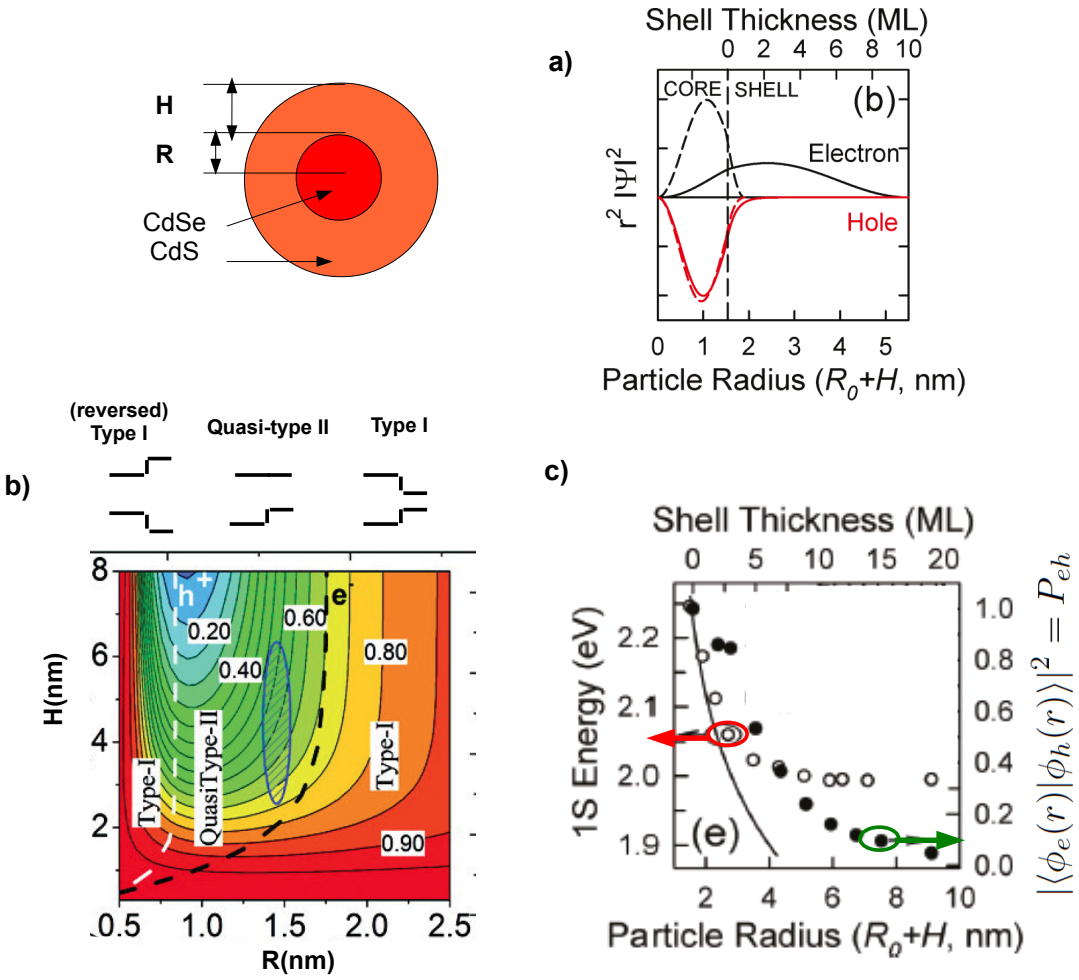

Figure 1.11: CdSe/CdS core/shell nanocrystals as a quasi type-II heterostructure, R is the core radius and H the shell thickness. a) Electron and hole wavefunction localization for a shell thickness of $H = 0.4nm$ and $H = 4nm$. b) Contour plot of the calculated electronhole overlap integral P_{eh} (red $P_{eh} = 0.9$, blue $P_{eh} = 0.2$) as a function of the core radius R and of the shell thickness H. White and black lines are boundaries between different localization regimes. They correspond to the condition that the electron wavefunction (white dashed line) or the hole wavefunction (black dashed line) are equally distributed between the core and the shell [39]. c) Empty circles (left axis): spectral position of the PL emission peak for CdSe/CdS nanocrystals with core radius $R = 1.5nm$ and different shell thickness H (expressed in nm or in CdS monolayers ML). Full circles (right axis): the electron-hole overlap integral P_{eh} derived from the measured lifetime as a function of the thickness. Measurements from [39].

Strain: According to ab initio calculations in [55], band alignment depends also on the strain, because it can change the lattice constant, Fig. 1.10 b). In CdSe/CdS heterostructures this strain-induced effect causes a quasi type-II alignment to be more probable. The strain can also cause an energy barrier between the core and the shell. It is important to consider the strain

when nanocrystals are studied as a function of the temperature, because the lattice parameters of the core and shell depend on the thermal dilatation.

Alloying at the core/shell interface: High growth temperatures and large shell thickness can also favor an alloying process at the interface which contributes to modify the band alignment of bulk materials, like in giant shell CdSe-CdS spherical nanocrystals [39].

1.5 Core/shell systems of anysotropic shape: CdSe/CdS dot-in-rods

Among the CdSe/CdS heterostructures that have been fabricated so far there are spherical core/shell nanocrystals, giant shell nanocrystals [56] [57], dots-in-rod [40] [16], rods-in-rod [50] and tetrapods [58].

Here we will focus on CdSe/CdS dots-in-rod (DR), where a spherical core is embedded in a CdS cylindrical shell. CdSe/CdS DRs were the first systems where the growth of a 1D anisotropic (rod-like) shell on a 0D isotropic core nanocrystals has been achieved.

In the original synthesis by Talapin [40], the CdS shell growth was carried out by the slow addition of organometallic Cd and S precursors. Crucial points for the anisotropic growth were the use of a relatively low reaction temperature of $130°C$ and of an excess of the sulfur precursor (Cd/S=1:3-1:5). The asymmetric shell growth has been rationalized by the different reactivity of the facets of the hexagonal CdSe core NCs and their different lattice mismatch with CdS.
The obtained nanocrystals exhibited linearly polarized emission with high QYs in the range of 70%, large Stokes shifts and a high extinction coefficient $10^7(mol * cm)^{-1}$ at 340nm for DRs with an aspect ratio of 4:1)[40].
In this synthesis process the core is always located at one end of the shell and the Stokes shift increases with the aspect ratio. DRs have the same diameter as cores at low synthesis temperature, whereas at higher temperatures $(140 - 180°C)$ also the diameter starts to increase. At $280°C$ an isotropic growth of the shell was observed.

Seeded-growth approach Dot-in-rod systems were further optimized in the so-called *seeded growth* approach [16]. This is a new synthetic procedure, which relies on the rapid injection of CdSe seeds and elemental sulfur dissolved in hydrophobic TOP (trioctylphosphine), into a solution of CdO in a mixture of TOPO (trioctylphosphine oxide), hexylphosphonic acid and octadecylphosphonic acid at high temperature ($350 - 380°$C). In the original work [16] aspect ratios as high as 30:1 were obtained together with a narrow distribution of lengths and diameters (monodispersity). The diameter of the studied rods varied between 3.5 and 5 nm, and the lengths ranged from 10 to 150nm.

Since nucleation is bypassed by the presence of the seeds, all nanocrystals experience very similar growth conditions resulting in a narrow distribution of lengths and diameters. In fact, if no CdSe seeds are co-injected into the primary solution, CdS nano-rods start nucleating after several seconds after the injection, and a large distribution of geometrical parameters is obtained.

This huge shape anisotropy and the homogeneity assured by the seeded growth synthesis is

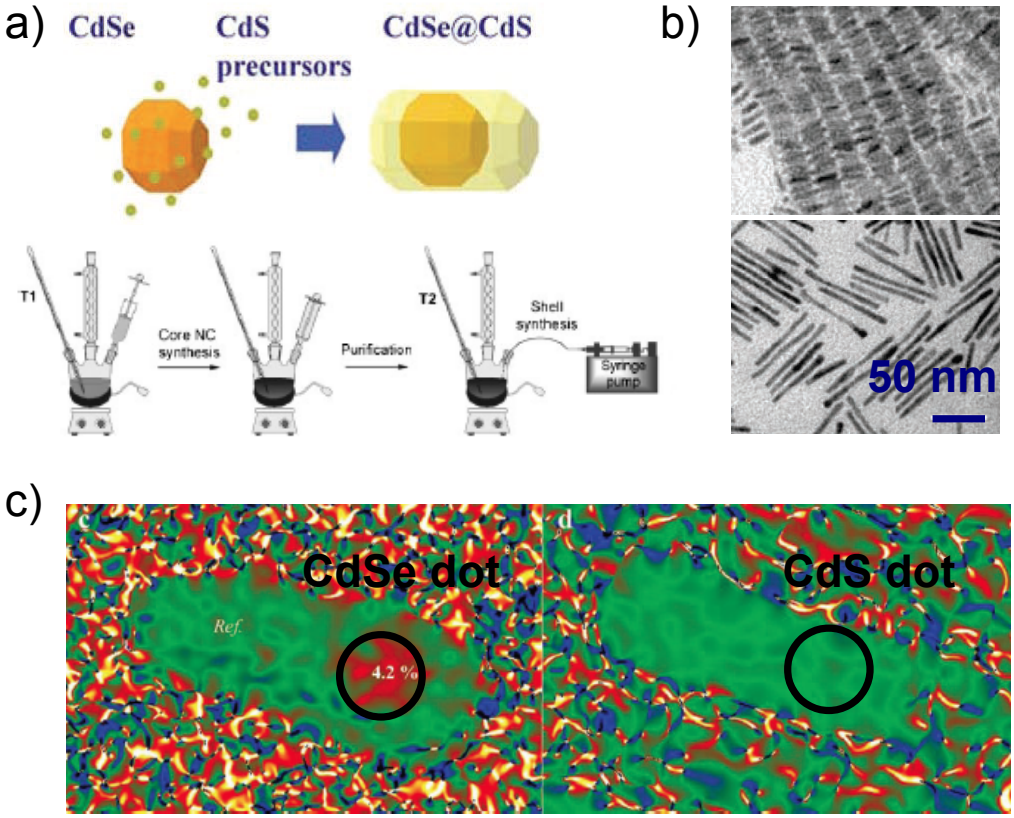

Figure 1.12: a) Sketch of the seeded-growth synthesis of CdSe/CdS DR. b) Transmission electronic microscope (TEM) images of 2 samples of DRs. c) High Resolution TEM (HRTEM) images of one single CdSe/CdS dot-in-rod and a CdS rod grown by the same technique around a CdS core. Color scale shows the variation in the periodicity of the HRTEM contrast. Areas of the same color are regions with the same periodicity. The mean dilatation image of the CdSe/CdS DR shows an area with lattice parameters altered by 4.2% with respect to the reference area, situated at the opposite tip of the rod. This allows to localize the core inside the rod-like shell at about 1/3 of the rod length. The same analysis for CdS-only rods displays no variation of the lattice parameters over the whole length of the nano-rod. Images taken from ref. [16].

essential for realizing self assembly on a substrate and ordered arrays of rods over large areas. The ability to respond to external bias like electric field (thanks to their intrinsic dipole moment) is essential for many applications. For example, a laser, based on the self assembly of DRs, has been demonstrated [41].

The seeded-growth synthesis is rather flexible, since there are many parameters which can

be tuned in order to control the morphology of the resulting DR. The mean rod diameter can be controlled by the growth temperature: higher temperatures result in thicker shell. The rod length, on the other hand, can be varied not only by the amount of precursors and/or seeds added, but also by the growth temperature and/or the reaction time. In both cases, the size of the seeds plays an important role: small seeds, for example, tend to form long and thin rods. However, it is important to underline that growing a DR with specified parameters of core diameter, rod thickness and rod length requires a careful tuning of all synthesis parameters and that there are limitations to the growth process. For example it is very difficult to grow thick shell on a small dot.

From the point of view of optical properties, DRs are characterized by high QY (70% for low aspect ratio (AR), decreasing with AR), high polarization of the emission, tunable emission from green to red. A detailed review of the most relevant results obtained in the last few years in the field of DRs, especially from the point of view of the optical characterization, is provided in the next section.

1.5.1 General properties of CdSe/CdS dot-in-rods

DRs have some remarkable features, which come from a mixture of properties of the rod-like shell and the spherical core, and which make them appealing for many practical applications.

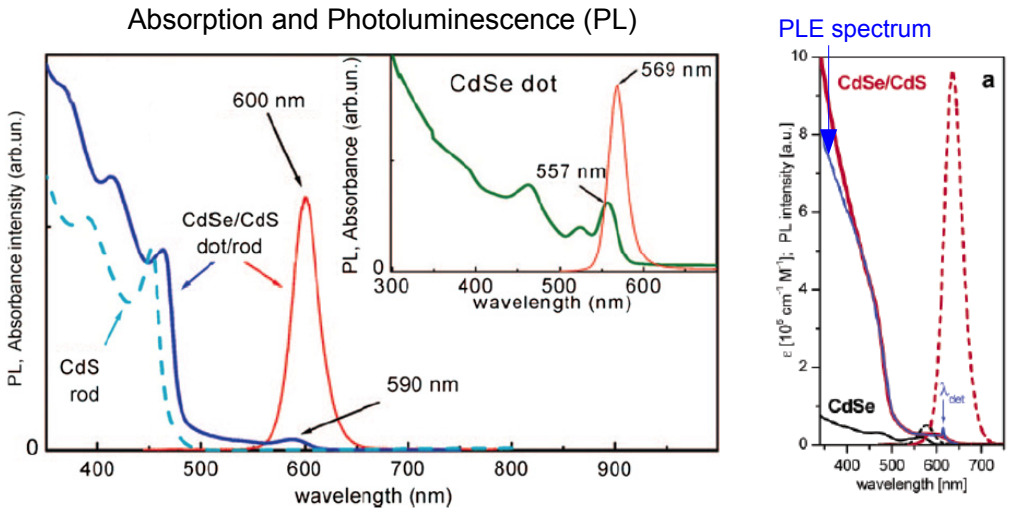

Figure 1.13: Left: an example of absorption (blue line) and PL emission spectra (red line) of CdSe/CdS DRs. Dashed blue line is the absorption of a CdS rod. In the inset: Absorption and PL of only CdSe cores. Right: Photo-luminescence emission (PLE) spectra measured at λ_{det} by exciting at specific wavelength along the absoption spectra.

Absorption and emission spectra Typical absorption and emission spectra from an ensemble of DRs in solution are shown in Fig. 1.13. In dots-in-rod, the absorption is dominated by the CdS shell, which acts like a large antenna capable of harvesting the excitation light. In [16] theoretical absorption spectra were calculated using the envelope function approximation for a sphere of CdSe embedded in a hexagonal prism of CdS and considering a zero conduction band offset. Theoretical calculations are in agreement with experimental spectra and show that the high energy peaks can be ascribed to the absorption from CdS shell while the lowest energy peak is due to electronic transition from the holes confined in the CdSe core to the electrons delocalized throughout the whole nanocrystal structure, because of the small offset. This behavior was observed also by Peng [34] in spherical CdSe/CdS nanocrystals.

The photo-luminescence emission, on the other hand, originates from states related to the CdSe core. This is experimentally confirmed by 2 observations:

(1) The emission peak is red-shifted with respect to the lowest CdSe absorption peak (Stokes shift). This (non resonant) Stokes shift is of about 40 meV (10 nm) for a wide range of aspect ratios and dot diameters, and it is similar to what is observed in only-core CdSe samples [40]. An example is shown in Fig. 1.13 (left): the PL peak is at $600nm$ and the absorption edge at $590nm$ for DRs, and at $569nm$ and at $557nm$ for the CdSe dots.

(2) In PL emission (PLE) measurements, PL is measured for a specific wavelength, while scanning different excitation wavelength. Carbone et al. [40] have found a phonon replica at 26 meV, which is exactly the same energy of the spherical CdSe dots.

Pump-probe transient absorption experiments show that the relaxation of carriers from high energy levels of the shell into the core is efficient (tens of ps). This relaxation was also observed in PLE spectra [40], which perfectly superpose with absorption spectra, as shown in Fig. 1.13 b): this implies that the PL emission always comes from the lowest energy levels.

However, as we will see in the next sections, the electronic structure of DRs can be complicated and strongly dependent both on geometrical and synthesis parameters and it is not fully understood yet. This is mainly due to the peculiar conduction band alignment of CdSe and CdS that was described above, which, in DRs, is determined by the interplay between many degrees of freedom, like the core size and shape, the shell thickness and length, the growth temperature.

Electronic structure No clear models exist of the electronic structure of DRs. In a recent paper Sitt et al. [46] have calculated the first excited states using the effective mass model described previously. They assumed a bulk conduction band offset $\Delta = 0.3eV$ and use a zero-order perturbation theory (independent electron and hole wavefunctions) to calculate Coulomb and exchange energy corrections for exciton and multi-excitons. Their results are summarized in Fig. 1.14 for different core diameters. According to Fig. 1.14 a) the second electronic level should be always in the CdS shell, while the band edge level may be localized into the core or delocalized, depending on the core size. In the inset, the predicted electronic wavefunctions for core diameter $d = 2nm$ and $d = 4.8nm$ are plotted, showing that in both cases they are preferably located around the core region. Ab initio calculations [55] have found that the band offsets change when the shell is grown because of the strain between core and shell, creating a

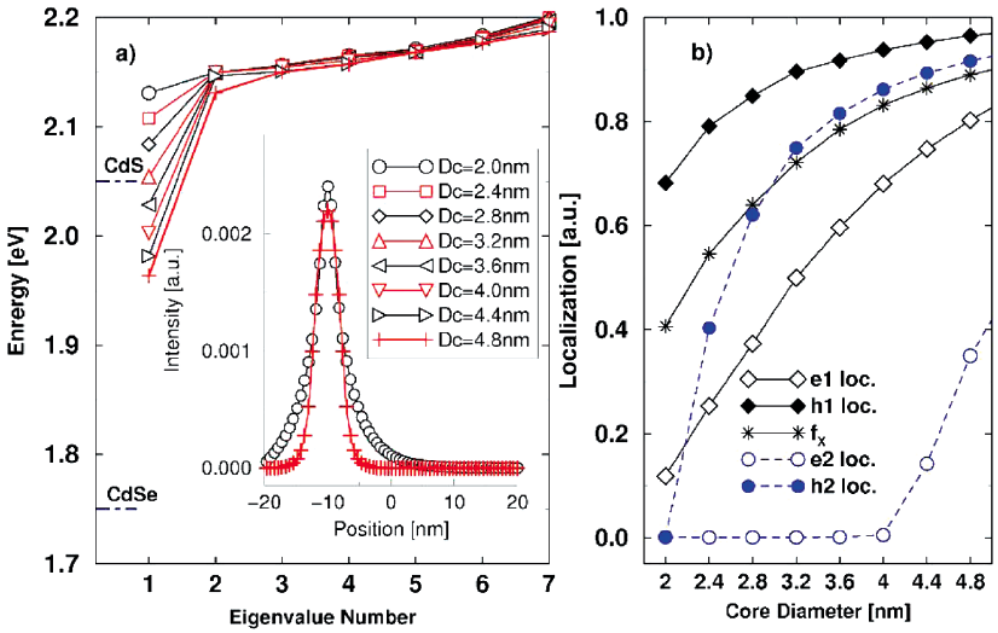

Figure 1.14: Computed electronic structure of CdSe/CdS DRs with different core diameters d and length=40 nm and thickness=6 nm, and conduction offset $\Delta = 0.3eV$. (a) Lowest seven electron eigenvalues. The CdS and CdSe conduction band edges are also shown. Inset: First electronic wave function along the main axis (-20 to +20 nm) of the rod for d=2.0 and 4.8 nm. (b) Core localization for the the first 2 electronic and hole states and the oscillator strength f_x of the fundamental transition. Core localization is defined as the integral of the electron (hole) envelope function inside the core. Figures taken from ref. [46]

quasi-type II conduction band offset ($\Delta \simeq 0$). However, due to the Coulomb interaction the electron wavefunction will be likely localized surrounding the hole. This leads to results similar to [46]. They have also found out that the band gap depends very much on the kind of atoms which are on the shell surface.

The DR length is not expected to play a main role on the electronic structure, in agreement with calculations and experiments in only CdSe rods. In fact, the polarization and spectral properties of rods do not depend much on the length after a critical aspect ratio AR, which is less than 1.5 regardless the diameter.
Core diameter and shell thickness seems to be more important parameters in order to determine the electronic structure. On the other hand, DR length and its AR can intervene in many indirect ways, for instance by controlling the dielectric confinement, or the surface properties, like the dipole moment induced by surface charges.

Even the fine structure in DRs has not been clarified yet. As we saw before, the lowest excited state of wurtzite spherical nanocrystals has a hole angular momentum $J_z = 3/2$ and it is optically forbidden along the crystallographic axis (c-axis). Its transition dipole moment is orthogonal to the c-axis ($\pm 1L$ state). A non spherical shape, like a CdSe rod [27], can swap $J_z = 3/2$ and $J_z = 1/2$ states, because of the shape factor (see Fig. 1.5).

Growing a rod-like CdS shell on a spherical CdSe core can have the same effect as in pure nano-rods. A change of the fine structure with respect to spherical nanocrystals could be attributed, for instance, to the Stark effect or to a modification of the shape of the core, induced by the growth of the asymmetric shell.

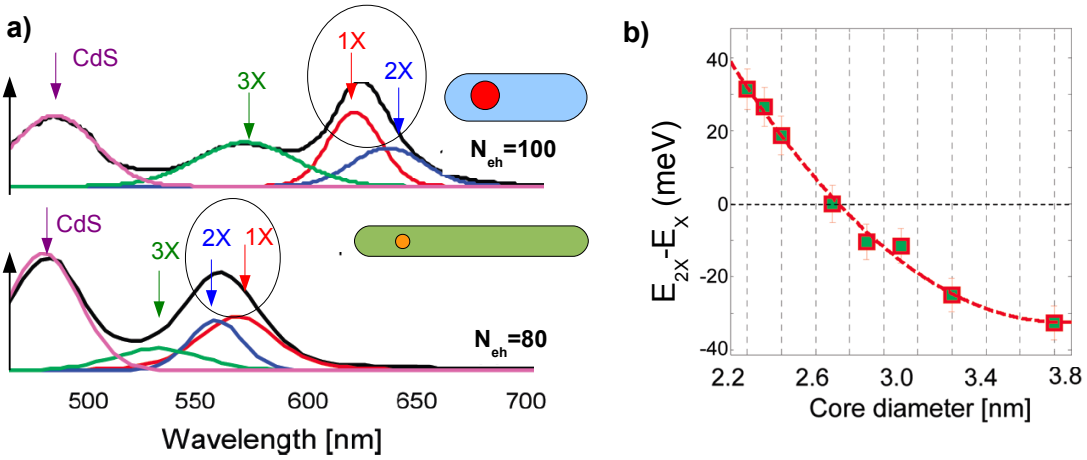

Figure 1.15: a) Photo-luminescence spectra at high excitation intensity $N_{eh} \simeq 100$ for 4 nm diameter CdSe cores embedded in 45 nm long and 6 nm thick CdS rods (up) and for 2.2 nm diameter CdSe cores embedded in 114 nm long and 4.7 nm thick CdS rods. Multi-exciton peaks: exciton (red), biexciton (blue), triexciton (green) and CdS exciton (magenta). b) The crossover from negative values (attractive biexciton binding energy) to positive energies (repulsive biexciton binding energy) is a signature of the transformation of the system from type-I to (quasi) type-II. Figures taken from ref. [46]

Electron delocalization: quasi type-II heterostructure Many pump-probe experiments suggested that the electron wavefunction must be delocalized in the shell. Even exciting only the core there is a transient bleaching of the absorption in the shell. This means that either the electron or the hole levels of the CdS shell are populated directly by the core absorption.

The red-shift of the emission and absorption spectra with respect to core-only samples confirms a quasi-type II behavior.

The red-shift increases with rod thickness and decreases with increasing core diameter [43]. Also in spherical CdSe/CdS a similar trend was observed [44], and it is summarized in Fig. 1.11.

No evident dependence on the rod length, at least for long lengths, has been observed. This

is also confirmed by envelope function calculations for CdSe nano-rods [25], where after 20 nm there is no more length dependence.

In many of the DRs studied in this thesis the Auger effect is still efficient and prevents the emission from multi-excitons, as explained in the next chapters.
However, in some cases the Auger recombination can be not very efficient in DRs. For example a suppression of the Auger recombination rate was observed in [45], which was assigned to the electron delocalization along the rod [22].
In the case the Auger effect is not very efficient, the emission from multi-excitonic states can be observed. In [46], by measuring the photo-luminescence spectra at high excitation, the authors have found a transition from a prevalently type-II (more than half of the electron wavefunction is delocalized into the shell) to a prevalently type-I regime (more than half of the electron wavefunction is localized into the core) for a core diameter of 2.7 nm, see Fig. 1.15. This is done by measuring the energy difference between the bi-exciton and the exciton peak, as illustrated in Fig. 1.15 b).
However, in these measurements both the shell thickness and the length change for each core sample, but, as it is evident in Fig. 1.11 b) for spherical CdSe/CdS nanocrystals, at least the shell thickness should be taken into account. Therefore the problem of determining a transition between type II and type I electron localization in DRs is still open.

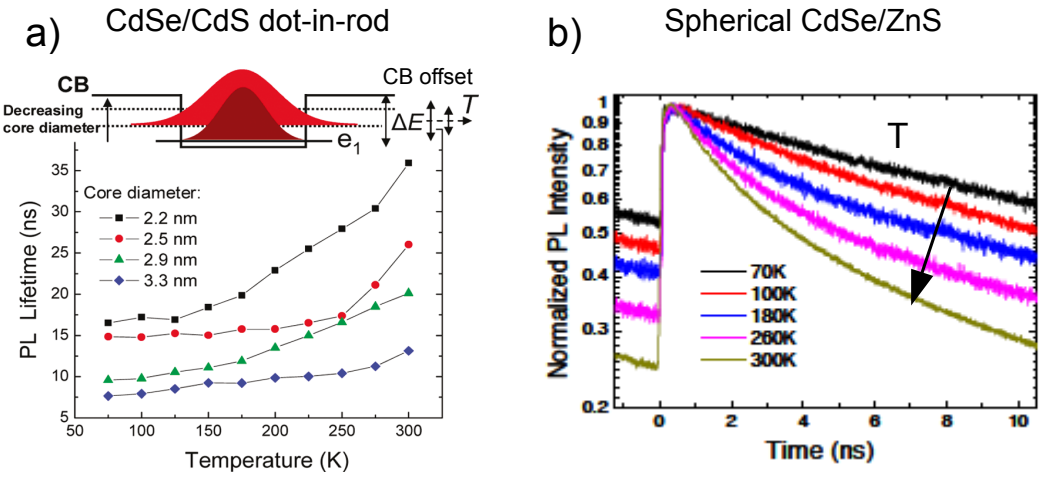

Figure 1.16: Photo-luminescence decay lifetime as a function of temperature for a) CdSe/CdS dot-in-rods and b) spherical CdSe/ZnS nanocrystals [42]. Increasing the temperature in (thin shell) DRs leads to a longer radiative lifetime, while in spherical nanocrystals the opposite behavior is observed.

Lifetime and PL spectra at low temperature The radiative lifetime is inversely proportional to the electron-hole wavefunction overlap integral P_{eh} and thus it depends on the electron delocalization.
In quasi-type II nano-structures the electron delocalization is usually positively correlated with a red-shift of the band-edge emission with respect to only CdSe core system. However, lifetime and spectral red-shift can have different behaviors, as we have already mentioned for spherical CdSe/CdS nanocrystals. In fact, as shown in [44] for giant shell nanocrystals, the red-shift saturates with the shell thickness (the core radius is fixed), whereas lifetimes increase with the thickness, according to the decrease of the electron-hole superposition shown in Fig. 1.11 c). The exciton radiative lifetime has been found to increase with increasing the temperature [42], a feature which has not been reported neither for CdSe/ZnS nor for CdSe/CdS spherical nanocrystals. Fig. 1.16 shows clearly a different behavior. In CdSe/ZnS nanocrystals the lifetime decreases with increasing the temperature and becomes non exponential. The evolution of lifetimes with T in spherical particles can be explained by the thermal population of the fine structure levels, as previously described. In DRs the measured lifetimes are mono-exponential [42] and they increase by increasing the temperature.

These results have been interpreted by assuming a temperature-dependent conduction band offset between core and shell, the electron being more and more localized into the core at low temperature. A blue-shift of the emission spectrum at low temperature is also observed in spherical nanocrystals, because the thermal contraction of both core and shell increases the charge confinement (especially of the hole).
It is well-known that an increase in temperature (or pressure and strain) alters the conduction and valence band energies in semiconductors and semiconductor nanocrystals. This is mainly due to the interaction with the lattice vibrations and to a volume change [42].

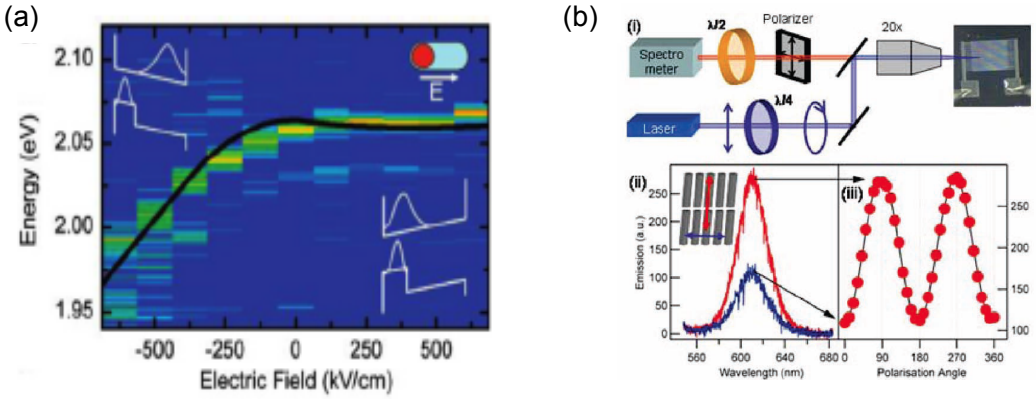

Figure 1.17: a) Shift of the PL spectra in a single CdSe/CdS DR as a consequence of the band bending induced by Stark effect [47]. b) Linear polarized emission measured from an ensemble of aligned DRs [16].

Surface, dipole moment and Quantum Confined Stark effect In DRs the surface plays a main role because more atoms lye on the surface as compared to spherical QDs with the same total number of atoms [54].

Surface plays an essential role in 2 different senses:

(1) **Passivation**. DRs may be more sensitive to the surface passivation than spherical QDs. Normally the photo-luminescence QY in DRs are higher than in spherical QDs with the same volume, probably because the seeded-growth leads to less interfacial defects and trap states. However, the atom termination of the external CdS shell is essential: for example, it is well-known that an anion rich surface (like anions $S^{(2-)}$) gives rise to deep hole traps [54] [55]. Chemical and photo-stability, as well as photo-charging and photo-luminescence fluctuations in DRs can thus be very sensitive to the surface properties.

(2) **Surface charges**. The role of surface charges in DRs on the emission properties have been studied by Müller in 2 papers [47] [48]. In DRs, with respect to spherically symmetric nanocrystals, charge fluctuations can strongly influence the electronic level structure via a giant quantum confined Stark effect (QCSE). In [48] it was shown that if a charge is close to the core, the PL peak is red-shifted and broadened by the Stark effect, while if the charge is localized far away, PL is at higher energies and less broadened. Anyway, DRs studied in [48] were synthesized by the low temperature method described in [40], while another group [49] showed that in seeded-growth DRs fluctuations of the energetic position are much smaller (few meV). If there are surface charges they are more likely to stay in a fixed position.

In [47] the effect of an external electric field has been studied and, as a consequence, the possibility to tailor the wavefunction distribution. A longer lifetime connected with a reduction of the charge overlap is associated with a red-shift because of the *band bending* induced by the electric field, as shown in Fig. 1.17 a). This can be important to understand spectral and lifetime fluctuations inside a sample.

Several experiments studied the permanent dipole moment in colloidal QDs and nano-rods with both wurtzite and zinc-blende structures [49]. The existence of a permanent ground-state dipole moment along the c -crystallographic axis in CdSe/CdS DRs relies on the crystallographic deviation from the ideal wurtzite structure and it was found to scale with the nanostructure volume. A dipole moment is also responsible for DR-DR interactions and makes them sensitive to electric fields. Self-assembling procedures are based on this intrinsic property [16].
A permanent dipole moment can also generate an internal electric field and thus it can be source of a Stark effect.
A further contribution to the internal field comes from the piezoelectric polarization induced by both the high piezoelectric constants and the elastic strain due to the lattice mismatch (about 4%) between CdSe and CdS at the heterostructure interface [49].

Linear polarization of the emission A high degree of linear polarization both in single nanocrystal and in ensemble measurements has been reported for DRs in [40], [16] and more recently in [50], where DRs are compared with CdSe nano-rods and CdSe/CdS rod-in-rods

structures. Fig. 1.17 b) shows an example of polarization measurements on an ensemble of aligned DRs [16].

Many factors can be at the origin of the measured degree of polarization.
We have already discussed the role of the electronic and of the fine structure in CdSe nano-rods, and how the swapping of fine structure levels can affect the polarization of the emitted photons. As we said, this swapping can occur for very low aspect ratios (1.2-1.3), also depending on the rod diameter.
In DRs the shape of the core could be modified by the strain induced by the growth of the cylindrical shell, resulting in a pronounced prolate shape for the CdSe core.

Moreover, like in CdSe pure nano-rods, also geometrical factors play a role in the polarization of the emission. The cylindrical shape of the shell could influence the electric field distribution via a quantum dielectric confinement [28].
The internal electric field, induced for example by an intrinsic dipole moment, could also enhance the degree of polarization by separating the electron and hole wavefunctions along the rod c-axis.

Temperature dependent polarization measurements should help to distinguish between the band structure and the geometrical contribution, as the first is expected to depend on the temperature, as described in the section devoted to the fine structure, while the second one should not.
The physical explanation of the polarization properties of DRs is still an open problem.

Chapter 2

Blinking and single photon emission in colloidal nanocrystals

Introduction In the first part of this chapter I will review two central concepts in the photophysics of colloidal nanocrystals, which are the main subjects of my experimental work: photoluminescence blinking and single photon emission.
After having introduced the most commonly used models accounting for the blinking and photocharging mechanisms, the subject of blinking suppression is addressed.
The general problem of building a triggered single photon source is then discussed. The origin of non-classical light emission at room temperature in colloidal quantum dots is explained. All the possible connections between blinking suppression and single photon emission are carefully analyzed.

The second part will be devoted to the experimental methods that are used to study and characterize the optical properties of single quantum emitters in this thesis: confocal microscopy and time correlated single photon counting (TCSPC). I will describe measurements and data analysis commonly performed from TCSPC to characterize blinking and photon statistics and which kind of information can be extracted about the fundamental physics of colloidal nanocrystals.
A special place will be reserved to the intensity auto-correlation function, an essential tool for studying the photon statistics of non-classical states of light.

2.1 Photo-luminescence blinking

When observed on the individual scale, the emission of colloidal nanocrystals is often blinking on and off intermittently, a process known as photo-luminescence (PL) intermittency or blinking [66]. photo-luminescence blinking was observed for a wide range of single emitters, including single molecules, fluorescent proteins, polymer segments, semiconductor nanoparticles, nanorods and nanowires. Basically, all known types of fluorophores studied so far exhibit fluorescence intermittency [61]. PL blinking was first reported to occur in single nanocrystals by Nirmal et al. in 1996 [62]. In this initial experiment the fluorescence of single CdSe nanocrystals, with and without a ZnS shell, were measured.

To characterize blinking and to extract the underlying dynamics responsible for this process, it is usual to compile histograms of the duration of on and off events. This is made by setting a suitable intensity threshold to discriminate between both types of events as exemplified in Fig. 2.1 (grey lines).

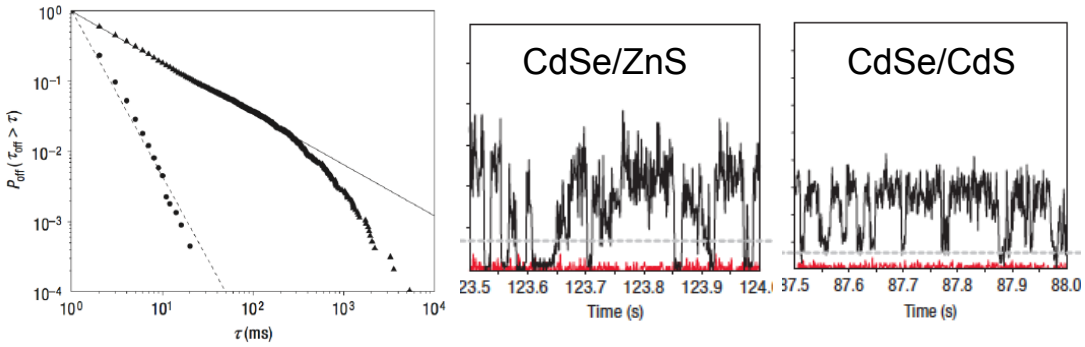

Figure 2.1: Cumulative distributions of off times in a double-logarithmic scale for CdSe/ZnS nanocrystals (triangles) and for thick shell CdSe/CdS nanocrystals (circles) [73]. On the right: PL timetraces from which the cumulative distributions are calculated. In red the noise level, in grey the threshold used for discriminating on and off periods.

In this analysis it is common to assume a binary blinking, i.e. the intensity can either be on (above intensity threshold) or off (below intensity threshold). Unlike the case of single molecules, a common feature to most of the colloidal nanocrystals of the first generation is that the histograms of the durations of on- and off-times display a highly non-exponential character. The probability distribution functions compiled from these histograms are usually described by inverse power laws, typically heavy tailed power law distributions.

Until 2008, i.e. until the first attempts to suppress blinking in colloidal nanocrystals, the challenge for theoreticians was to interpret the observed blinking kinetics, characterized by a large distribution of periods of high fluorescence (on-state) and low fluorescence (off-state) spanning from hundreds of microseconds to hundreds of seconds.

In this thesis we will often deal with nanocrystals showing suppressed blinking, where off states are quite rare. Photo-luminescence fluctuations are still present, but they occur mostly between an on-state and a lower intensity *grey state* and their kinetics is faster than in original nanocrystals. The photo-luminescence fluctuations between two or more intensity levels, which are not properly resolved, are also called flickering. In the following we will refer to blinking only if the PL fluctuations occurs between on states and proper off states.
Even if the dynamics can be different in the so called non-blinking nanocrystals, we think that it is very useful to describe the models for on-off blinking developed so far, because they provide a necessary insight into the basic physics causing PL fluctuations.

2.1.1 Models of photo-luminescence blinking

It is generally agreed that fluorescence blinking is a direct consequence of the trapping of charge carriers. However, the details of the underlying mechanisms are still very debated [60].
Two approaches have been developed in the literature to link the charge trapping with the off (or grey) periods observed during PL blinking.

The first kind of models, here referred to as Type A models (also called charging models) assumes that the charge trapping leaves the nanocrystal core effectively charged. This is also called a ionization process. The Auger recombination is an efficient non-radiative decay pathway for the charged nanocrystal, which causes a low fluorescence QY for a duration dictated by the lifetime of the trapped charge.

The second kind of models, here referred to as Type B models, assumes that the trapped charge can recombine non-radiatively with its countercharge promptly after each excitation event. In this case, low fluorescence quantum yield periods are associated with fast charge-trapping rates, while intermittency is caused by time-dependent fluctuations in the trapping rate.

Type A blinking A schematic illustration of the key processes for Type A models are shown in Fig. 2.2 a) (upper panel).

The high fluorescence intensity on-state is the result of continuous cycling photon absorption to create an exciton, followed by radiative recombination. An on-to-off switching occurs via thermal ionization or Auger-assisted photo-ionization of a charge carrier to a trap state [63]. The trapped charge (a hole in Fig. 2.2 a)) leaves a delocalized charge of opposite sign inside the nanocrystal. The resulting charged nanocrystal remains non-fluorescent, despite the subsequent absorption, because of the fast non-radiative Auger energy transfer from the new generated excitons to the spectator charge. The off-to-on switching occurs when the trapped charge returns into the nanocrystal and neutralizes it, typically via a relaxation process.
The main role of the Auger effect in the photoionization process was supported in the first blinking measurements by a decrease of the average duration of the on periods with higher excitation intensity [62]. We will talk about the photoionization, or photo-charging, process more deeply in the next section.

A simple single-rate model is not enough to explain the complicated experimental results concerning off and on time distributions and spectral diffusion. That's why many different and refined theoretical models have been elaborated which can account for one or more experimental facts, but not for all of them at the same time. In Fig. 2.2 a) (lower panel), which is taken from ref [60], some of these models are sketched just to give an idea of the possible processes, but we refer to [60] for a complete treatment.

Type B blinking Type B models do not require an efficient Auger recombination [64].

In this case the nanocrystal returns to the neutral ground state after each excitation event. Charges are trapped at each excitation cycle, and when they are trapped they always prefer to recombine non-radiatively because the non-radiative rate is larger than the radiative rate. Here what determines the PL intensity is not the competition between radiative and non-radiative

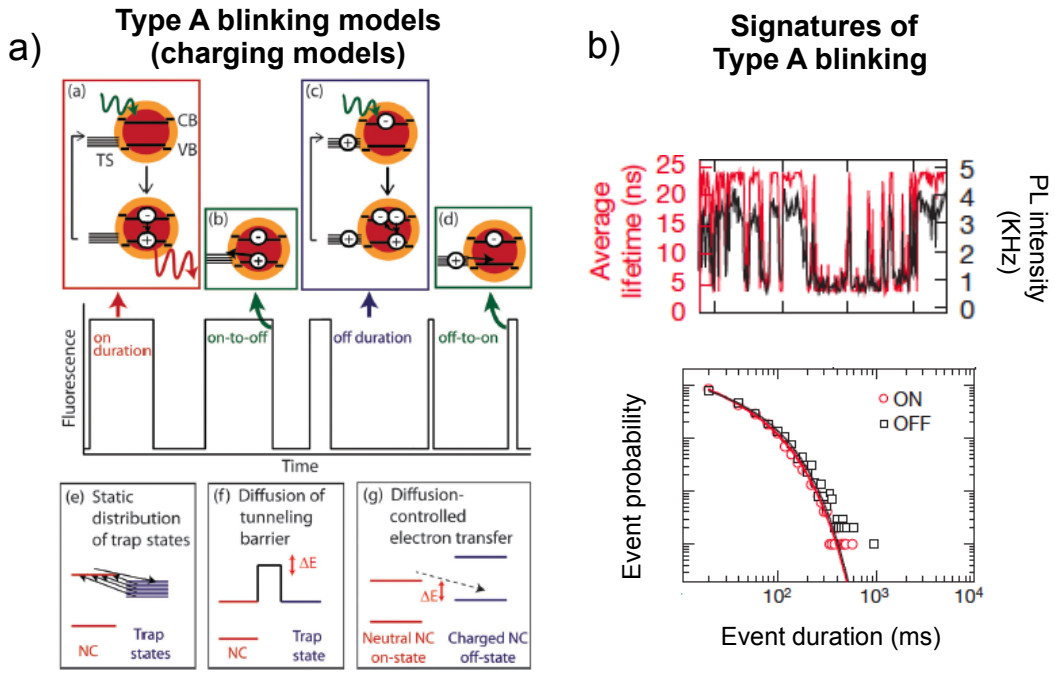

Figure 2.2: a) Sketch of the key processes in Type A blinking (upper panel), and some proposed models of photo-charging. b) Signatures of Type A blinking, as measured in [65]: correlations between intensity fluctuations and lifetime (upper panel) and exponential distribution of on and off (grey) times (lower panel).

decays (since the condition $\gamma_{NR} \ll \gamma_R$ is always verified), but the competition between the radiative rate and the trapping rate. Blinking is associated with fluctuations of the trapping rate: the nanocrystal remains in an off-state when the trapping rate is much faster than the radiative recombination rate. A schematic illustration of Type B blinking mechanisms is shown in Fig. 2.3 a) and the key steps are described below.

An on period occurs when the trapping rate is considerably slower than the fluorescence rate and the nanocrystal cycles between photon absorption to create an exciton and its radiative recombination. The switching from the on to the off state occurs when the trapping rate becomes much faster than the fluorescence rate. During an off duration the nanocrystal cycles between photon absorption to create an exciton, fast removal of the charge (a hole in the figure) to a trap state, and non radiative recombination of the electron and trapped hole. Off-to-on switching occurs when the trapping rate becomes very slow again. This can be due, for instance, to a change of the distribution of trap states on the surface.

Therefore, for Type B models the off duration is determined by the time the trapping rate remains very fast, and not by the lifetime of the trapped charge (as was the case in Type A models). The low photo-luminescence quantum yield of the off-state is not a result of the Auger

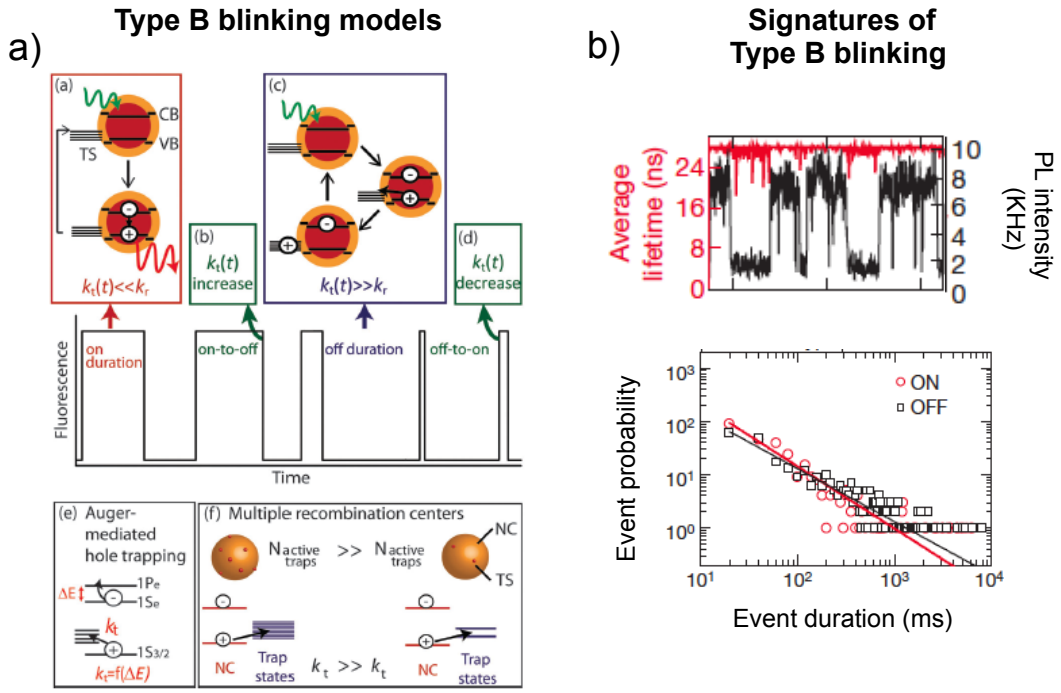

Figure 2.3: a) Schematics of the basic steps in Type B blinking (upper panel) and some models which try to explain the fluctuations of trapping rates (lower panel). b) Experimental signatures of Type B blinking as put in evidence by [65]: intensity fluctuations without corresponding lifetime change and power law distribution of on and off (grey) times.

recombination (as was the case in Type A models).

It is likely that blinking is due to a combination of both Type A and Type B models. This would explain the cross-over from power law to exponential behavior of the on-state distributions, observed in many experiments. It could be associated with a combination of a distributed-rate (typically type B) and a single-rate blinking process (typically type A), without need for a single complicated model taking into account all the experimental features.

Signatures of Type A and Type B blinking A recent experiment reported that two types of blinking can be observed for one single CdSe/CdS nanocrystal [65]. In this work the experimental signatures of these two different blinking behaviors are described, and they will be summarized here.

In Type A blinking, correlated fluctuations of the photo-luminescence intensity and lifetime are expected and they were observed experimentally by several groups [88] [89] [90]. When a nanocrystal is in a charged state, the three-particle Auger recombination opens a fast, non-radiative channel, resulting in a shorter lifetime and, consequently, a reduced photo-luminescence

quantum yield, as illustrated in Fig. 2.2 b). The low fluorescence intensity and the faster recombination rate measured during the grey states are both due to the competition between radiative and non-radiative Auger recombination in a charged exciton. In fact, given a measured decay rate $\gamma_i = \gamma_R + \gamma_A$, the PL intensity is determined by the definition of Quantum Yield $QY = \gamma_R/(\gamma_R + \gamma_A)$.

Moreover the expected radiative lifetime for a charged state is lower than that of the neutral exciton, because there are more recombination possibilities and thus γ_R is higher. We will discuss more specifically this point in the next section 2.1.3, when we will try to estimate the radiative and non-radiative lifetimes for different charge configurations.

In Type B blinking, intensity fluctuations occur, while the PL lifetime remains constant at a high value, as shown in Fig. 2.3 b). In [65] the periods of low intensity PL are explained by an efficient and fast trapping of high energy electrons, followed by the non-radiative recombination of the hole and the trapped electron. The nanocrystal returns to the neutral state before the next excitation event.
During an off-state the intensity is small because the fast electron trapping process competes with the thermalization from high energy states to the band-edge. The PL lifetime, on the other hand, is unchanged because the trapping process does not compete directly with the radiative recombination from the band-edge. In the case of B-type blinking, the Quantum Yield of the off state is unrelated to the charged exciton Auger lifetime. Instead, it is defined by the rate of hot-carrier trapping compared to the carrier cooling rate. As a result, it can be much lower than the QY of a charged state, defined before.

Another signature of the two different blinking mechanisms proposed in [65] is the distribution of on and off times: in the case of type B blinking, it is a power law with exponent around 1, Fig. 2.3 b), in type A an exponential cut-off must be introduced such that the distribution is fitted by

$$P(\tau) \propto \tau^{-\mu} e^{-\frac{\tau}{\tau_c}}$$

where μ is about 0.5 and τ_c is the time-scale of the fluctuations, typically in the range of ms or tens of ms.

Another interesting feature observed in [65] is that B-type blinking dominates in thin-shell nanocrystals and, therefore, is likely a dominant blinking mechanism in standard core-only CdSe and core/shell CdSe/ZnS nanocrystals studied in earlier reports.

The proposed model of B-type blinking based on hot-electron surface traps, provides an explanation of previously reported properties of the nanocrystal off state, such as low emission quantum yields [79] and the lack of a systematic size dependence of the photo-luminescence lifetimes [80], that could not be explained by the traditional charging model (type A blinking).

En passant, lifetime fluctuations are possible, but rare, in type B blinking. This happens if, instead of recombining at each excitation cycle, the nanocrystal remain in a positively charged state [65].

2.1.2 Photo-charging and Grey states

In the case of commonly studied CdSe/ZnS nanocrystals, the blinking is dominated by discrete switching between on and off states [62], or by a continuous distribution of emission states [86] [87], because of random fluctuations in the non-radiative rate $\gamma_{NR}(t)$. The distributions of on and off times typically follow heavy tailed power law distributions with not well-defined time scale.

A well defined grey state, i.e. a state characterized by a PL intensity which is intermediary between the on and the off states, was observed for the first time in CdSe/CdS core/shell nanocrystals, both by analyzing the lifetimes in ensemble measurements [88] and on single nanocrystals [89].
In particular in [90] the authors reported the simultaneous presence of both grey and off states, Fig. 2.4.

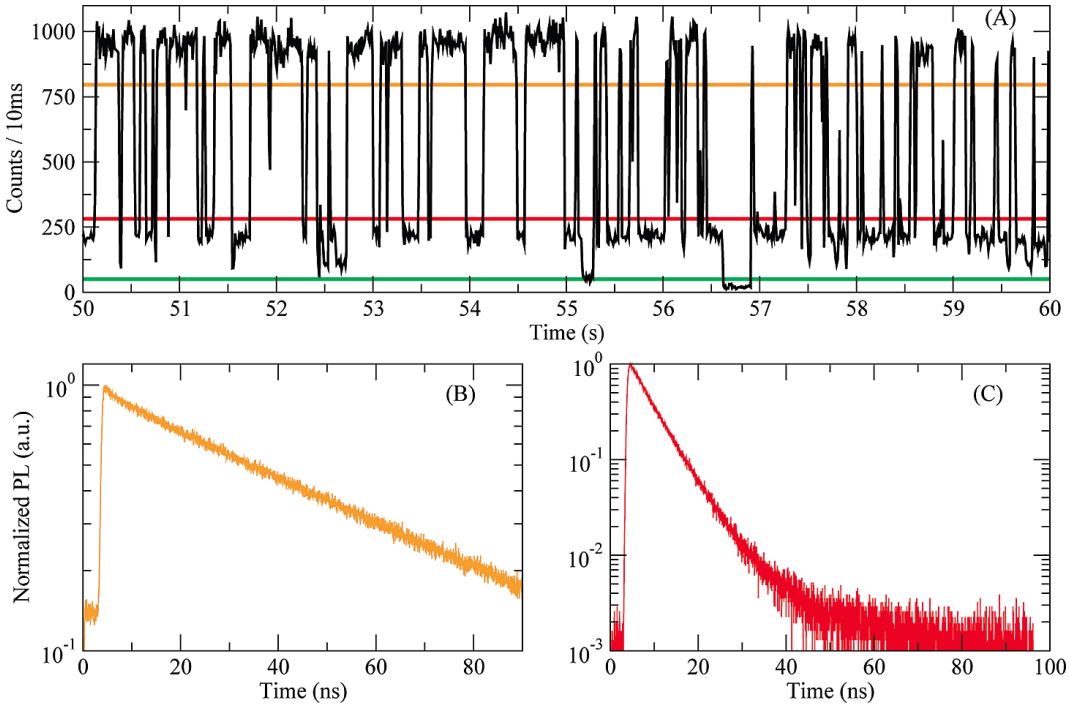

Figure 2.4: (A) Grey states and off states in the PL time-trace of a single CdSe/CdS nanocrystal. (B) and (D) Observed lifetimes for photons coming from the bright state (yellow) and form the grey state (red). Figure taken from reference [90].

In CdSe/CdS nanocrystals, the duration of both the bright and the grey state emission has usually a single (and well-defined) characteristic time constant, in the range of ms. It means that the fluctuations between on and grey states are governed by a single-rate process.
Moreover the results in Fig. 2.4 indicate that the grey state has a well defined quantum yield.

Furthermore, the grey state is also characterized by a well defined (i.e. not fluctuating) lifetime, which is lower than the bright state radiative lifetime.

The coexistence of off and grey states is coherent with the results found in [65], where the off states are assigned to type B blinking and the grey states to type A blinking.

Type A blinking is assumed to be prevalent in nanocrystals with suppressed blinking, like giant shell nanocrystals [56] or, as we will see, also in thick shell CdSe/CdS dot-in-rods. The Quantum Yield of the grey state (and its lifetime) depends on the efficiency of the Auger effect in the presence of a supplementary charge.

Photo-ionization In Type A blinking, the PL fluctuations are assigned to fluctuations of the state of charge between a neutral, bright state and a charged, grey state (or even more than one, if more than one charge is allowed).
The mechanism for the charge fluctuations in nanocrystals is likely an Auger-assisted ionization, as originally suggested by Efros and Rosen [63]. When more than one electron-hole pair are generated inside a nanocrystal by the absorption of light, the Auger decay of such multi-exciton state can lead to the ejection of a charge, a phenomenon known as Auger ionization, sketched in Fig. 2.5. This does not require high excitation intensity, since the Poissonian statistics of the excitation process leads to a significant probability for creating a multi-exciton.

The photo-ionization hypothesis has been supported by a number of experimental observations, most remarkably by the fact that the illumination can lead to the ionization of single NCs. Ionization events were observed directly with an electrostatic force microscopy (EFM) [91].

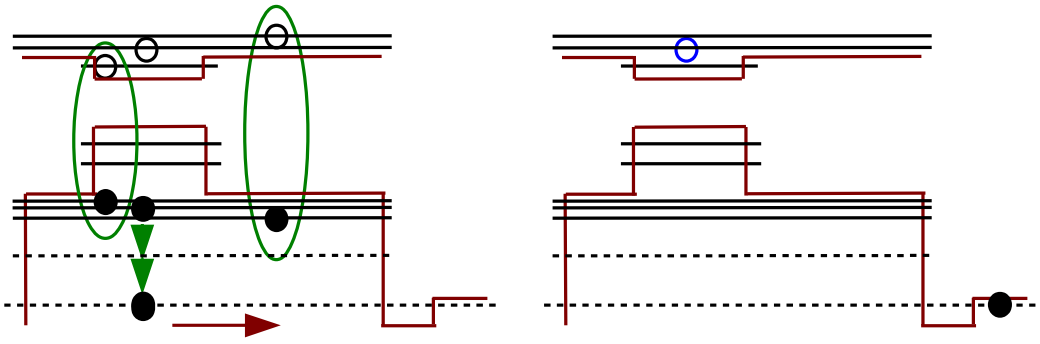

Figure 2.5: Sketch of the Auger assisted photo-ionization in a CdSe/CdS dot-in-rod, via the energy transfer to a hole (positive trion recombination). The green circles indicate an electron-hole recombination, the green arrow represent the energy acquired from the recombination (not in scale). The hole can thus be ejected and trapped, for instance, in a surface trap states, leaving a negatively charged nanocrystal.

The electron or more likely the hole trapping at the surface leaves a delocalized and mobile charge inside the nanocrystal, as illustrated in Fig. 2.5. The sign of the trapped charge will be

discussed in the next section.
This supplementary charge can efficiently quench the photo-luminescence via the non-radiative Auger recombination, as described before. In a Type A model, on states can be recovered either when the trapped charge comes back or whenever and whatever a neutral state is recovered. In any case this is referred to as a charge-separated state and not a charged state because the nanocrystal is still neutral with respect to external observation.

Positive or negative ionization? Many experimental evidence suggest that, at least in CdSe/CdS nanocrystal, and in particular in dot-in-rods, photo-ionization leads more likely to a negatively charged state.

A first qualitative consideration should be the following: since QY in CdSe/CdS core/shell nanocrystals is high, despite the quasi-type II structure and electron delocalization, it is unlikely that electrons are involved in trapping processes.

Recent experiments showed that for cold exciton (i.e. band edge), the surface trapping occurs only for the hole but not for the electron [93] [67] [94]. These observations were confirmed by theoretical calculations [85]. Hot electron trapping is still possible, as observed in [65], but in this case it is a B-type blinking and no charged state is produced.

Since photo-ionization is connected with the Auger effect, these observations suggest that electron and holes behave in a different way during the Auger recombination process. The Auger recombination is a 3-charges effect, where an electron-hole pair recombines and transfers its energy either to an electron (negative trion) or to a hole (positive trion). If many charges are present in a nanocrystal, we can always consider each elementary trion independently. Fig. 2.5, for instance, shows the Auger recombination of two positive trions, since the energy from two electron-hole pairs is transferred to a hole. We can thus define an Auger decay rate γ_A^h for the positive trion and an Auger decay rate γ_A^e for the negative trion.
If the Auger assisted photo-ionization leads more likely to a negative ionization, the Auger energy transfer to the holes should be more efficient than the Auger transfer to the electrons, i.e. $\gamma_A^h > \gamma_A^e$.

2.1.3 Statistical scaling of radiative and non-radiative rates

Lifetime fluctuations are a signature of the presence of grey states and they can give informations about the electronic wavefunction localization in DRs. In this section we want to calculate the expected radiative and non-radiative Auger rates when many charges are excited inside the nanocrystal. First of all we consider that all excitons, which are normally created 'hot', i.e. at high energy in the conduction band, have already thermally relaxed to the band-edge levels, as already described in the chapter 1, section 1.2.
We estimate the decay rates of neutral and charged excitons, single and bi-excitons, by using a statistical scaling approach. It considers the number of recombination path-ways that lead from the initial to the final charge carrier configuration, assuming that every pair or trion recombination occurs with the same basic rate [125] [126].

Radiative decay rates. The spontaneous recombination rate of an electron and a hole is proportional to the square of the transition dipole for a given electronic transition. Of course

the specific fine structure of the band-edge exciton may play an important role. As we already pointed out in chapter 1, the presence of degeneracy can influence the radiative lifetime, the spectra (dark exciton, Stokes shift) and the polarization of the emitted light.
As a first order approximation at room temperature, the fine structure can be taken into account by considering an average radiative decay rate γ_R over all the (allowed) electronic transitions of the fine structure. This approximation is expected to be valid for modelling the room-temperature PL dynamics, when the bright-dark exciton splitting is small compared to the thermal energy k_BT and thus the spin selection rules do not play a major role.
The most important factor is therefore the overlap integral of the electron and hole wavefunctions.

As for the radiative decays, a basic Auger recombination rate for a 3 charges system (negative or positive trion) γ_A^e or γ_A^h can be defined.
Given n_e and n_h the number of electrons and holes, one can thus estimate the radiative and non-radiative decay rates:

$$\begin{array}{rcl} \gamma_R(n_e,n_h) & = & n_e n_h \gamma_R \\ \gamma_A^e(n_e,n_h) & = & n_e n_h (n_e-1)\gamma_A^e \\ \gamma_A^h(n_e,n_h) & = & n_e n_h (n_h-1)\gamma_A^h \\ \gamma_{NR}(n_e,n_h) & = & n_e n_h \gamma_{NR} \end{array} \tag{2.1}$$

γ_{NR} takes into account all non-radiative processes different from Auger, like recombination from trap states, phonon scattering or energy transfer to an external matrix if present.

The measured lifetimes take into account both radiative and non-radiative rates. The measured decay rate γ_i for a configuration of n_e electrons and n_h holes is given by the sum of all radiative and non-radiative rates:

$$\gamma_i(n_e,n_h) = \gamma_R(n_e,n_h) + \gamma_A^e(n_e,n_h) + \gamma_A^h(n_e,n_h) + \gamma_{NR}(n_e,n_h)$$

For instance, an important quantity is the expected lifetime of a negatively charged nanocrystal (negative trion):

$$\gamma_i(n_e=2,n_h=1) = 2\gamma_R + 2\gamma_A^e + 2\gamma_{NR}$$

Examples of radiative and non-radiative decay rates and of their interplay are illustrated in Fig. 2.6.

2.1.4 Blinking suppression strategies

Blinking suppression has been a very hot topic in colloidal nanocrystal research in the last few years. The first strategies relied on avoiding the ionization by controlling the nanocrystal close environment. The first works were oriented to suppress surface trap states: longer on periods and enhanced ensemble PL in a solution of CdSe/ZnS nanocrystals were obtained by passivating the surface using thiolate groups [68]. Nevertheless further studies [69] demonstrated that the efficiency of thiol group to passivate the surface strongly depends on the pH of the solution. This strategy relies on the capability of thiolates to serve as electron donors for CdSe/ZnS

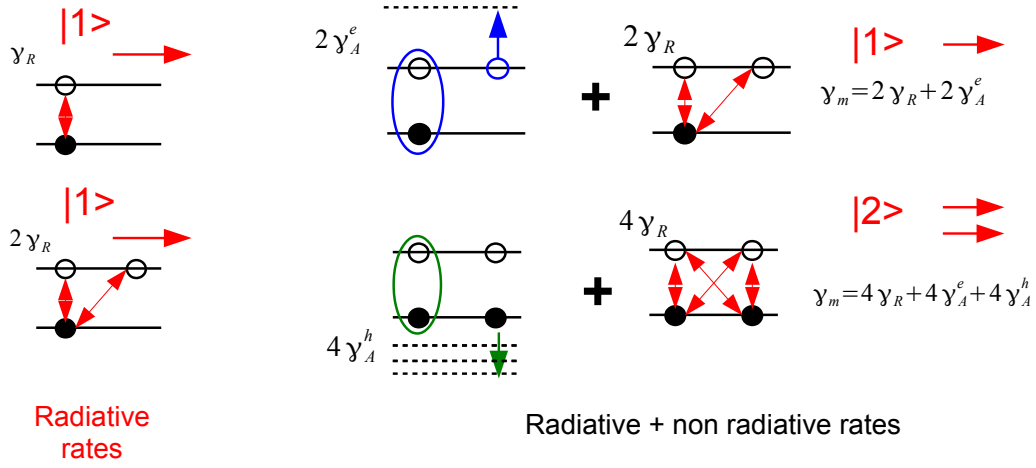

Figure 2.6: Left: Radiative decay rates for a neutral and a negatively charged nanocrystal. Right: competition between radiative and non-radiative decays. Above: the case of a negatively charged state (negative trion), where the radiative decay (red arrow) is in competition with the Auger energy transfer to the supplementary electron. The electron-hole pair in the blue circle recombines non-radiatively and transfers its energy to the third electron. Below: a bi-exciton state. In this case an Auger transfer both to the holes or to the electrons is possible. The green circle indicates an Auger recombination with energy transfer to a hole (positive trion). All the radiative and non-radiative decay channels contribute to the final measured rate γ_i of the bi-exciton.

nanocrystals, filling electron-accepting trap sites.
Other groups used different organic ligands, like electron-donating molecules [70] [71] as well as n-doped substrates [78]. However, lifetime measurements showed that blinking reduction came mostly from a reduction of the radiative lifetime of the band-edge exciton. More generally, Fomenko et al. [71] showed that these approaches based on the modification of surface states or changes in the near chemical environment lead necessarily to a parallel acceleration of both radiative and non radiative decay rates, γ_R and γ_{NR} (non Auger).

Blinking suppression is thus attained at the price of a reduction of the PL Quantum Yield, and so of the photon flux that can be provided by a single nanocrystal.

A similar consideration holds for experiments based on the electrochemical control of the state of charge, like the aforementioned case of ref. [65]. In this experiment, for instance, the neutral exciton $QY_1^{(0)} = \gamma_R/(\gamma_R + \gamma_{NR})$ is reduced to less than 0.4 because of the non radiative energy transfer to the conductive ITO substrate, which is a component of the electrochemical cell. In [65] the authors show that it is always possible to suppress blinking by inserting nanocrystals in an electrochemical cell and by applying a proper potential (positive for type A and sligthly

negative for type B blinking). On the other hand, the right potential can be very different from one nanocrystal to another and switching from type A to type B is possible by varying the voltage.

In a following report, [67] another group used the same technique as in [65]. In this case the authors state that they can suppress the grey states in CdSe/CdS nanocrystals via electrochemical control (type A blinking) but they cannot avoid transitions to the off state. Moreover they find different behaviors for thin shell and thick shell nanoparticles and different voltage conditions for blinking suppression with respect to [65]. In fact, differences both in the electrochemical cell preparation and in the sample synthesis or passivation can lead to very different results. In [67] the authors also show that the choice of a proper substrate is another key point in order to control the optical properties of the nanocrystals.

These considerations show that the approaches based on the modification of nanocrystals environment and/or of their surface properties are not very reliable and robust, at least up to now, because the possibility to suppress blinking depends on several parameters.
For these reasons, many efforts have been devoted to develop strategies based on the modification of internal structure of nanocrystals, in particular by choosing a suitable core/shell heterostructure.
These approaches mainly focus on the competition between radiative and non-radiative recombination channels.

Several reports have suggested that the nanocrystal shell engineering is a suitable strategy to control the recombination pathways, both the radiative and the Auger recombination rates, producing almost non-blinking nanocrystals [72] [73] [74]. Specifically, *giant* shell CdSe/CdS nanocrystals exhibit an almost complete suppression of blinking. Blinking is progressively reduced by increasing the shell thickness, and a complete absence of PL fluctuations is obtained with very thick shells (15-19 monolayers), together with a significant increase in photo-stability.

Blinking suppression in giant NCs can be assigned to two different factors, which are linked to the physical models of blinking introduced in section 2.1.1:

(1) **Suppression of Auger recombination** (type A blinking). As we said before, once a nanocrystal is in a charge-separated state, the emission is normally quenched because of an efficient Auger non radiative recombination rate γ_A. If the Auger recombination is no more efficient, grey states can become very efficient, i.e. the charged state QY can approach 1. Therefore, even when the nanocrystal is ionized it can continue to emit like when it is in a neutral state.

(2) **Reduction of electron tunneling** (type B blinking). A very thick shell can prevent the tunneling of hot electrons towards surface states, because the probability of this process is expected to decrease exponentially with the thickness of the tunneling barrier.

In ref [65] the authors demonstrate that type B blinking events are less and less frequent while increasing the shell thickness until they are completely eliminated for shells with 15 or more CdS monolayers. By contrast, type A blinking can still be observed even in the case of the extremely thick 19-monolayer shells. In a following work by the same group [81], the authors reported a

lifetime blinking even in nanocrystals where the emission is nearly Poissonian, showing that the thick shell does not prevent from photo-ionization, but it only makes the grey state as bright as the neutral state. On the contrary, the probability to be in a charged state seems to increase with the shell thickness, likely because of a less efficient relaxation of the trapped holes.

Auger effect suppression In order to understand how the Auger effect can be suppressed for certain core/shell configurations, such as giant NCs or graded alloy core/shell NCs, we must come back to the physical origin of the Auger effect.

One possible explanation relies on the electron wavefunction delocalization which takes place in quasi-II type heterostructures like CdSe/CdS: the Coulomb interactions are reduced by the spatial separation of electrons and holes. Indeed the volume scaling of the Auger rate is not determined by the physical dimension of the confinement potential but by the size of the exciton Bohr radius, which is roughly given by the distance between the electron and the hole wavefunctions.
On the other hand, a simple volume scaling would not explain the exceptional Auger rate reduction observed in [72] and [73]. For instance, a complete charge separation can be realized in type-II structures, but even in CdS/ZnSe nanocrystals (complete type-II heterostructures) the Auger recombination still occurs in hundreds of picoseconds.

In ref [82] the role of the core/shell interface in CdSe/CdS heterostructures is investigated and a breakdown of the volume scaling of the Auger rate is found already for a shell thickness of about 4 monolayers. Fluorescence-line-narrowing studies indicate that the suppression of the Auger rate correlates with the formation of an alloy layer of CdSeS at the core/shell interface. Therefore a suppression of the Auger effect would derive primarily from a *smoothing* of the confinement potential associated with the interfacial alloying process.

This would be coherent with the first proof of blinking suppression in CdZnSe/ZnSe nanocrystals [74]. In this pioneering work the authors suggested that the structure is a radially graded alloy of CdZnSe into ZnSe, which can soften the abrupt confinement potential of a typical core/shell nanocrystal.

2.2 Room temperature emission of non-classical light

2.2.1 On demand single photon sources

In the past few years, the deterministic generation of single photons on demand has become a field of huge interest for potential applications. The development of reliable sources of quantum light is a major challenge for the field of quantum information science, including quantum communication, computing and metrology. Several quantum information protocols are based on the properties of single photons and cannot be achieved with classical light. Such applications include single photon-based quantum cryptography that ensures inviolable exchange of information exploiting the fundamental laws of quantum mechanics.

Single photons from laser pulses Quantum cryptography has been the subject of very active research since the first proposals in the 1980s, such as the famous BB84 protocol. For example, quantum key distribution (QKD) allows ideally an unconditional secure key transmission. Presently, commercial QKD exploits attenuated coherent beams as single-photon sources.

In the context of quantum cryptography it is important to estimate the reliability of a single photon source. This is done by considering that a smart eavesdropper can get the information as soon as the number n of photons in each pulse is larger than one, provided that this pulse contains at least one photon. Therefore a low probability of emitting two or more photons is not a sufficient condition. A good parameter is the fractional information leakage f, i.e. the conditional probability that a pulse, containing some photons, contains more than one photon:

$$f = p(n > 1 \mid n > 0) = \frac{p(n > 1)}{p(n > 0)} = \frac{P_{2+}}{P_{1+}}$$

As we will see later, the probability $p(n)$ that a pulse contain n photons is also called the *photon statistics*. The simplest solution to generate single photons is to strongly attenuate a pulsed laser source. This kind of source, essential in quantum cryptography, is often used as a reference in order to study and compare the photon statistics of a quantum emitter, like a nanocrystal.

For a laser beam with an average intensity of μ photons, the photon statistics follows by definition a Poisson distribution. The probability to count n photons for each pulse is given by:

$$p(n, \mu) = \frac{\mu^n e^{-\mu}}{n!}$$

In this case the fractional information leakage is:

$$\begin{aligned} f &= p(n > 1 \mid n > 0, \mu) \\ &= \frac{p(\{n>1\} \cap \{n>0\}, \mu)}{p(n>0, \mu)} \\ &= \frac{1 - p(1,\mu) - p(0,\mu)}{1 - p(0,\mu)} \\ &= \frac{1-(1+\mu)e^{-\mu}}{1-e^{-\mu}} \overset{u \to 0}{\simeq} \frac{\mu}{2} \end{aligned}$$

This probability can be made arbitrary small by choosing μ close to 0, i.e by reducing the mean number of photons in each laser pulse.
This increases the probability $p(0, \mu) \simeq 1 - \mu$ that a pulse does not contain any photon at all, as illustrated in Fig. 2.7 a).
The maximum rate R of the photon flux is given by the product of the probability to have at least one photon in a pulse P_{1+} and the frequency of the laser pulses Γ:

$$R = P_{1+}\Gamma \approx \mu\Gamma$$

This kind of source is not deterministic (photons on demand) and its brightness is limited by the value of μ.

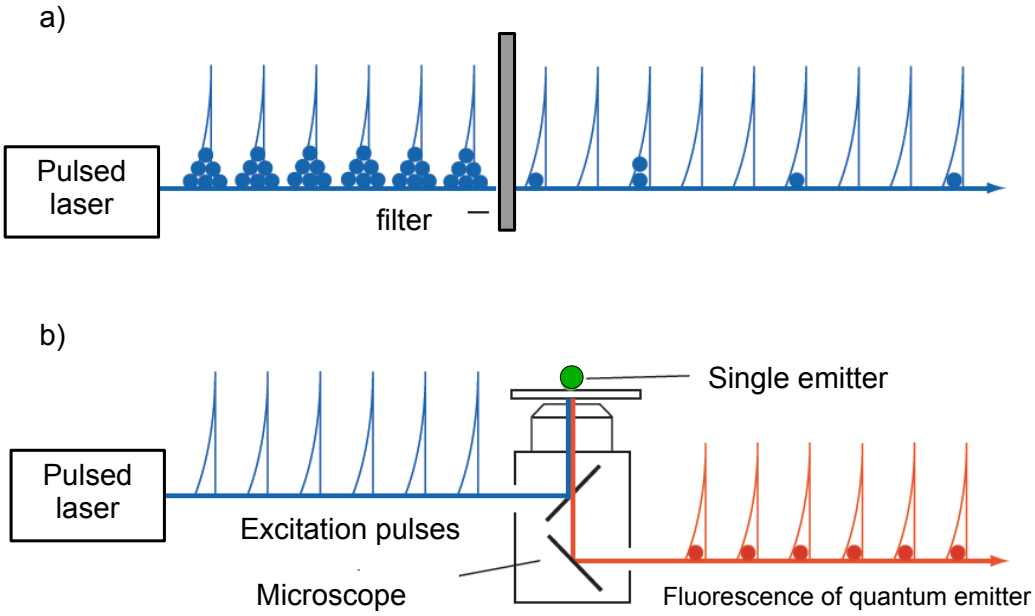

Figure 2.7: a) A single photon source based on faint laser pulses: in order to reduce the probability P_{2+} to emit two or more photons most of the pulses do not contain any photons at all. b) On demand single photon source based on a single quantum emitter, emitting single photons with unitary probability.

An ideal single photon source The best way to generate single photons on demand is to use a two-level system, as sketched in Fig. 2.7 b). This quantum emitter can be excited from its ground state by absorbing the energy of a properly tuned laser beam or by some other kinds of interactions (e.g. electron or phonon scattering). If the relaxation is purely radiative, only one photon can be emitted and detected for each excitation cycle. Indeed when a photon is detected, the two-level system falls into the ground state and it cannot emit one more photon until the excited state is recovered. In contrast to a Poisson source like an attenuated laser, two photons can never be emitted (and so detected) at the same time. The flux of photons is also said to be anti-bunched.

Of course there are some strict conditions which must be satisfied in order to build a real on demand single-photon source:

(1) The excitation time must be short enough compared to the radiative decay, in order to avoid more than one absorption-emission cycle during the excitation pulse duration.

(2) The probability of the excitation must be unitary: the beam pulse must be intense enough to bring the quantum emitter into its excited state. It is easier to reach this condition if

the quantum system has a high absorption cross section like dot-in-rods.

(3) The probability of the emission must be unitary, i.e the exciton Quantum Yield $QY_1 = 100\%$. This means that the transition must be purely radiative. Conditions (2) and (3) define the probability of single photon generation P_1 for the system.

(4) The collection efficiency of the light must be unitary. This can be obtained by modifying the normally isotropic emission diagram of the source, for instance by means of an interface or of an optical cavity. In our case the nanocrystals are deposited on a glass-air interface and 80% of the emitted photons can be collected by means of an oil immersion objective, as sketched in Fig. 2.7.

2.2.2 Auger effect and single photon emission in nanocrystals

Room temperature photon anti-bunching from CdSe/ZnS core/shell nanocrystals was first reported in 2000 [100] [101]. The possibility to use single colloidal nanocrystals as sources of nonclassical light at room temperature relies on the efficiency of Auger relaxation in strongly confined system.

When a multi-exciton state is generated inside the nanocrystal, their recombination can be radiative or non-radiative exactly like described for single excitons. A Quantum Yield QY_m can be defined for the decay of m electron-hole pairs to (m-1) electron-hole pairs, leading to the emission of one photon:

$$QY_m = \frac{\gamma_{R,m}}{\gamma_{R,m} + \gamma_{A,m} + \gamma_{NR,m}} \tag{2.2}$$

The radiative rate of m multi-excitons can be complicated because of the interplay of Coulomb effects, discrete electronic levels and their occupancy, wavefunction delocalization, etc... As a first approximation, which is valid at least for bi-exciton states, the radiative and non-radiative decay rates are expected to scale with the number of possible recombination pathways, and so with the number of charges. We will discuss the statistical scaling of radiative and non-radiative rates in details in the next chapter.

In small CdSe/ZnS nanocrystals (diameter less than 5nm) the Auger effect can quench the multi-exciton emission within a few picoseconds, since $\gamma_{A,m} \gg \gamma_{R,m}$ for $m > 1$.
This leads to negligible multi-exciton quantum yields QY_m for $m > 1$, and then to an efficient single photon emission [102].

Single exciton QY_1 was reported to be very high, up to 1 in solution measurements, which means that other non-radiative channels different from Auger are usually negligible, $\gamma_{NR} << \gamma_R$. This is why colloidal nanocrystals have been proposed as efficient triggered single photon source at room temperature [103].

However, their practical implementation have been for long time limited by the photoluminescence blinking which, as we described, is likely linked to the Auger effect too.

The quest for more stable and non-blinking nanocrystals, leading to a partial suppression of the Auger effect, has revealed a sort of intermediate regime where the Auger recombination

is in competition with the radiative recombination. For instance, in giant shell CdSe/CdS nanocrystals a nearly complete suppression of the overall Auger effect is obtained most of the time. This can be very useful for applications like lasers, or energy conversion, where having long lasting multi-excitonic states is convenient, but is detrimental for implementing a single photon source.

Quantum cascades of photons in colloidal nanocrystals Altough a not very efficient Auger effect can be detrimental for the performance of single nanocrystals as single photon source, the possibility to tune Auger rates may allow for generation of non-classical light states, like entangled photon pairs. This was already demonstrated at cryogenic temperature for quantum dots fabricated with vacuum deposition techniques [106].

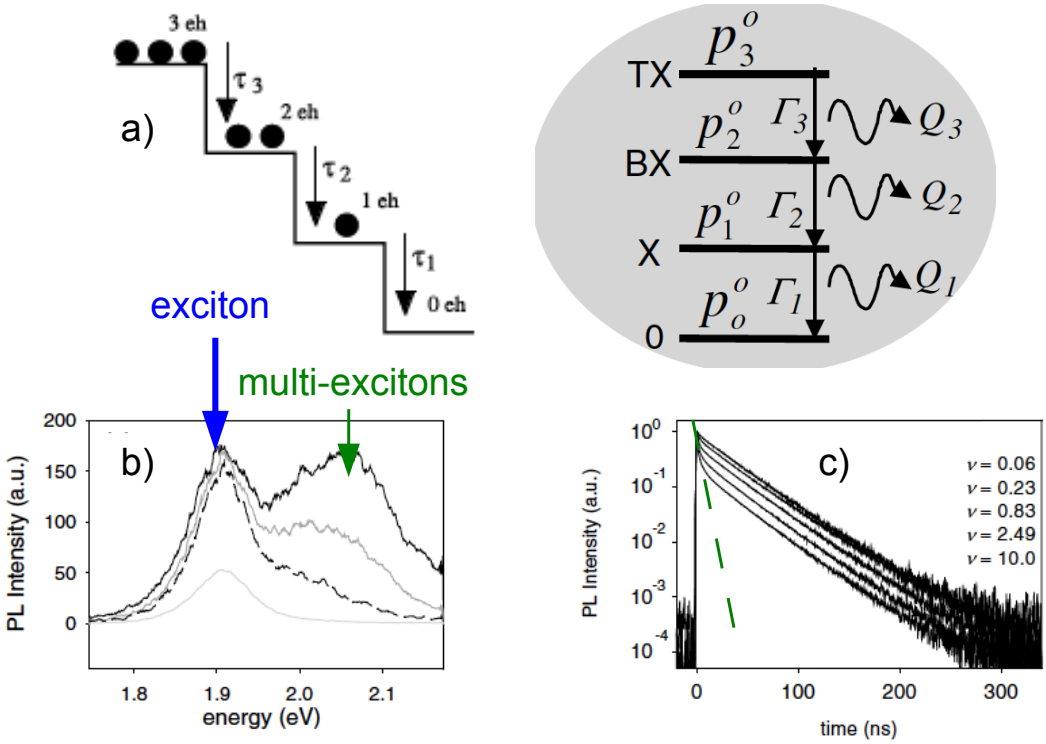

Figure 2.8: a) Sketch of an ordered quantum cascade of photons in CdSe/CdZnS nanocrystals. b) Transient ensemble spectra, showing a signature of multi-exciton radiative recombination. The high energy peak is associated with the fast decay of multi-excitons and it almost disappears after about 1 ns. c) Multi-photons in a lifetime measurment: at high excitation intensities a short lifetime component (green dashed line) emerges in ensemble PL, accounting for the multi-photons emission. All figures are taken from ref. [104].

The first experimental demonstration of an ordered multi-photon emission in colloidal nanocrys-

tals was obtained by Fisher [104], using CdSe/CdZnS core/shell heterostructure of large dimension (diameter about 5nm, PL at 655 nm).

In [104] the authors perform spectral and time resolved measurements both on ensemble and on single nanocrystals, at different excitation powers. The time resolved ensemble spectra in Fig. 2.8 b) clearly show the decay of multi-excitonic states at high energy and at short times (< 1 ns) after the pulsed laser excitation.
The emergence of a short time constant (lower than 1 ns, below the instrumental resolution) in otherwise mono-exponential fluorescence decays at high excitation intensities is another signature of the radiative recombination of multi-excitonic states, shown in Fig. 2.8 c). Decay constants of hundreds of ps were measured by means of a Streak Camera.
A definitive evidence for a multi-photon emission was provided by auto-correlation measurements on single nanocrystals by a Hanbury-Brown Twiss setup. A growth of the central peak as a function of the excitation power was observed. This behavior can be reproduced by a simple 4 levels system model, considering a ground state, a single exciton, a bi-exciton and a tri-exciton state. The intensity auto-correlation function is a powerful tool in order to study the photon statistics and to evaluate the quality of a single photon source. We will discuss widely about this subject in the next sections of this chapter.

Measurements of the auto-correlation function in [104] also revealed the mechanism for the multi-photon emission, that is an ordered quantum cascade of photons, with the tri-exciton decay preceeding the bi-exciton and the bi-exciton emission preceeding the single exciton.

2.2.3 Blinking suppression and single photon emission

The reduction of the PL blinking is often accompanied by a suppression of the Auger effect and thus by an increasing of the multi-excitonic Quantum Yields QY_m [75] [76] [77]. In some cases this can be useful: for example long lasting multi-excitons are necessary in nanocrystals-based lasers or solar cells or if we are interested in the emission of entangled photons pairs.

Of course an indiscriminate suppression of the Auger recombination is a drawback for the quality of the single photon emission. As a general rule, there is a positive correlation between blinking and multiexciton QY_m [83]: the more the photo-luminescence is stable, the more multi-photon emissions are likely to occur. This is reasonable, since the Auger effect is the common origin (at least in type A blinking models) of blinking and single photon emission.

However, some degrees of freedom allow to tailor at the same time blinking and single photon emission.
First of all, as we have already mentioned, the Auger effect can be different for electrons and holes. If we suppose that the photo-ionization leads mainly to negatively charged nanocrytals, the non-radiative processes in the grey state are dominated by the Auger recombination rate of negative trions γ_A^e. When many electron-hole pairs are generated they can recombine by transfering their energy both to electrons and to holes. If $\gamma_A^h \gg \gamma_A^e$ the multi-exciton decay is dominated by the Auger recombination of positive trions, i.e. by electron-hole pairs transfering their energy to a spectator hole. Therefore the blinking can be reduced because of a small γ_A^e, while at the same time multi-exciton radiative recombinations can be efficiently suppressed by a large γ_A^h.

For instance, in giant shell nanocrystals with completely suppressed blinking, the QY of the grey state is as high as the QY of the bright state. This implies that the Auger recombination rate in the charged state is suppressed, so that the lifetime of the grey state is exactly equal to its radiative lifetime. However a large dispersion of the bi-exciton QY_2, i.e. the probability to emit 2 photons, has been observed [75]. Therefore it is still possible, even if rare, to find single nanocrystals which are good single photon emitters. This implies that the Auger recombination of multi-excitons can still be efficient.
This apparent contradiction can be explained only by introducing 2 different Auger rates for the negative trion and the positive trion. The uniform non-blinking behavior is thus associated with an efficient suppression of the Auger energy transfer to electrons, $\gamma_A^e \ll \gamma_R$. On the other hand, in a non-blinking nanocrystal the Auger recombination of multi-excitons can still be efficient, because it is dominated by γ_A^h.

There are some other reasons which could explain why, in principle, a suppression of the blinking behavior can be attained without increasing too much the probability of multi-photon emission.
In type A blinking, the PL fluctuations are associated with a photo-ionization event followed by a relaxation process. The probability of these charging and de-charging processes depends strongly on the specific energy and spatial distribution of the trap states [85]. Even if Auger induced photo-ionization has a key role in the blinking models, ionization can also take place without the mediation of Auger effect. For example, a nanocrystal can be already in a charge-separated state after its synthesis. Therefore the nanocrystal internal structure, its surface and the core/shell interface can influence the ionization rate, and so the PL fluctuations, without requiring a suppression of the Auger rates.

Finally, type B blinking is not associated neither with the photo-ionization nor with the Auger effect, and so it should be possible to reduce it without interfering with the Auger efficiency. Indeed in CdSe/CdS with suppressed photo-luminescence fluctuations, type A blinking is prevalent. This is also why complete off states are quite rare in thick shell nanocrystals.

Different Auger rates for Positive and Negative Trion. The reasons for a difference in the Auger decay rates of negative and positive trions might relate to a much higher density of hole states in II-VI nanocrystals and/or to a higher degree of spatial confinement for holes than for electrons in CdSe/CdS quasi-type II heterostructures.

A pronounced difference between the Auger decay rates of negative and positive trions may explain previous observations of significant dot-to-dot variations in the biexciton PL quantum yields QY_2 among nominally identical nonblinking giant NCs [75]. Even when the Auger decay for the negative trion is suppressed, variations in the rate of the positive trion pathway may lead to a significant spread in the biexciton Auger time constants. Such variations can result from differences in the steepness of the core/shell confinement potential [82] as well as dot-to-dot variations in the core size. These are expected to affect more strongly a recombination channel involving the excitation of the core-localized hole, compared with a channel involving the excitation of the more delocalized electron.

Finally a difference in the Auger rates is coherent with the observation, stated in the previuos sections, that the Auger-assisted photo-ionization leads mainly to negatively charged nanocrystals. Hole trapping is more efficient because when a multi-exciton non-radiatively decays, its energy is transferred preferably to the hole, which thus can be more easily ejected from the NC core, as illustrated in Fig. 2.5.

2.3 Fluorescence Microscopy Techniques

Single nanocrystals can be directly observed with wide-field or confocal fluorescence microscopy techniques[109]. In both cases, samples are prepared by spin coating or drop casting on a glass microscope coverslip (BK7, 180 microm) a diluted solution of nanocrystals of proper concentration. Typical dilutions for the drop-casting are between 10^{-13} and 10^{-15} M, i.e. moles of nanoparticles per liter.

For both microscope configurations discussed below, a single objective is used to both focus the excitation light source and back-collect the nanocrystal fluorescence. A high numerical aperture (NA) infinity-corrected objective is employed to obtain high (diffraction-limited) spatial resolution. Lateral spatial resolution r for a given wavelength λ can be defined using the Rayleigh criterion as $r = 0.61\frac{\lambda}{NA}$.

Wide-field fluorescence microscopy. In wide-field configuration (Fig. 2.9) a large area of the sample is excited by focusing a non-collimated light source, either a UV lamp or a laser beam, through the objective.

The fluorescence from each nanocrystal within the focal volume is back-collected and spectrally isolated from residual scattered excitation light using a dichroic beam-splitter and further spectral filters. The fluorescence is imaged on a 2-dimensional detector, typically a charge coupled device (CCD) camera or directly on a photo-detector for ensemble measurements. The spatial resolution of the resulting wide-field fluorescence image is diffraction limited, as determined by the fluorescence wavelength and NA of the objective. A single frame image showing the fluorescence of many nanocrystals is reproduced in Fig. 2.9.

Confocal fluorescence microscopy. A confocal microscope configuration is advantageous for studies that aim to measure the faster time fluctuations in the fluorescence intensity (time-trace) or the carrier recombination dynamics of a single nanocrystal (lifetime).

The basic configuration of the confocal fluorescence microscope is illustrated in Fig. 2.9. A well-collimated excitation source enters the objective and is focused to a diffraction limited focal volume at the sample. The nanocrystals are highly dispersed, such that only a single nanocrystal is located within the excitation spot. In order to map the fluorescence from many nanocrystals over a large area on the substrate, the sample (or excitation spot in our case) is scanned using a piezoelectric stage with small step sizes ($r \simeq 100nm$). The spatial resolution is defined by the diffraction-limited focal area.

For a single nanocrystal measurement, the stage is positioned such that a single nanocrystal

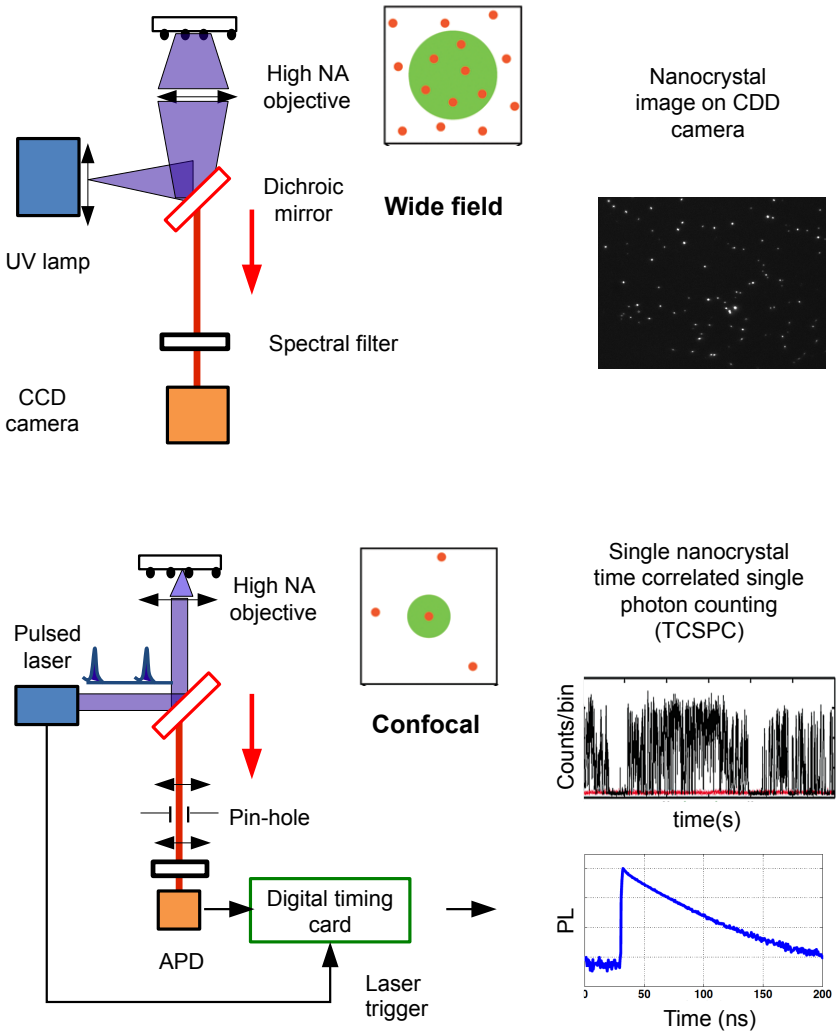

Figure 2.9: Fluorescence microscopy techniques. Upper panel: a wide-field configuration, where a large area of the sample is excited by a UV lamp and observed on a CCD camera. Lower panel: a confocal configuration, where one single nanocrystal is excited by a pulsed diode laser focused on the sample by means of a high NA objective. The photo-luminescence is collected by the same objective and then spectrally and spatially filtered. Finally the signal is sent to single photon detectors, an avalanche photodiode (APD) in this case. The time correlated single photon counting provided by a digital card allows for instance to measure the photo-luminescence lifetime or to perform blinking analysis on the time-trace.

is at the center of the focal spot. The nanocrystal fluorescence is back-collected and filtered spectrally. In a traditional confocal configuration, the fluorescence is focused tightly at a pinhole aperture (150 μm for a $100x$ magnification objective) to spatially separate and remove any out-of-focus light. The isolated fluorescence is then imaged by a single photodetector. Single photon

avalanche photo diodes (APDs, SPCM-AQR-13) are often used, as they have high detection efficiencies in the visible range and low dark count rates.

The APD signal is read by digital timer or counting card, as discussed below.

2.3.1 Time-Correlated Single Photon Counting

Carrier recombination lifetimes (from hundreds of ps to tens of ns) can be measured using a confocal microscope through time-correlated single photon counting (TCSPC) experiments. A thorough description of the fundamental principles of TCSPC is given in [110].

For these measurements, the excitation laser triggers a timer, which is stopped upon the detection of a fluorescence photon, by means of a time-to-amplitude converter (TAC). The delay times between photo-excitation and fluorescence emission are collected for each excitation cycle and a histogram of the fluorescence decay is built. The decay curve can be fitted by a single or a multi-exponential function to find the excited states lifetimes.

The pulsed laser excitation source must satisfy the following conditions: the pulse durations must be much shorter than the excited state lifetime and the period of the pulses must be longer than the lifetime. We use a diode laser PDL 800-B, emitting at 405 nm with repetition rate of 2.5 MHz (distance between two pulses: 400 ns) and pulse width of around 100 ps.

Specialized digital cards provide the timing electronics used for TCSPC (PicoHarp 300, by PicoQuant). On these cards, digital timers are triggered by the detection of an excitation pulse and by the detection of a fluorescent photon. An electrical synchronization pulse is usually provided by the laser control system.
Normally there are two different electronic systems, the first one registers the absolute arrival time with respect to the beginning of the experiment with a precision of some μs, the second one with respect to a trigger excitation pulse with temporal resolutions lower than $1ns$. The time resolution of this technique is limited by the instrument response function (IRF). With a digital TCSPC setup, this is determined by the timing accuracy of the detector, i.e. by the jitter of the electrical pulse generated after a photon detection. A sub-nanosecond resolution is typical: we measured $350ps$ by sending an attenuated laser pulse directly to the detectors.
By tagging each fluorescence photon with both its absolute arrival time and the delay time relative to excitation, both fluorescence blinking traces and fluorescence decays (lifetime) can be measured simultaneously for a single nanocrystal, as shown in Fig. 2.9.

We will use time-correlated single photon counting to measure exciton decay lifetime of single nanocrystals and for correlating photo-luminescence fluctuations with lifetime and multi-photon emission dynamics.

Let us consider some important issues and limitations in TCSPC techniques. A real detector has always a dead time, due to its operating mode. It means that it cannot measure two events if they come within a minimum delay. For example an avalanche photo-diode is blind until the avalanche of electrons produced by a single detection event is quenched and the breakdown potential is recovered. This implies that if two photons arrive within this dead time only one pulse can be detected.

Because of the detectors finite dead time, if the number of photons occurring in one excitation

cycle were > 1, the system would very often register the first photon but miss the following one or more. This would lead to an over-representation of early photons in the histogram, an effect called *pile-up*. This leads to distortions of the fluorescence decay, typically the fluorescence lifetime appearing shorter. In order to maintain single photon statistics, the average count rate at the detector should be at most 5-10 % of the excitation rate, e.g. with the diode laser PDL 800-B, pulsed at 2.5 MHz repetition rate, the average detector count rate should not exceed 250 KHz.

There is another natural limitation to single photon counting technique, due to the long dead time of single photon detectors. They cannot be used directly to characterize the photon statistics of a quantum state of light, which has a short lifetime (some ns in the case of fluorescence light). The probability to detect N photon counts for a quantum state with n photon $\mid n >$, which is collected and detected with a probability α, is a binomial distribution:

$$P(N,n) = \left(\begin{array}{c} n \\ N \end{array} \right) \alpha^N (1-\alpha)^{n-N}$$

Since the detector dead time is tipically 50 ns, which is much longer than the time distance between two photons coming from a nanocrystal, if two photons arrive within this dead time only one pulse can be detected. Therefore it is impossible to evaluate the photon statistics $p(n)$ with only one detector.

This limitation can be overcome by splitting the photon beam into two arms and using two independent detectors, in a configuration called **Hanbury-Brown Twiss setup**, sketched in Fig. 3.6. This configuration allows to improve the time resolution of the system, because the photons arrival time can be correlated between two detectors. The time resolution is thus given by the electrical jitter of the pulses generated by the photon counting and by the number of channels of the analog-digital converter of the card for data acquisition.

In this way it is possible to correlate each arrival time with the next one. We will see in the following that this is one of the best technique to study the photon statistics of a quantum state of light and to rely it to the quantum properties of the emitter.

2.4 Photon statistics of non-classical light

Since we are not dealing with ideal single photon sources, or 2 level systems, but with more complex semiconductor structures, there will always be a certain probability to emit more than one photon. Moreover the light can be emitted from different quantum levels with different efficiency, changing in time, as we described in the section devoted to the photo-luminescence blinking.

The general problem is to characterize the photon statistics of a low intensity beam and its evolution in time, i.e. the probability that a light pulse contain n photons $p(n,t)$. We will often speak about the properties of the photon flux, but we should always keep in mind that $p(n,t)$ does not come from intrinsic properties of photons as elementary particles, but it characterizes the statistical properties of the light source. Quantum light results from quantum transitions in matter. Quantum states of light emerge from photon counting statistics or time correlations

which cannot be explained by a wave model of light.

2.4.1 Intensity Auto-correlation Function

Definition and properties The photon statistics $p(n,t)$ of a beam of light can be fully characterized by measuring the auto-correlation function of the electromagnetic intensity $I(t)$ (also called second order correlation function), defined as:

$$g^{(2)}(t,\tau) = \frac{< I(t)I(t+\tau) >}{< I(t) >< I(t+\tau) >}$$

where the mean values are statistical, i.e. calculated on identical repetitions of the experiment. Normally the mean values are time independent (stationary) and then $< ... >$ can be replaced by a time average $<>_t$:

$$< I(t) >=< I(t+\tau) >=< I(t) >_t$$

For a classical field $I(t)$ is a continuous function of time and thus $g^{(2)}(\tau)$ must satisfy the Cauchy-Schwartz inequality, which implies the following constraint:

$$1 < g^{(2)}(\tau) < g^{(2)}(0)$$

In the case of quantum radiation, the intensity $I(t)$ can be thouhgt as a discrete flux of photons. $\frac{<I(t)I(t+\tau)>}{<I(t)>}$ is thus the conditional probability to detect a photon at $t+\tau$, given that one photon has been detected at time t:

$$g^{(2)}(\tau) = \frac{P(t,t+\tau)}{P(t)P(t+\tau)} = \frac{P(t+\tau \mid t)}{P(t+\tau)}$$

This probability is not a continuous function, then the value of $g^{(2)}(\tau)$ for a quantum state of light is not restricted by the Cauchy-Schwartz inequality: $g^{(2)}(0)$ can be lower than 1. The photons are treated like particles in the sense that only an entire number of them can be emitted and detected. This is the only 'quantum' assumption that we will use in the next paragraphs to develop our argument.
A fully quantum treatment [107] would require to quantize the intensity and take expectation values on the quantum state of light $|\phi >$. This kind of treatment leads to the following expression for the auto-correlation function at zero delay $\tau = 0$:

$$g^{(2)}(0) = \frac{< \phi|\hat{n}(\hat{n}-1)|\phi >}{< \phi|\hat{n}|\phi >^2}$$

where $\hat{n}$ is the photon number operator. Treating photons like particles means that we consider the photon number basis (Fock states) $|n >$. The expectation values taken in such a basis correspond to averages on the photon distribution $p(n)$, for instance $< \hat{n} >= \sum p(n)n$. Therefore we come to the following alternative expression for the auto-correlation function:

$$g^{(2)}(0) = \frac{< n(n-1) >}{< n >^2} \tag{2.3}$$

$g^{(2)}(\tau)$ measurements are normally performed by means of a Hanbury-Brown Twiss setup, in which the photon flux is split by a 50-50 beam splitter and sent onto 2 independent detectors. This allows to avoid the limitations due to the finite dead time of both the detectors and the electronic system, as we have already mentioned. It means that, using only one detector, two following photons couldn not be correlated if their delay τ is shorter than the dead time.

The value at zero delay $g^{(2)}(0)$ is a simple criterion to distinguish between classical and non-classical sources of light. According to the nature of the source of light, different situations are possible, illustrated in Fig. 3.6 :

if $g^{(2)}(0) > 1$ packets of photons are generated by the source and the flux is called super-poissonian. Examples of this situation, also called *photon bunching*, are the black body radiation and the stimulated emission, which allows the generation of photons in the same quantum state, thus leading to an excess of correlation.

If $g^{(2)}(0) = 1$ all detection events are independent and the source is called poissonian (e.g. a stabilized laser beam). Such a state of light is called a *coherent* state.

If $g^{(2)}(0) < 1$ the photon flux is *anti-bunched*, the beam is called sub-poissonian and the photons come from a non classical system. In the case of an ideal single photon source, for which two photons are never emitted at the same time $g^{(2)}(0) = 0$.

We will see now how a precise analysis of $g^{(2)}(0)$ allows for a complete characterization of the photon statistics $p(n,t)$ and, as a consequence, of the decay processes in a single nanocrystal.

Auto-correlation function under pulsed excitation In this section we will derive an equation relating $g^{(2)}(0)$ measurements to the photon statistic in the case of pulsed excitation, following the treatment proposed by Nair et al. [105]. We will try to point out the physical principles of this approach and we will refer to [105], especially to the supplementary informations, for further details about the calculation. All this treatment is completely based on statistics, with only one quantum assumption that photons are treated like particles: the quantum source can emit only entire numbers n of photons, each n state with a certain probability, i.e. a photon statistics $p(n)$.

Let us start by considering the histogram of coincidence counts as a function of the delay between 2 start and stop detection events, as it is measured by a Hanbury-Brown Twiss setup. When the quantum emitter is excited by a pulsed laser with an interval T between two pulses, the histogram is made of discrete peaks, like in Fig. 3.6, because n-photons pulses arrive at discrete time$= t + T$. The probability to detect N photon counts for a state with n photon, which is collected or detected with a probability α, is a binomial distribution:

$$P(N,n) = \left(\begin{array}{c} n \\ N \end{array} \right) \alpha^N (1-\alpha)^{n-N}$$

from which the probability to detect no counts $N = 0$ is $P(N = 0, n) = (1-\alpha)^n$.
Since we have two detectors, let N_α and N_β be random variables representing the number of

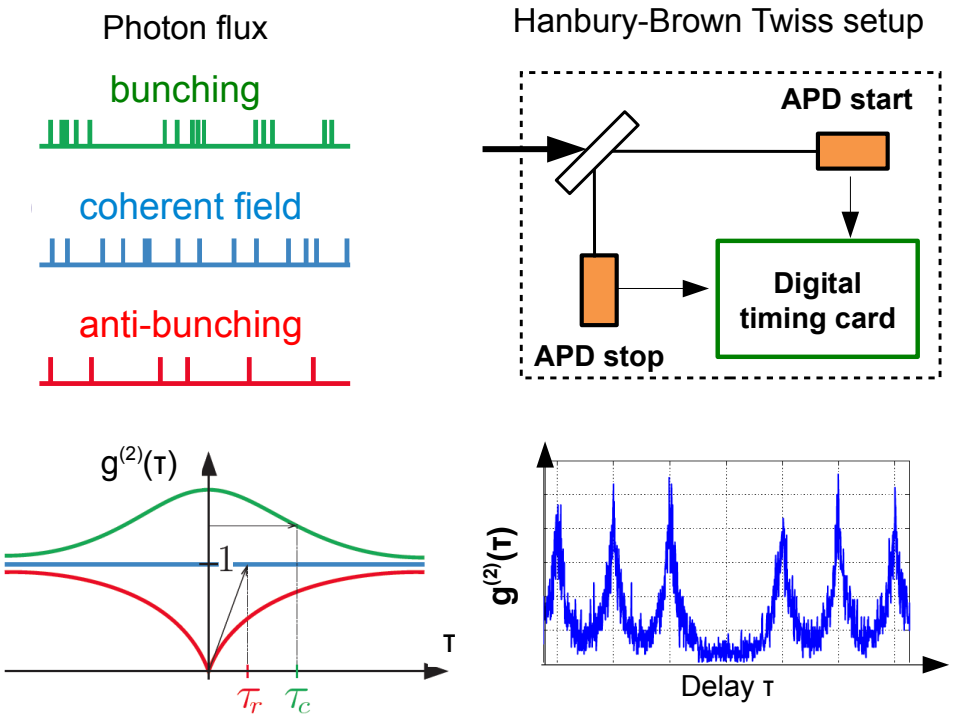

Figure 2.10: Left: bunching and anti-bunching of a photon flux and their corresponding $g^{(2)}(\tau)$ (τ_r and τ_c are time-scales of bunching and anti-bunching respectively). Right: Hanbury-Brown and Twiss setup for intensity auto-correlation function measurements: the delay τ is measured between a start count and a stop count by a digital timing card. In the lower part of the figure examples of $g^{(2)}(\tau)$ in the case of continuous (left) and pulsed excitation (right).

photon counts detected at the start and the stop and α and β the detection probabilities, taking into account the quantum efficiency of the detectors and all the losses of the optical system. One of the main interest of the auto-correlation function is that it is independent of the detection efficiency.

The central peak of the histogram (at delay $\tau = 0$) corresponds to the probability of start and stop occurring during the same n-photon pulse $P_n(center)$. It is the probability that at least one photon is detected at the start APD and at least one photon is detected at the stop APD:

$$\begin{aligned} P_n(center) &= P(N_\alpha \geq 1 \ \& \ N_\beta \geq 1) \\ &= 1 - P(N_\alpha = 0 \ or \ N_\beta = 0) \\ &= 1 - P(N_\alpha = 0) - P(N_\beta = 0) + P(N_\alpha = 0 \ \& \ N_\beta = 0) \\ &= 1 - (1-\alpha)^n - (1-\beta)^n + (1-\alpha-\beta)^n \end{aligned}$$

The probability to find a coincidence in the side peak, at delay= T, is the probability of start occurring at the n-photon pulse and the stop occurring at the next. It is the probability that at least one photon is detected at the start APD and no photon is detected at the stop

(this case is already considered in $P_n(center)$) multiplied by the probability that at least one photon is detected at the stop APD at the next pulse. Let P_β be this last probability:

$$P_\beta = \sum_{m=0}^{\infty} p(m) P(N_\beta \geq 1) = \sum_{m=0}^{\infty} p(m)[1-(1-\beta)^m]$$

The side peak is given by:

$$\begin{aligned} P_n(side) &= P(N_\alpha \geq 1 \ \& \ N_\beta = 0) P_\beta \\ &= [P(N_\beta = 0) - P(N_\alpha = 0 \ \& \ N_\beta = 0)] P_\beta \\ &= [(1-\beta)^n - (1-\alpha-\beta)^n] P_\beta \end{aligned}$$

By adding the contributions from all possible values of n weighted by their probabilities $p(n)$, we get the total probabilities of coincidence counts at the center peak $\sum p(n) P_n(center)$ and at the side peaks $\sum p(n) P_n(side)$ of the experimental histogram. We can evaluate the ratio of these two quantities, making the approximation of low detection efficiency, which is typical of most experiment, i.e. for α and $\beta \ll 1$:

$$\frac{\sum p(n) P_n(center)}{\sum p(n) P_n(side)} \approx \frac{\sum_{n=2}^{\infty} n(n-1) p(n)}{(\sum_{n=1}^{\infty} n p(n))^2} = \frac{< n(n-1) >}{< n >^2}$$

The last term is exactly the definition of $g^{(2)}(0)$ found in eq. 2.3.

We want to underline that no hypothesis was made on the temporal behavior of the n-photons pulse. Since any quantum emitter is characterized by a finite lifetime, the photon counts will be dispersed around the excitation pulse time t=0, T, 2T,... Nothing changes in the previous argument: it is sufficient to consider the total number of counts in the central peak and in the side peaks. This is made by taking the areas on the coincidence histogram:

$$g^{(2)}(0) = \frac{< n(n-1) >}{< n >^2} = \frac{Area(center)}{Area(side)} \tag{2.4}$$

As we said, this approach does not account for the specific shape of $g^{(2)}(\tau)$, which depends on the delay between two successive photons, which in turns is determined by the time evolution of the quantum source. For instance, by studying the specific temporal shape of $g^{(2)}(\tau)$ in [104], it was discovered that a multi-excitonic decay can produce an ordered cascade of n photons in a colloidal quantum dots, see Fig. 2.8.
For a complete derivation of the relation between the temporal behavior of the coincidence histogram and $g^{(2)}(\tau)$ we refer to [104] for a specific case or to [108] for a complete treatment.

Effect of Blinking on $g^{(2)}(0)$ The probability distribution $p(n)$ of the photons pulse can change over time, because of the intensity fluctuations or blinking.
This fact gives an effect of photon bunching on delay scale comparable to the time scale of the

fluctuations. This is typically much longer than the distance between laser pulses T, i.e. some ms against 400 ns or less.
$g^{(2)}(\tau)$ is a good tool also for studying PL fluctuations and we will discuss this later.

For the moment we will focus on $g^{(2)}(\tau)$ at short delays. In order to evaluate $g^{(2)}(0)$ from the experimental histogram it is necessary to normalize the coincidence counts at $\tau = 0$ with the counts of the side peak at $\tau = T$, according to eq. 2.4. Since the counts in the coincidence histogram at the center and at the side peaks are accumulated separately, the previously calculated quantities need to be time averaged:

$$\frac{\left\langle \sum_{n=2}^{\infty} n(n-1)p(n,t) \right\rangle_t}{\left\langle \left(\sum_{n=1}^{\infty} np(n,t) \right)^2 \right\rangle_t} = \frac{\langle\langle n(n-1)\rangle\rangle_t}{\langle\langle n\rangle^2\rangle_t}$$

Therefore $g^{(2)}(0)$ is given once again by the ratio between the central peak and the side peak areas:

$$g^{(2)}(0) = \frac{\langle\langle n(n-1)\rangle\rangle_t}{\langle\langle n\rangle^2\rangle_t} = \frac{Area(center)}{Area(side)}$$

2.4.2 Bi-exciton Quantum Yield from Photon Statistics

In the previous section we derived the experimental expression for $g^{(2)}(0)$ in the regime of photon counting, stating that it is measured by calculating the ratio between the number of coincidences detected at zero delay and the number detected at delay $\tau = T$.
Now we will see how this ratio can be linked to the internal properties of the nanocrystals, namely to the exciton Quantum Yield QY_1 and the bi-exciton Quantum Yield QY_2.

The probability $p(n)$ of a nanocrystal to emit n photons is given by two indepedent processes: the excitation, which can produce a certain number of electron-hole pairs N_{eh}, and the probability of the radiative recombination of this N_{eh} multi-exciton state. A nanocrystal absorbs a random number N of photons from one excitation pulse, leading to the creation of a random number N_{eh} of excitons in the band-edge levels. N_{eh} excitons are generated with a Poissonian probability which depends on the excitation intensity, i.e. on the mean number $< N_{eh} >$:

$$P(N_{eh}, \langle N_{eh}\rangle) = e^{-\langle N_{eh}\rangle} \frac{\langle N_{eh}\rangle^{N_{eh}}}{N_{eh}!}$$

This is true when the absorption takes place at high energy, much higher than the band-gap, so that the electron energy levels can be cosidered as a quasi-continuum. In order to simplify the notation we will call $P(N_{eh}, \langle N_{eh}\rangle)$ just $P_{N_{eh}}$.

Each step of the resulting recombination cascade can occur radiatively or non-radiatively. We can define a random variable q_m which takes the value 1 if the decay of the m-th exciton to (m-1) multi-excitonic state is radiative, and 0 otherwise. According to the definition of multi-exciton quantum yield, eq. 2.2, $< q_m >= QY_m$. We can thus calculate the random variable

corresponding to the number n of emitted photons, for the excitation of N_{eh} electron-hole pairs:

$$n = \sum_m q_m I_{N_{eh} \geq m}$$

where I is equal to 1 only if $N_{eh} \geq m$. By substituting this expression in the definition of $g^{(2)}(0)$ given in eq. 2.3 and by taking the expectation values, we obtain:

$$g^{(2)}(0) = \frac{\langle n(n-1) \rangle}{\langle n \rangle^2} = \frac{2 \sum_m P_{N_{eh} \geq m} \sum_{m' < m} \langle q_m q_{m'} \rangle}{(\sum_m P_{N_{eh} \geq m} \langle q_m \rangle)^2} \tag{2.5}$$

$P_{N_{eh} \geq m}$ is the probability that at least m photons are absorbed by the nanocrystal. This probability is a Poissonian of mean value $\langle N_{eh} \rangle$. Therefore eq. 2.5 provides the expected dependence of the auto-correlation function on the excitation intensity, which is proportional to $\langle N_{eh} \rangle$.

It can be calculated explicitly only if the quantum yield of all m multi-excitons $QY_m =< q_m >$ are known. In the next section we will see how QY_m can be estimated from the exciton QY_1 and the bi-exciton QY_2.

However, for most of the applications it is enough to consider the case where $< N_{eh} > \to 0$. In the limit of low excitation power eq. 2.5 can be simplified:

$$\lim_{<N_{eh}> \to 0} g^{(2)}(0) = \lim_{<N_{eh}> \to 0} \frac{2 P_{N_{eh} \geq 2} < q_2 q_1 >}{{P_{N_{eh} \geq 1}}^2 < q_1 >^2} = \frac{< q_2 q_1 >}{< q_1 >^2}$$

assuming that exciton and bi-exciton emissions are independent this becomes:

$$g^{(2)}(0) \approx \frac{< q_2 >}{< q_1 >} = \frac{QY_2}{QY_1}$$

If the emission changes in time (blinking or flickering) because of fluctuations of the non-radiative rate, due for example to charging and de-charging processes, time averages must be taken on numerator and denominator separately, as described before, because the counts in the center and lateral peaks are accumulated separately:

$$g^{(2)}(0) \approx \frac{< QY_2 >_t}{< QY_1 >_t} \tag{2.6}$$

Single nanocrystals as efficient single photon sources Eq. 2.5 shows that the auto-correlation function, can be written as a ratio of probabilities.

The product of the excitation probabilities $P_{N_{eh}}$ and of the conditional emission probabilities like $< q_m q_{m'} > \approx QY_m QY_{m'}$ corresponds to a joint probability that the emitted pulse contains a certain number of photons. This is exactly the photon statistics $p(n)$ which is required to calculate the expectation values of n and $n(n-1)$.

Let us consider some important cases. QY_1 is the conditional probability to emit one and only one photon, provided that at least one electron-hole pair is generated, $N_{eh} \geq 1$.

The probability to emit only one photon $P_1 = p(n = 1)$ is then:

$$P_1(< N_{eh} >) = QY_1 P_{N_{eh} \geq 1} = QY_1 (1 - e^{-<N_{eh}>}) \tag{2.7}$$

We will come back to this important expression in the next chapter.
In the same way QY_2 is the probability to emit a photon, knowing that the second one will be emitted for sure and that at least two excitons are present $N_{eh} \geq 2$. If the bi-exciton recombination and the following exciton recombination are independent the probability to emit two photons, will be the product QY_1QY_2, provided that $N_{eh} \geq 2$.

By using a similar argument for the evaluation of $< n(n-1) > / < n >^2$ as in eq. 2.4, it is possible to demonstrate [115] [105] that $g^{(2)}(0)$ is equal to:

$$g^{(2)}(0) = 2\frac{P_{2+}}{P_{1+}^2}$$

where $P_{2+} = \sum_{n\geq 2} p(n)$ is the probability to emit two or more photons and $P_{1+} = \sum_{n\geq 1} p(n)$ the probability to emit one or more photons. This is linked to the fractional information leakage defined before by the simple relation:

$$f = P_{1+}\frac{g^{(2)}(0)}{2} \simeq P_1\frac{g^{(2)}(0)}{2}$$

If $g^{(2)}(0) \approx 0$ then $P_{1+} \approx P_1$. Assuming the excitation $\langle N_{eh} \rangle \gg 1$ in eq. 2.7, we have $P_1 \approx QY_1$.

A $g^{(2)}(0)$ measurement thus allows a direct comparison with a single photon source based on faint laser pulses.
The photon rate R of a single photon source based on a single nanocrystal is:

$$R = P_{1+}\Gamma \approx QY_1\Gamma$$

where Γ is the frequency of the laser pulses. Its information leakage is:

$$f \approx QY_1\frac{g^{(2)}(0)}{2}$$

If $QY_1 \approx 1$ the source is nearly on demand, while f can be as low as $g^{(2)}(0)$, which is proportional to QY_2, according to eq. 2.6.

These results can be compared with a source based on an attenuated laser with a mean number μ of photons in each pulse. As we have already discussed, this kind of source is characterized by $R \simeq \mu\Gamma$ and $f \simeq \mu/2$.
If we assume the same laser frequency Γ, in order to produce the same photon rate R of the single nanocrystal, the number of photons in each pulse should be:

$$\mu \approx QY_1$$

The corresponding fractional information leakage would be:

$$f \approx \frac{\mu}{2} = \frac{QY_1}{2}$$

A single source based on a nanocrystal has thus an information leakage $g^{(2)}(0)$ times lower than a source based on laser pulses characterized by the same photon rate R.

2.4.3 PL as a function of the excitation intensity

In the previous sections we described how the normalized autocorrelation function at zero delay $\tau = 0$, $g^{(2)}(0)$ is a direct measure of the single photon source quality. It has been demonstrated that $g^{(2)}(0)$, measured at low excitation power, corresponds to the ratio between the probability of a two photons emission QY_2 and the probability of a single photon emission QY_1 [105].

Another method to assess the photon statistics of nanocrystals is to measure their PL as a function of the excitation power, i.e. of the mean number of excitons $\langle N_{eh} \rangle$ generated inside a nanocrystal by the absorption of the energy of a laser pulse [75]. This can be done both on single nanoparticles and on ensembles of nanocrystals.

When a laser pulse is absorbed by a NC, it creates N_{eh} electron-hole pairs with a Poissonian distribution $P(N_{eh}, \langle N_{eh} \rangle)$, with a mean number $\langle N_{eh} \rangle$ which is proportional to the excitation power.

Any m-multiexciton state decays to the $(m-1)$ state via an electron-hole recombination, which can be radiative or non radiative, with a probability QY_m to emit a photon. This process is repeated until all the electron-hole pairs have recombined.

In this model of a quantum cascade of multi-photons [104], the normalized PL intensity N_{PL} emitted by a nanocrystal is given by the following general expression [75]:

$$N_{PL}\left(\langle N_{eh} \rangle\right) = \sum_{N_{eh}=1}^{\infty} P(N_{eh}, \langle N_{eh} \rangle) \sum_{m=1}^{N_{eh}} QY_m \tag{2.8}$$

This is the number of photons emitted by a single nanocrystal for a single excitation pulse generating $\langle N_{eh} \rangle$ excitons.

QY_m is the probability of a m-exciton radiative recombination, as defined in eq. 2.2:

$$QY_m = \frac{\gamma_{R,m}}{\gamma_{R,m} + \gamma_{A,m} + \gamma_{NR,m}}$$

where γ_R is the radiative recombination rate, γ_A is the Auger recombination rate, responsible for single photon emission, and γ_{NR} takes into account other non-radiative decay channels different from Auger, like the energy transfer to phonons or to surface defects.

Using a statistical scaling with the number of charges for radiative and non-radiative decay rates of m excitons, as described in section 2.1.3, QY_m can be written in terms of single exciton and bi-exciton QYs:

$$QY_m = \frac{1}{1 + (m-1)A_2 + A_1/m}$$

where

$$A_1 = (\gamma_{NR,1} + \gamma_{A,1})/\gamma_{R,1}$$

and

$$A_2 = (\gamma_{NR,2} + \gamma_{A,2})/\gamma_{R,2}$$

Let us consider first of all the case of a perfect single photon emitter. In this case a saturation of $N_{PL}(\langle N_{eh} \rangle)$ is expected because an ideal single photon source can never emit more than one photon even if many electron-hole pairs $\langle N_{eh} \rangle$ are excited.

When all multi-excitonic Quantum Yields are suppressed by efficient Auger recombination, i.e. $\gamma_A \gg \gamma_R$, $QY_m \simeq 0$ for $m > 1$ and the probability of emitting more than one photon per excitation pulse is negligible, so $g^{(2)}(0) \simeq 0$. Then eq. 2.8 reduces to:

$$N_{PL}(\langle N_{eh}\rangle) = QY_1 \left(1 - e^{-\langle N_{eh}\rangle}\right)$$

This is exactly what we found in eq. 2.7, i.e. the probability P_1 to emit one photon per each excitation pulse, provided that $\langle N_{eh}\rangle$ excitons are created.
Experimentally it is useful to express this equation as a function of the exciting laser power P. P is proportional to $\langle N_{eh}\rangle$:

$$< N_{eh} >= P/P_{sat}$$

The *saturation power* P_{sat} is the power that corresponds to $\langle N_{eh}\rangle = 1$. Experimentally only a fraction of the photons emitted by a single nanocrystal can be collected and detected.
The photo-luminescence signal $I_{PL}(P)$ is a rate of photon counts measured by a single photon detector when the nanocrystal is excited by a laser pulse with a rate Γ. $I_{PL}(P)$ is just proportional to $N_{PL}(P)$:

$$I_{PL}(P) = I_{sat} \left(1 - e^{-\frac{P}{P_{sat}}}\right) \tag{2.9}$$

where I_{sat} is the product of QY_1, Γ and of the collection and the detection efficiency of the optical system. We will discuss this in details in the next chapter.
By fitting the PL curve as a function of the excitation power is thus possible to convert the excitation intensity into a number of absorbed excitons $\langle N_{eh}\rangle$, without knowing anything about the absorption properties of nanocrystals.
It is important to point out that the PL signal of an ensemble of quantum emitters, each one obeying eq. 2.9, such a cluster of nanocrystals, would show the same power dependence as in eq. 2.9.

If no Auger effect is present, $QY_m = QY'$ is identical for any number m of excited electron-hole pairs, leading to light emission with a Poissonian statistics, and consequently to a $g^2(0)$ equal to 1. Such a 'classical' source of light gives rise to a PL which is proportional to the excitation power:

$$N_{PL}(\langle N_{eh}\rangle) = QY'\langle N_{eh}\rangle$$

The saturation of the PL as a function of the excitation power is thus a remarkable signature of single photon emission.

If multi-exciton QYs are not negligible, the complete expression of eq. 2.8 must be considered. In order to make this expression more readable we have performed some numerical simulations, illustrated in Fig. 2.11.
The result is that for low excitation (up to $\langle N_{eh}\rangle = 6$) and low bi-exciton QY_2 ($\lessapprox 0.2$), $N_{PL}(\langle N_{eh}\rangle)$ can be approximated by the sum of the exponential of eq. 2.9 and of a straight line, as shown in Fig. 2.11 (right).
In the left panel of Fig. 2.11 we show the calculated contribution to the PL of multi-excitonic

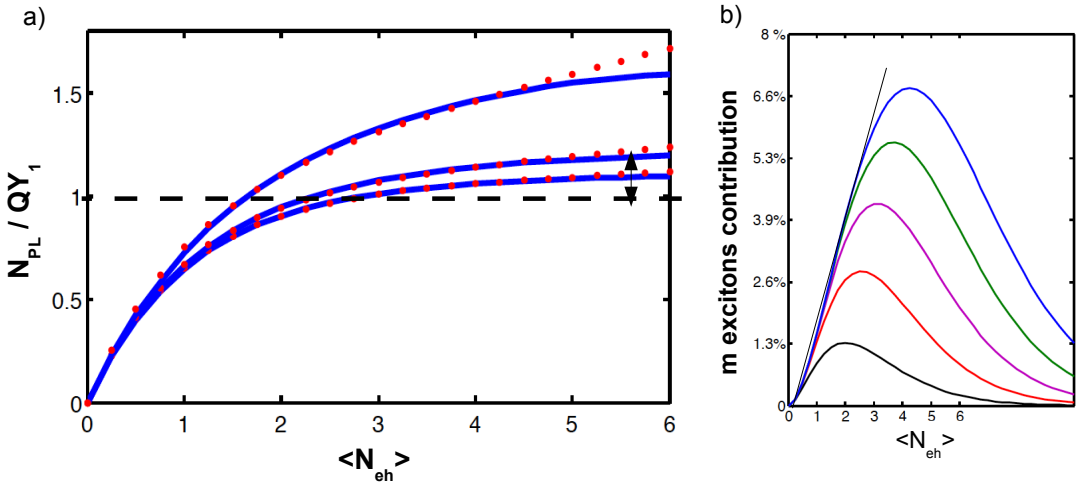

Figure 2.11: (a) N_{PL} normalized to the single photon QY_1 as a function of the mean number of excited electron-hole pairs as calculated from eq. 2.8 for different values of $g^{(2)}(0) = QY_2/QY_1$: 0.05, 0.1, 0.3 (frow bottom to top). Blue lines are calculated using the general expression 2.8, while red dots represents the simplified model of an exponential plus straight line of eq. 2.10 with a coefficient c=0.4. (b) Contribution to the PL of the first 6 multi-excitons (black=2X, red=2X+3X,...), expressed as a percentage of the saturation level (single photon emission), for $g^{(2)}(0) = 0.05$.

emission up to $m = 6$ and it is evident that this curve can be roughly approximated by a straight line. The saturation value of the exponential is the single photon QY_1, while the linear coefficient is proportional to the ratio QY_2/QY_1, which is exactly equal to the auto-correlation function $g^{(2)}(0)$ measured at low power:

$$N_{PL}\left(\langle N_{eh}\rangle\right) \simeq QY_1 \left((1 - e^{-\langle N_{eh}\rangle}) + c\frac{QY_2}{QY_1}\langle N_{eh}\rangle \right) \tag{2.10}$$

where $c \simeq 0.4$ according to our simulations.

Fig. 2.11 shows the evolution of the PL intensity for different values of $QY_2/QY_1 = g^{(2)}(0)$, according to the model described in eq. 2.8 (blue line) considering QY_m up to $m = 9$.

From these simulations it is evident that for values of $g^{(2)}(0)$ as low as 0.05 or 0.1, the contribution from the multi-excitonic emission only sligthly modifies the shape of the curve, with respect to the complete saturation of eq. 2.9, expected for a perfect single photon emitter.

2.5 Analysis of photo-luminescence fluctuations and Blinking

Strong emission fluctuations are now considered as a deep signature of single quantum emitter luminescence, even if they are basically ignored in ensemble measurements because they are not synchronized. The problem of characterizing the fluctuations of the PL intensity is a general issue of the optical study of single nano-objects, as molecules, quantum dots and nanocrystals.

In the first part of this chapter we focused on the physical origins of the fluctuations and on their theoretical explanation.

In this section, on the other hand, we review which experimental methods can be used in order to study the PL fluctuations, especially in the case of nanocrystals.

2.5.1 Bin and threshold analysis

Traditionally, the discrete blinking was accessed by the distributions of on and off times, calculated from the PL time-traces of single nanoparticles, measured by time correlated single photon counting (TCSPC). A PL time-trace is generated by summing the fluorescence counts of a TCSPC acquisition with a binning which can vary between fraction of ms and tens of ms. A sample blinking trace with 10 ms bins is shown in Fig. 2.12.

The kinetics of the switching processes that causes the nanocrystal intensity to alternate between high and low intensity states is probed through the distributions of on- and off-state dwell times or durations. A threshold is defined to separate the on- and off-state intensities. The threshold can be set to be halfway between the on- and off state intensity peaks in the photon distribution, if they can be separated. Alternatively, it can be set to a number of standard deviations above the average intensity of the off-state.

Upon setting a threshold, the blinking trace is divided into a sequence of on- and off-state events of given durations. This allows for the calculation of the percent time spent in the on/off state (on/off time fraction) and of the probability distributions of the on/off state durations, $P(t_{on}, t_{off}) = \frac{N(t_{on},t_{off})}{N_{tot}}$, where $N(t_{on}, t_{off})$ is the number of on/off state events with duration t_{on} or t_{off} and N_{tot} is the total number of on/off state events.

In most of the experiments, instead of the direct probability $P(t_{on}, t_{off})$, a cumulative probability is measured $P_{on/off}(\tau) = P_{on/off}(t_{on/off} > \tau)$, i.e. the probability to have on- or off-periods longer than a given value τ. Sample probability distributions are shown for on- and off state durations in Fig. 2.12.

Off-state durations are typically inverse power law distributed:

$$P_{off}(t_{off} > \tau) \propto \tau^{-\mu}$$

For standard CdSe/ZnS nanocrystals $\mu \approx 0.5$ for short τ [98], while for longer times $P_{off}(t_{off} > \tau)$ falls down faster due to the finite duration of the experiment.

Values between 0 and 1 (or 1 and 2, if a direct probability $P(t_{off})$ is considered) were found in many different experimental conditions: excitation power, temperature, experiment duration, excitation wavelength,....

On-state durations are also power law distributed (typically $0 < \mu < 1$) for short durations, but an exponential truncation is often observed for long on-state durations.

$$P_{on}(t_{on} > \tau) \propto \tau^{-\mu} e^{-\frac{t}{\tau_c}}$$

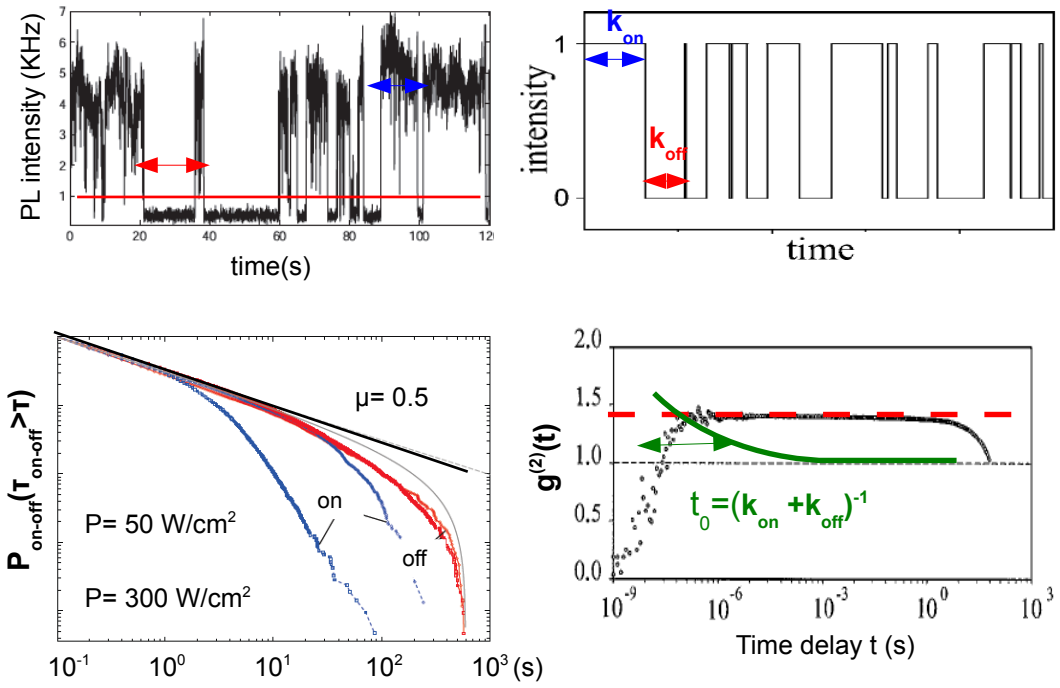

Figure 2.12: Left panel: An example of a bin and threshold technique for the analysis of discrete blinking between on and off states and the corresponding on-states (blue points) and off-states (red points) cumulative distributions at two different excitation powers. The plot is on a double logarithmic scale and the black straight line is a power law distribution with $\mu = 0.5$. Right panel: Random telegraphic model for the blinking (up) and intensity auto-correlation function of a single nanocrystal intensity time-trace. Heavy tail power law distribution of off-periods gives the nearly flat behavior found in ref. [97] (dashed red line). Finite on and off average times would lead to an exponential behavior (green line), with $g^{(2)}(\tau)$ going to 1 in a time $t_0 = 1/(k_{on} + k_{off})$, as discussed in section 2.5.2.

Let us discuss some issues of an analysis of blinking based on the bin and threshold method. A complete characterization of the artifacts introduced by a bin and threshold analysis is provided by [99].

The size of the time bin is selected in order to yield a good signal-to-noise ratio or it is imposed by the resolution of the detector. The choice of the time bin artificially limits the minimum on/off durations, and switching events occurring within one bin are averaged out. Overall, larger time bins lead to longer on/off state durations.

On-state distributions described by a truncated power law are heavily affected by the bin size. Variations of the threshold can also affect the values of μ and τ_c.

The variability of the measured distributions with the choice of the bin size and of the threshold makes also difficult to compare results originating from various sources. A minimal dependence

is observed only if the on- and off-state intensities are well separated.
If the fluctuations between the on and the off (or more likely the grey) states are too fast, no probability distribution can be built because there are not enough experimental points for most of the values $t_{on/off}$.

Even if there are some limitation to the bin and threshold method, the estimation of the μ parameter, especially for the off state durations, is still a good figure of merit to assess the blinking suppression in nanocrystals. From the statistical point of view the higher the parameter μ, the lower the probability to have long blinking periods. In particular:

If $\mu < 1$ all the momenta of the distribution $\frac{1}{\tau^\mu}$ diverge, and in particular its average value and its variance are not defined.

If $1 < \mu < 2$ the blinking statistics changes and the mean value converges.

If $\mu > 2$ the mean value and the variance converge and the law fulfills the central limit theorem.

2.5.2 Intensity auto-correlation function

The auto-correlation function $g^{(2)}(\tau)$ of the PL intensity $I(t)$ is less frequently used to characterize single nanocrystal blinking. However it becomes necessary when the fluctuations timescale is too short to perform a bin and threshold analysis, or when it is problematic to set a threshold between different emission levels [60].
The intensity auto-correlation function $g^{(2)}(\tau)$, already introduced before to access the photon statistics of a quantum emitter, can also be measured on longer time scales and it provides a direct measurement of the fluctuations dynamic.

Because of the PL intensity fluctuating during time, the emission of the nanocrystals is typically superPossonian, i.e. it shows photon bunching, like in the case of thermal light.

In order to measure $g^{(2)}(\tau)$, the intensity time-trace $I(t)$ measured by just one detector can be directly superposed with itself after applying a delay τ, according to the definition $g^{(2)}(t,\tau) = \frac{<I(t)I(t+\tau)>}{<I(t)><I(t+\tau)>}$

Let us consider a two-states model where a system jumps back and forth between on and off states with constant rates, k_{on} and k_{off}, respectively, as sketched in Fig. 2.12. In this model on and off states are characterized by finite and well defined average times $t_{on} = 1/k_{on}$ and $t_{off} = 1/k_{off}$. Such a model is often employed to represent the fluctuations of fluorescent systems and it successfully describes, for instance, the observed photon bunching in organic molecules [95].
In this case, the auto-correlation function is stationary and $g^{(2)}(\tau)$ varies as:

$$g^{(2)}(\tau) = 1 + \frac{1-p}{p} e^{-\frac{\tau}{t_0}} \tag{2.11}$$

where $p = \frac{k_{off}}{k_{on}+k_{off}}$ and $t_0 = \frac{1}{k_{on}+k_{off}}$

This exponential decay from the maximum value $\frac{1}{p}$ to 1 implies that, for t much longer than the characteristic time scale t_0, the auto-correlation function becomes constant (equal to 1). Efros and Rosen [96] developed a random telegraphic signal model for the fluorescence of colloidal nanocrystals which predicted this kind of behavior.

In the case of long tail power law distributions a much slower time dependence of the correlation function $g^{(2)}(\tau)$ is expected. Qualitatively, long on- or off-times yield to a nearly flat correlation, at least for short times. Such flat correlation functions have been observed experimentally [97].
In ref. [97] $g^{(2)}(\tau)$ was measured for capped CdSe/ZnS nanocrystals for a very long range of times, as illustrated in Fig. 2.12.

A complete theoretical derivation of the expected auto-correlation function for different kinds of fluctuations has been developed by Verberk [108]. According to this paper, on/off distributions and autocorrelation are entirely equivalent.

Chapter 3

Experimental study of CdSe/CdS dot-in-rods

Introduction My thesis project is consacrated to the study of the optical properties of colloidal dot-in-rods (DRs). The final goal is to develop a single photon source based on these nanocrystals with suitable characteristics for practical applications: suppression of blinking and multi-photon emission, photo-stability, and polarization of the emission are some key features. This objective requires a systematic characterization of many different kinds of dot-in-rods and a careful selection of the samples with the most interesting features. Most of them are, as we will see, the result of novel synthesis procedures, and thus without many references in literature.

When studying new materials there is always a first necessary step to do, i.e. developing the right experimental tools to extract maximal information from the system. This is why an important part of my work focused on the development of effective experimental techniques aiming, for example, at accessing the sample photo-stability from ensemble measurements or the quantum yield of single DRs. These results are of general validity, and they can be applied to the study of other nano-structures [124].

A complete room-temperature characterization of optical, and especially quantum optical, properties of single DRs is then provided: spectra, blinking and PL fluctuations, auto-correlation function, lifetime and their evolution with the excitation intensity, PL polarization have been measured for all samples. Some results of immediate practical interest towards the application of DRs as single photon sources have been attained: blinking suppression, associated with high single photon QY_1 and low auto-correlation functions $g^{(2)}(0)$ have been observed, for the first time, in thick shell DRs [111].

Other interesting results about the influence of the core dimension and the shell thickness and length on the lifetime and the Auger effect have been obtained as well. An analysis of the lifetimes confirmed that the photo-ionization is the main responsible for PL fluctuations in DRs. Single particle lifetime and $g^{(2)}(0)$ measurements as a function of the excitation intensity and a systematic study of the polarization properties contribute to shed some light on the electronic structure of DRs and its evolution with shape and dimensions. This contributes to a better understanding of the physics of quantum confinement in this kind of nano-structure. In particular, all these measurements reveal that the wavefunction engineering is a specific feature

of CdSe/CdS DRs. This can be associated with their intrinsic quasi-type II band alignment and with the possibility to tune supplementary degrees of freedom with respect to spherical nanoparticles.

The specificity of CdSe/CdS DRs relies on their electronic structure, designed as quasi type-II: although the core/shell band alignment would imply the localization of both carriers into the core, the very small offset of the conduction bands allows for the electron wavefunction to be spread also into the shell [39]. Because of that, the shell energy landscape strongly influences the electrons wavefunction $\phi_e(r)$ while preserving the holes confinement.
The results presented in this chapter are important for orienting future synthesis procedures toward further improvement of the performances of DRs as effective room temperature sources of polarized single photons.

3.1 Presentation of the samples

The DRs investigated in this work have been produced by a wet-chemical seeded-growth approach [16], a synthetic procedure, described in chapter 2, that allows a precise control of the heterostructure geometrical parameters [112].

In this section we present a selection of samples which have been analyzed in details, either because they have demonstrated remarkable optical properties or because they are useful to better understand some specific properties of DRs. Fig. 3.1 gives an in-scale sketch of the geometrical parameters, while the Table below provides a detailed characterization: core diameters are extracted by optical absorption and emission ensemble measurements [113], while the shell thickness and length are determined from T.E.M. images, as shown in Fig. 3.1 c) for DR42, by averaging on about 100 nanocrystals. Shell dimensions are less than 10% dispersed.

In particular, we will focus on the first group of DRs, characterized by the same CdSe core diameter $d \simeq 3.3nm$. The traditional synthesis protocol has been modified in order to thicken the shell size, resulting in a total DR thickness of $t \simeq 7nm$ against a thinner standard thickness of $t \simeq 4nm$ which is reported in many previous works about DRs [42] [43] [45]. Our approach, involving high growth temperatures ($350 - 380$ °C) and long reaction times (20-30 min), fosters the CdS shell to thicken in the volume section around the core and reasonably promotes the formation of Cd, S and Se alloyed layers at the core/shell interface [44]. We will show that it is possible to suppress blinking by keeping a good single photon emission by passing from thin shell DR42 to thicker shell DR22, while DR23 and DR26 are used to study the effect of shell length.

DR21 and DR24 are samples with bigger cores (4.2 and 4.5 nm respectively). In particular DR24 which have a very thick shell, will be taken as an example of how excessive suppression of Auger effect, despite enhancing the stability of the emission, also causes stronger multi-photon emission. DR76, on the contrary have a very small core (1.5-2 nm) and thin shell: blinking is still evident but they have very low $g^{(2)}(0)$.

a)

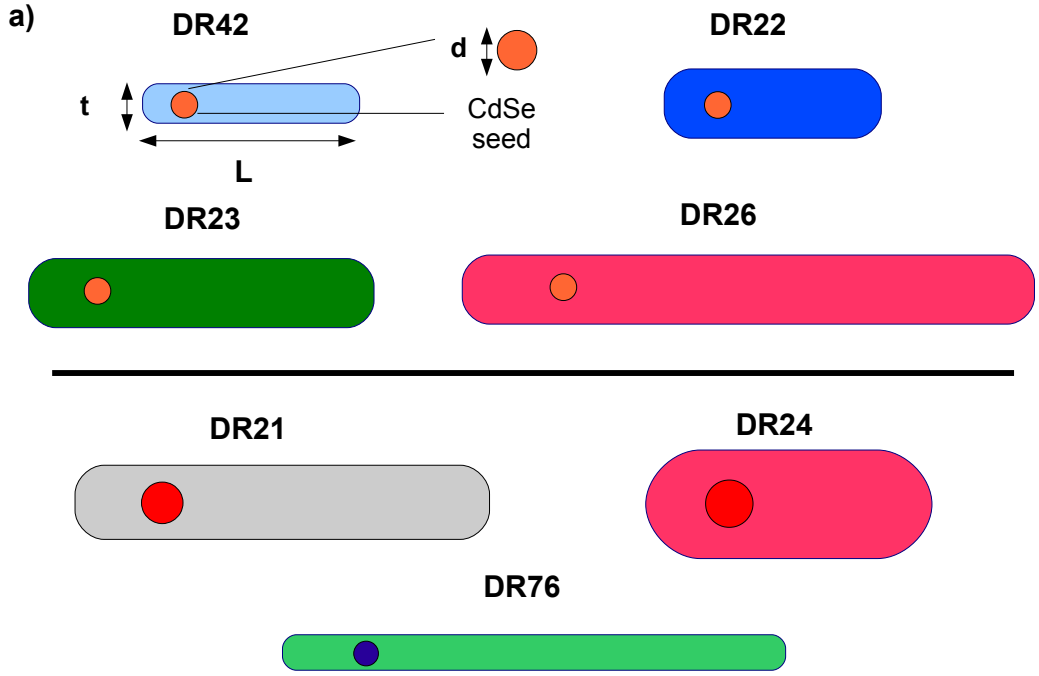

b)

DR name sample	Core Diameter d(nm)	Shell thickness t(nm)	Shell length L(nm)	Growth Temperature (°C)	Growth time (min)
DR42	3.3	4.0	22	350	8
DR22	3.3	7.0	22	350	20
DR23	3.3	7.0	35	380	20
DR26	3.3	7.0	58	350	40
DR21	4.2	7.5	42	380	20
DR24	4.6	11.0	29	360	8
DR76	1.5-2	3.6	51	350	8

c)

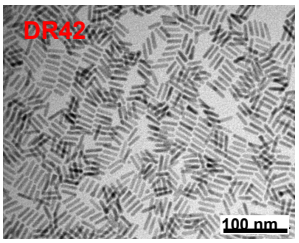

Figure 3.1: a) Schematic in-scale sketch of the DR samples optically characterized during this thesis. b) Table summarizing geometrical and synthesis parameters. c) An example of T.E.M. image for DR42, from which the shell size are estimated.

3.1.1 Photo-luminescence spectra

Absorption and PL emission spectra are measured in solution by means of a spectro-photometer. Fig. 3.2 shows an example of this kind of measurements for DR42 and its respective core seed sample.

In DR42 the PL spectrum is 25 nm red-shifted with respect to the CdSe seeds. This is an indicator of (electron) wavefunction delocalization following the CdS shell growth process. This red-shift has been observed in almost all the studied samples, as summarized in the table of

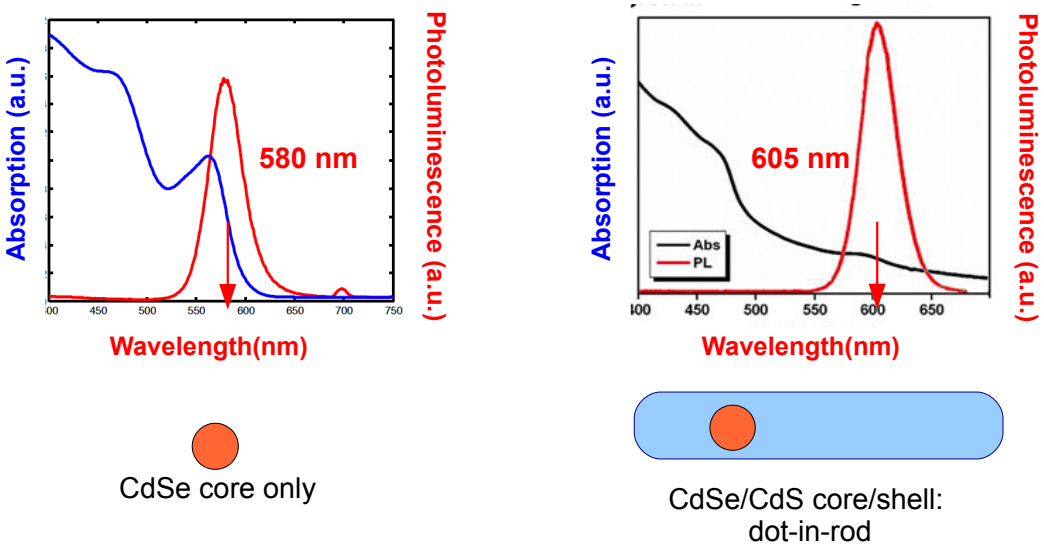

name DR sample	Core Diameter d(nm)	Core PL peak (nm)	Shell thickness t(nm)	Shell length L(nm)	DR PL peak (nm)	FWHM (nm)	Red-shift (nm)
DR42	3.3	580	4.0	22	605	33	25 (81 meV)
DR22	3.3	580	7.0	22	605	30	25 (81 meV)
DR23	3.3	580	7.0	35	600	27	20 (65 meV)
DR26	3.3	580	7.0	58	595	23	15 (49 meV)
DR21	4.2	604	7.5	42	600	30	- 4 (- 17 meV)
DR24	4.6	613	11.0	29	665	30	52 (145 meV)
DR76	1.5-2	~450-500	3.6	51	587	>50	>100 nm

Figure 3.2: Upper panel: An example of the absorption and emission spectra for a core-only sample and after the growth of rod-like shell. Lower panel: table summarizing the spectral characterization of all the samples

Fig. 3.2, indicating that in any case there is a certain degree of electron delocalization into the shell. Only DR21 show a negligible blue-shift. As we will see in the following section, DR21 are characterized by a low photo-stability, i.e. they are very sensitive to the chemical environment. The observed PL blue-shift could thus be associated to some degradation processes, like a photo-oxidation of the core.

The PL red-shift of the DRs with respect to the core-only systems confirms the model of CdSe/CdS core/size systems as quasi-type II heterostructures, described in chapter 1. A larger red-shift is an indicator of a prevalent type II electron delocalization, while a smaller red-shift indicates that the electron is more localized into the core.

The red-shift is maximal ($>$ 100 nm) for DR76, i.e. the sample with the smallest core size

($d = 1.5 - 2$ nm). This is coherent with the results obtained in [46] for thin shell DRs, where a transition to a type II regime was found for $d < 2.7$ nm. However, the spectral red-shift found for DR24, the sample with the largest core $d = 4.6$ nm, is still important, while it is minimal $(15 - 25)$ nm for the group of DRs with $d = 3.3$ nm. Moreover in samples with the same core and shell thickness but different lengths (DR22,DR23 and DR26), the red-shift decreases with the shell length. This fact will be confirmed by lifetime measurements.

With respect to previous studies about on DRs by Sitt [46], these results suggest that the wavefunction delocalization is not determined only by the core size, but also by the shell size, providing additional degrees of freedom for wavefunction engineering in DR with respect to spherical CdSe/CdS nanoparticles.

The Stokes shift, i.e. the energy difference between the emission peak and the first absorption peak, is about 40-50 meV (10-12 nm) for all the samples. This is exactly the same as in CdSe nanocrystal spectra, confirming that the emission of DRs comes from the core and not from the shell energy levels. On the other hand, the absorption edge at about 470 nm is dominated by the rod-like shell and the absorption from the core is much smaller. The absorption spectrum of the DR structure can be compared with the core-only absorption spectrum in Fig. 3.2.
This implies that the absorption from the core/shell nano-structure is much more efficient: the shell acts like a dipole antenna in harvesting the excitation light. All the absorption measurements here and in the following have been performed by using circularly polarized light, in order to assure a uniform excitation of the sample. The polarization properties of the absorption have not been studied yet and they represent a future perspective.

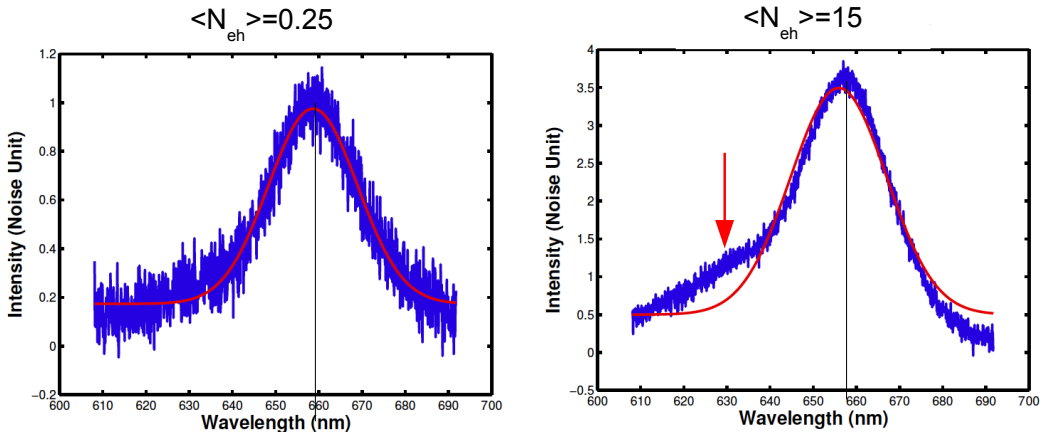

Figure 3.3: PL spectra of a single nanocrystal from sample DR24 at low power (left) and high excitation power (right). The central wavelength is about 660 nm in both cases.

PL spectra of single DRs The PL spectra of single DRs are measured by sending the PL of a single nanocrystal to a spectrometer Princeton SP2500 (f=500 mm) provided with a high sensitivity Peltier-cooled CCD camera.
Single DRs spectra are narrower than the ensemble spectra: the full-width half maximum from a Gaussian fit is $20nm$ instead of $30nm$. Single DRs spectra can be dispersed within $\pm 10nm$ the average value. This implies that the width of the ensemble spectra is only partially due to the inhomogeneous broadening, i.e. associated with size inhogeneities. Sources of the $20nm$ homogeneous broadening of single DRs PL spectra can be the scattering with thermal phonons or the Stark effect induced by fluctuations of surface charges (spectral diffusion).

DRs are excited both at low power i.e. for an average number of injected electron-hole pairs $\langle N_{eh} \rangle < 1$ and at high power ($\langle N_{eh} \rangle \gg 1$) and no difference is generally found. Only for thick shell DR24, at high power $\langle N_{eh} \rangle \simeq 15$ a new feature appears in the blue part of the spectrum, as shown in Fig. 3.3. This is a multi-excitonic contribution, likely the emission from the tri-exciton recombination, according to the literature [46]. The bi-exciton contribution is hidden because it should be much closer ($< 10nm$) to the central excitonic peak.

The conclusion is that multi-excitonic emission is efficiently suppressed in most of the DR studied samples, except in DR24. The auto-correlation function measurements will confirm and quantify this first simple observation.

3.2 Exciton and bi-exciton quantum yields

In this section I will describe a method to measure the emission Quantum Yield of single DRs. As we observed in chapter 2, the single exciton quantum yield QY_1 is an important parameter to build a deterministic single photon source: ideally QY_1 should be unitary in order to obtain one photon for each excitation event. At the same time the probability to emit more than one photon should be as low as possible, i.e. $QY_m \approx 0$ for $m > 1$.

Measuring the photo-luminescence QYs is not only important for the practical application of DRs as single photon sources, but it is also important to understand the interplay between radiative and non-radiative lifetimes. In fact, the decay lifetimes measured by time resolved single photon counting are only average rates:

$$\gamma_i = \gamma_R + \gamma_{NR} + \gamma_A$$

An independent measurement of QY is thus required to estimate the radiative and non-radiative rates, especially the Auger rates.

By measuring the PL signal as a function of the excitation $\langle N_{eh} \rangle$ and the intensity auto-correlation $g^{(2)}(0) = QY_2/QY_1$ at low power, it is possible to characterize each single DR in terms of its single exciton and bi-exciton quantum yields.

3.2.1 Measurements of single photon quantum yield

The PL quantum yield QY_1 of a sample of nanocrystals is usually measured on ensembles of nano-particles directly in their colloidal suspension [113]. This is made by first estimating the sample concentration and absorption coefficient, and then by comparing their emission with a reference sample, excited in the same conditions. QY_1 measurements in solution are usually carried on at very low excitation intensity in order to avoid multi-photon contributions.

This technique, even if useful for a qualitative comparison of two different samples like in [40] or [16], does not represent a reliable characterization of the emission efficiency of nanocrystals, when observed one by one in a quantum optics experiment.
First of all, the estimation of the concentration and of the absorption of the colloidal solution are usually subject to high experimental errors (between 10 and 50%). Moreover QY_1 measured in solution is simply an average value of the sample. Strong variations from one nanocrystal to another are possible and such a dispersion is not experimentally accessible.
Most importantly, the experimental conditions in a spectro-photometer for solution measurements and in a confocal microscope are very different: a highly concentrated solution of nanocrystals, well passivated by the abundance of ligands, is hardly comparable with the very low density deposed onto the microscope coverslip for single particle observations. It is well-known that the average QYs are much higher in solution than in air conditions, since photo-charging is probably less efficient in solution.

For all these reasons we developed a technique which allows to estimate the single photon QY_1 by a direct measure on single nanocrystals, by time-correlated single photon counting. It is based on a PL measure as a function of the excitation intensity on one side, and on auto-correlation function measurements on the other side. This method has many advantages:

(1) The measurement of QY is performed exactly in the same conditions in which other quantum optical properties, like single photon emission or blinking, are measured.

(2) It does not require any a priori information about the absorption of the sample, and about the excitation conditions. Many groups estimate the number of excited electron-hole pairs $\langle N_{eh} \rangle$ by means of an absorption cross section, which is either taken from ensemble measurements [113] or calculated from some theoretical model (i.e. assuming absorption scaling with the nanocrystal volume). This also requires to know precisely the shape and the energy of the laser beam on the sample. On the other hand, we can deduce $\langle N_{eh} \rangle$ independently, from a fitting procedure, which makes our system robust with respect to the excitation conditions.

(3) By monitoring the fluctuations of PL as a function of time, not only an average $\langle QY_1 \rangle_t$ but also a maximal QY_{max} can be extracted for each single DR. In an ensemble measurements the photo-luminescence is time and ensemble averaged.

(4) The contribution of the single photon and the multi-photon emission can be carefully separated, thanks to independent auto-correlation measurements

Methods The key point of our technique is that we can separate the contribution of single photon emission and multi-photon emission by using the theory developed in section 2.4.3 . This is made by independently measuring the PL intensity and the auto-correlation function for each single quantum emitter.

The emission of single nanocrystals is collected by an oil immersion objective with N.A.=1.4 and sent to APDs detector in a Hanbury-Brown Twiss configuration for auto-correlation measurements.
By time-correlated single photon counting it is possible to follow the PL time evolution $I_{PL}(t)$ with a time resolution of fractions of ms, depending on the detected rate. A typical PL time-trace from a single DR is shown in Fig. 3.4. This acquisition allows to estimate average $\langle I_{PL} \rangle_t$ (dashed red line in Fig. 3.4) and maximal I_{PL}^{max} (green dashed line) counts rates. The distribution of the photon counts, shown on the left of Fig. 3.4, shows that it is impossible to separate different intensity levels, because the fluctuations are too fast.
This kind of analysis can be repeated for different excitation powers P. In Fig. 3.6 the PL counts are measured for 10 single DRs at different powers and the values are averaged.

The measured curve of photon counts as a function of the laser excitation power is then fitted by a function proportional to the one derived in eq. 2.10:

$$I_{PL}(P) = k \cdot QY_1 \left((1 - e^{-P/P_{sat}}) + c \cdot g^{(2)}(0) \cdot P/P_{sat} \right) \tag{3.1}$$

k is the expected rate of photon counts on the detectors if $QY_1 = 1$, given the excitation laser frequency (2.5 MHz in our case) and the collection effiency of the confocal system. k can be estimated by measuring the collection efficiency of the objective, the losses of the optical system and the detection efficiency of the APDs, as sketched in Fig. 3.5.

We have performed simulations of the radiation diagram of a linear dipole, based on the classical paper of Lukosz [114]. These simulations show that the presence of an air/glass interface

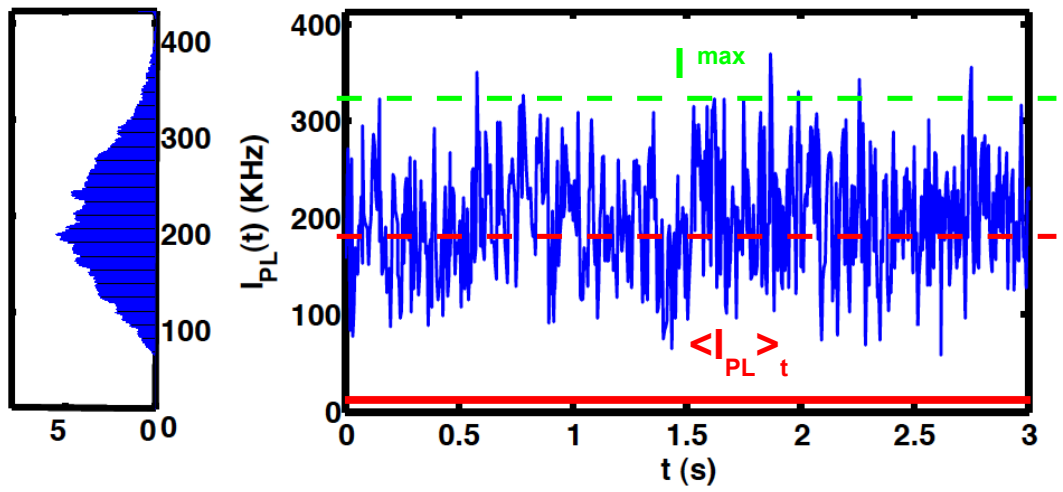

Figure 3.4: A typical PL time-trace for a single DR excited at power P above the saturation. Photon counts rates are measured on a time bin $\Delta t = 5$ ms. A maximal rate I_{PL}^{max} (dashed green line) and an average level $\langle I_{PL} \rangle_t$ (dashed red line) can be extracted, upon subtraction of the noise counts (solid red line). The distribution of the photon counts (on the left) shows that it is impossible to separate different intensity levels, because of too fast fluctuations.

redirects 86% of the radiated power into the higher refractive index, towards the oil objective. Further numerical simulations [115] have also demonstrated that this proportion is only slightly dependent ($\pm 5\%$) on the dipole orientation and nature (linear or degenerate dipole) and of its distance from the interface between 0 and 100 nm. With our NA=1.4 oil objective it is thus possible to collect up to 80% of the emitted photons. Fig. 3.5 summarizes the overall transmission of our system due to the losses of the optical elements, the transmission of the dichroic, the spectral filters and the pin-hole ($150\mu m$ for a microscope magnification of 100x) and the quantum efficiency of the APD detectors at 600 nm. The total collection efficiency is then found to be $15 \pm 2\%$. Considering a typical excitation pulses frequency of 2.5 MHz this leads to an expected photon rate $k = 375kHz$.

It is important to maximize the collection efficiency for any new measurement. The DRs are first illuminated by a UV lamp and selected by looking at the wide-field image on the CCD camera. By means of a piezo-electric control a single nanocrystal is moved in the center of the focussed laser spot, by maximizing the PL on the CCD. Once the PL signal is switched to the detection system, the position of the pin-hole is adjusted in order to maximize the photon counts on the avalanche photo-diodes.

Results Fig. 3.6 shows an example of PL measurements on two different samples of DRs, DR22 and DR24. DR22 are good single photon emitters, the average $g^{(2)}(0)$ is equal to 0.07 at low power ($\langle N_{eh} \rangle$ about 0.1-0.2), whereas for DR24 $g^{(2)}(0) = 0.3$, as exemplified in Fig. 3.6

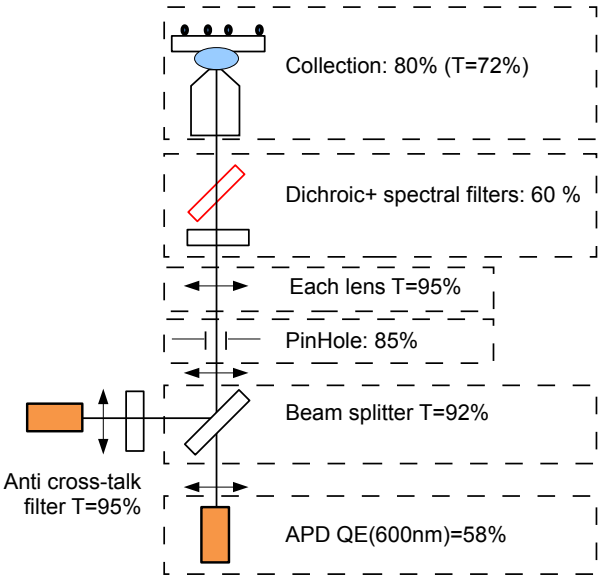

Figure 3.5: Schematics of the confocal microscope with estimated collection efficiency, optical losses and detection effiency.

(lower panel) for two single nanocrystals with similar lifetime. For DR22 the contribution from the multi-excitonic emission is only a small correction (about 10%) with respect to the expected complete saturation level (blue lines) for a perfect single photon emitter, while for DR24 this deviation is more pronounced.
The errors bars are much larger than the experimental errors, and they are due to the dispersion of the emission properties within the sample of 10 analyzed nanocrystals.

In the table of Fig. 3.6 we summarize the results of our measurements for all the kinds of DRs studied.
$\langle QY_1 \rangle_t$ is the value extracted from the fit of the time-averaged PL photon counts $\langle I_{PL} \rangle_t$ as a function of the power P, according to eq. 3.1. QY_{max} is the value associated with maximal photon counts rates I_{PL}^{max}, evaluated using a time bin of $t = 5ms$.

As described in chapter 2, in the model of a type A blinking, the PL fluctuations are associated with a charged, grey state. This is likely a negatively charged state, as widely discussed before. Therefore we will call $QY_1^{(-1)}$ the quantum yield of the grey state, where the index refers to the additional electron.
QY_{max} thus refers to the emission efficiency of the neutral, bright state:

$$QY_1^{(0)} \simeq QY_{max}$$

It is interesting that QY_{max} values $> 80\%$ are found for most of the studied samples. This measurement confirms that our DRs are synthesized with a small number of internal defects which would cause non-radiative recombinations, that is $\gamma_{NR} \ll \gamma_R$.

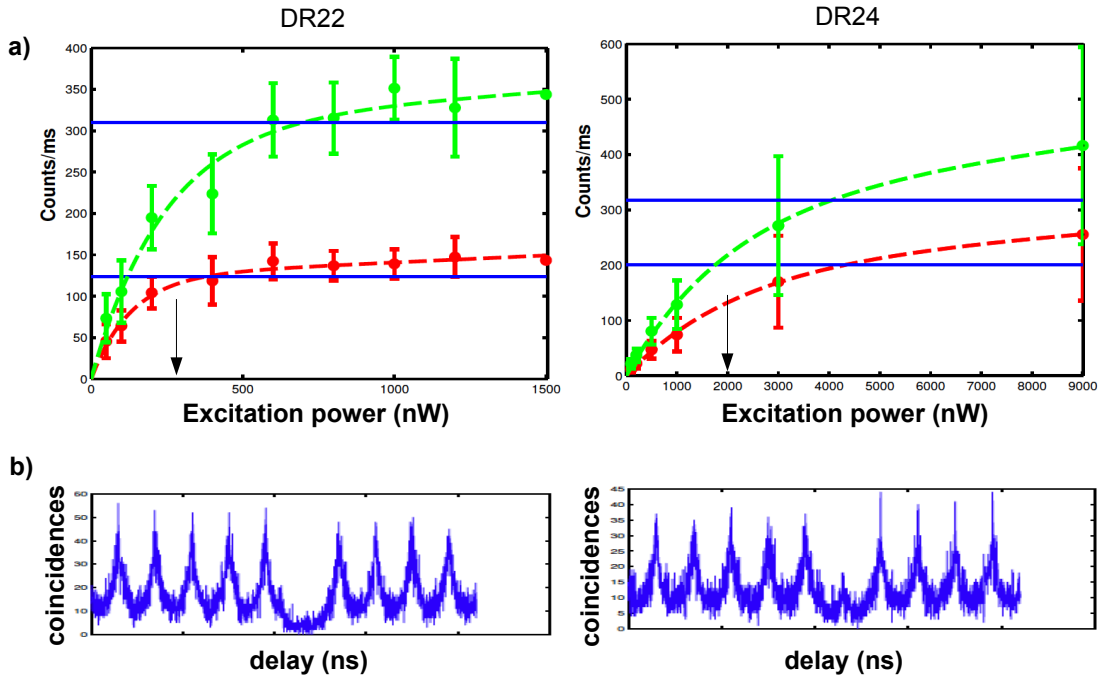

c)

DR sample name	<QY_1>$_t$	QY_{max}	$g^{(2)}(0)$ (<N_{eh}>=0.1-0.2)
DR42	0.1-0.27	0.3-0.75	0.14
DR22	0.33	0.83	0.07
DR23	0.33	0.79	0.1
DR26	0.33	0.92	0.13
DR21	0.39	0.84	0.1
DR24	0.54	0.85	0.3
DR76	0.22	0.64	0.06

Figure 3.6: (a) PL counts $I_{PL}(P)$ from single nanocrystals as a function of the power P for samples DR22 (left) and DR24 (right). Green points are maximal photon counts rates, while red points are time-averaged values. The arrows indicate the values P_{sat} and the blue lines the value $k \cdot QY_1$ found from the fit of eq. 3.1. $\langle QY_1 \rangle_t$ can be extracted from the red curve, QY_{max} from the green curve. (b) Auto-correlation function for two single DRs from sample DR22 (left) and DR24 (right), $g^{(2)}(0)$ is calculated as the ratio between the central peak area and the side peaks. (c) Table summarizing the quantum yields measured for all the DR samples.

$\langle QY_1 \rangle_t$, on the other hand, is due to the fluctuations between the bright state, the grey state and the off state. As it can be seen in Fig. 3.4, the time-scale of the PL fluctuations is too fast in order to separate the bright state and the grey state: this makes difficult to directly assess the quantum yield of the grey state $QY_1^{(-1)}$. However, a qualitative estimation can be provided by comparing QY_{max} and $\langle QY_1 \rangle_t$.
For instance, DR24 show the highest $\langle QY_1 \rangle_t = 0.54$: this implies that the efficiency of their grey state is higher than other samples. This can be associated to a better suppression of the Auger

effect, in particular of the negative trion decay rate γ_A^e, due to the shell thickness 11 nm.

If no grey states but only off states are present, like for thin shell DR42 and DR76, $\langle QY_1 \rangle_t$ is just an average between the bright and the off state, and indeed it is lower than in the other samples. Moreover, in this analysis only naocrystals with a signal-to-noise ratio > 3 are taken into account, and thus we do not consider nanocrystals which spend most of the time in an off state. These nanocrystals would make $\langle QY_1 \rangle_t$ even lower.
For thin shell DR42 a range of values of QY is given, corresponding to two different sets of measurements, one on a freshly open, well-conserved solution and the other one performed after some days. Both $\langle QY_1 \rangle_t$ and QY_{max} are much lower in the older sample.
As we will see in the next section, this sensitivity to the external environment is associated with a still evident blinking behavior and it can be improved by increasing the thickness of the CdS shell.

The table of Fig. 3.6 also reports the values of $g^{(2)}(0)$ found at low excitation power ($\langle N_{eh} \rangle = 0.1 - 0.2$) for all kinds of DRs studied in this thesis, from which the ratio $\langle QY_2 \rangle_t / \langle QY_1 \rangle_t$ can be extracted.
For most of the nanocrystals $g^{(2)}(0) < 0.15$ and thus their bi-exciton $\langle QY_2 \rangle_t < 0.05$. As we will see in section 3.6, $\langle QY_2 \rangle_t \approx QY_2$ is nearly constant, i.e. it does not depend on the state of charge.
The only exception are DR24 where $g^{(2)}(0) = 0.3$ and $\langle QY_2 \rangle_t \simeq 0.15$. This implies that the Auger effect of the positive trion γ_A^h, which is the main responsible for the suppression of the multi-excitonic emission, is not very efficient.
Moveover, $\langle QY_2 \rangle_t$ in DR24 is 3 times larger than in thinner samples like DR22 or DR21, while $\langle QY_1 \rangle_t$ is only 1.5 times larger. The two Auger rates γ_A^e and γ_A^h do not have the same behavior. This suggests that growing a too thick shell is detrimental for the performance of DRs as single photon sources.

Conclusions In this section we performed quantum yield measurements, by means of a method based on measurements of the PL emission from single DRs as a function of the excitation power. This kind of measurement is preliminar to any other because it allows to calibrate the excitation conditions. The laser power P is converted into a mean number of excitons $\langle N_{eh} \rangle = P/P_{sat}$, where P_{sat} is found from the fit of I_{PL}^{max} as a function of P.
High $QY_1^{(0)} \simeq QY_{max}$ are regulary measured for the bright state in air conditions, confirming the good structural quality of the samples.
The presence of a grey state in thick shell DRs increases the average quantum yield $\langle QY_1 \rangle_t$. A thicker shell also acts on the stability of the photo-luminescence, as it will be more clear in the next sections devoted to blinking and photo-stability.
$g^{(2)}(0) \approx 0.1$ is measured at low power for a selection of about 10 DRs from each sample, showing that most of the samples are potentially good single photon emitters, except for DR24 where $g^{(2)}(0) \simeq 0.3$.

3.3 Blinking suppression in CdSe/CdS dot-in-rods

In this section we will demonstrate how the photo-luminescence blinking can be suppressed in DRs by growing a thicker rod-like shell. We will focus on two samples with the same core size (d=3.3 nm) and shell length (L=22 nm) but different shell thickness t: DR42 (t=4 nm) and DR22 (t=7 nm). A substantial suppression of off-states durations and the appearance of relatively bright grey states ($0.2 < QY_1^{(-1)} < 0.5$) have been measured. This is, up to our knowledge, the first observation of grey states in dot-in-rod nanostructures; these results are detailed in a recent publication [111].

We also show that increasing the shell length does not improve blinking suppression, by presenting the results for DR23 (L=35nm) and DR26 (L=58nm). All measurements are performed in air conditions. Protecting the DRs with a polymeric film like PMMA would probably further improve the non-blinking performance.

3.3.1 Off and grey states

A blinking reduction with respect to traditional CdSe/ZnS nanocrystals has already been demonstrated in CdSe/CdS spherical nanostructures, and grey states, instead of off states, have been intensively observed in this kind of hetero-nanostructures [73] [89]. Most often the simultaneous presence of grey and off states have been reported.
A first advantage of having grey states is that they increase the time-averaged $\langle QY_1 \rangle_t$, because the grey states are well above the noise level, in opposition to the off states. However, one could observe that this does not solve the problem of creating a deterministic single photon source, because this would necessarily require $\langle QY_1 \rangle_t = 1$. Of course this is true, but the presence of grey states brings an important additional advantage.

The main reason why blinking is normally considered detrimental for practical applications is that the time duration of off periods is unpredictable, since it follows a long-tail power-law distribution, for which average and standard deviation cannot be defined: off periods as long as the duration of the experimental run appear with non negligible probabilities. Now, the presence of grey states is also generally accompanied by the emergence of a different distribution of on and off (and grey) times. Even if off states can be still present, they occur more rarely, and long off-periods are nearly suppressed. The switching from bright to grey states, and to off states, is usually very fast (of the order of ms): this allows to define a time-scale for the low intensity periods. As a consequence the nanocrystals are basically emitting most of the time, as illustrated in Fig. 3.7 for DR22.

The emergence of grey states, the simultaneous co-existence of grey and off-periods and the transition from a long-tailed distribution to a short-tailed, or even exponential time distribution, can all be understood by referring to the double nature of blinking, described in chapter 2.
Long off-periods can be explained in the scenario of type B blinking, for example by invoking a process of hot electrons trapping at the surface. Growing thicker shells would prevent this phenomenon, because the tunneling rate strongly depends on shell thickness, as described in [65] . Also the time duration of off-times can be modified by the shell geomtery.

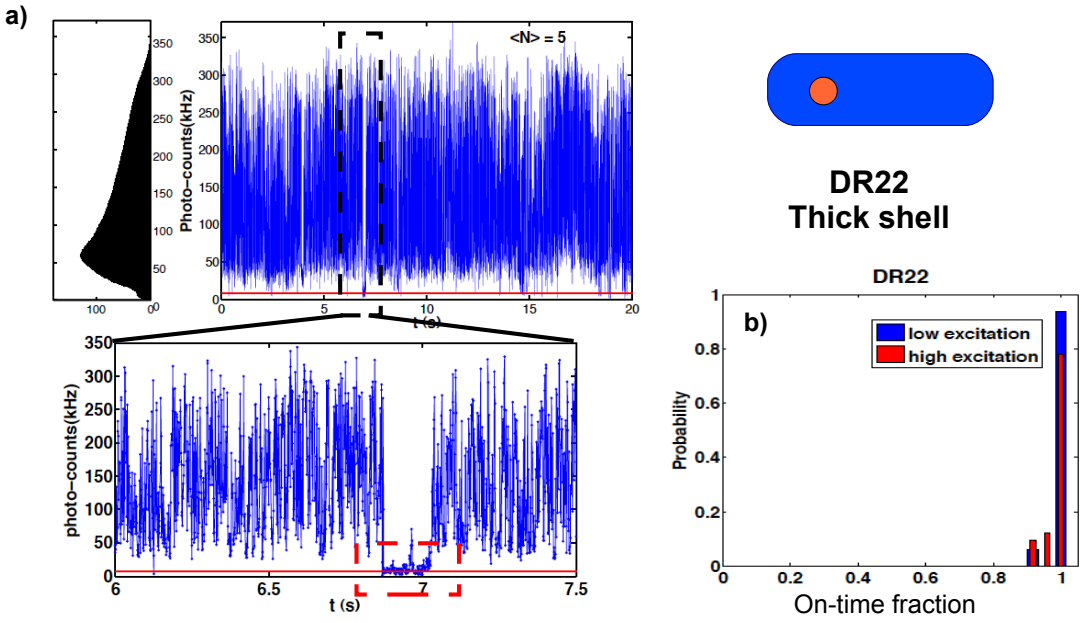

Figure 3.7: Blinking suppression in thick shell DRs, the example of DR22 (d=3.3nm,t=7nm, L=22nm) (a) Single nanocrystal PL time-trace showing the fast switching between bright and grey periods. The zoom shows that also completely off periods can be present (red dashed box), the red line is the noise level. (b) On-time fraction at low ($\langle N_{eh} \rangle < 1$) and high ($\langle N_{eh} \rangle > 1$) excitation, showing that off periods are very rare. The threshold for being in the on state is set two standard deviation above the noise level.

On the other hand, a type A blinking, associated with photo-ionization and charging, can explain the presence of grey states. The thickness of the shell cannot eliminate Auger-assisted photo-ionization. However, once the nanocrystal is in a charged state, it enters a grey state, instead of an off state, due to a reduction of the Auger effect, which makes the radiative and non-radiative recombinations rates comparable.
In this case the main physical mechanism is thought to be the hole trapping, which leaves the nanocrystal in a negative trion state. A different Auger rate for the electron γ_A^e and for the hole γ_A^h would explain why photo-ionization is still efficient ($\gamma_A^h \gg \gamma_R$), although in grey states the Auger rate can be quite low ($\gamma_A^e \approx \gamma_R$). This fact also justifies, as we will see in the following, why the suppression of the Auger effect acting on blinking can be attained while conserving reasonable single photon emission properties.
Concerning the time distribution of the grey states, it was already mentioned that a type A blinking [65] is characterized by an exponential cut-off in the on-time distrbution. In non blinking DRs a fast switching between bright and grey states is observed, characterized by a well-defined and short time-scale.

3.3.2 Blinking suppression in thick shell dots-in-rod

In order to characterize the blinking statistics, first of all we perform an analysis of the PL time-traces by using the bin and threshold method described in chapter 2. This kind of analysis focuses only on the off-state dynamics; the grey states, when they are present, are not considered here. PL time-traces $I_{PL}(t)$ are measured with a time binning $\Delta t = 1ms$ and a threshold for discriminating the off periods from the on states is set at 5 times the noise level.

Fig. 3.8 shows the results. For thin shell DR42 (t=4 nm) the cumulative distribution of the off-periods $P(t_{off} > \tau)$ follows a power law distribution with coefficient $\mu \simeq 1$. We remind that for $0 < \mu < 1$ no average and standard deviation can be defined, meaning that long off periods are likely to happen. In the right panel of Fig. 3.8, it is also reported the on-time distribution (black triangles), showing an exponential cut-off, similar to what observed in thin shell CdSe/CdS spherical nanocrystals.

For thicker shell (t=7 nm) samples DR22 (L=22 nm), DR23 (L=35 nm) and DR26 (L=58 nm), the slope of cumulative off-time distributions in the log-log plot is $2 < \mu < 4$, indicating that off-periods are much faster. The shortest DRs (DR22, black circles in Fig. 3.8) show the highest μ.

Therefore increasing the shell length does not improve the blinking suppression. On the contrary, too long DRs are slightly worse in terms of off time statistics. This can be explained by the increase of the surface-to-volume ratio with the shell length and with a higher probability to form internal defects and trap states in such long shell structures.

In thicker shell DRs grey periods are much more frequent than off periods, as illustrated in Fig. 3.7. The off-times analysis has been performed by choosing a threshold level of 5 times the noise value. This relatively high threshold is necessary to accumulate enough points to compile the cumulative distributions of Fig. 3.8, but it is probably too high to properly discriminate between off and grey states.

This is why we also use another method to evaluate the blinking dynamics, the *on-time fraction*, i.e. the ratio between the time spent in the on-state and the total measurement time (typically 60 s). Even if more qualitative than cumulative distributions, on-time fraction allows to lower the threshold for the off-states and fix it at two standard deviation above the average noise level. Fig. 3.7 shows the results for about 20 nanocrystals from sample DR22: their PL is above the noise threshold for more than 90% of the time, independently of the excitation power.

An on-time fraction analysis on thin shell DR42 reveals a very different behavior, illustrated in Fig. 3.9. Some nanocrystals spend a significant amount of time in an off state and on-time fractions become lower under high excitation ($\langle N_{eh} \rangle > 1$).

Moreover, the same measurement on a fresh sample and on a sample kept in air for some days show very different results, while thick shell are normally stable in air for weeks after the deposition. Other conservation parameters, like the concentration of the colloidal stock solution, may play a role. This is why all the samples are conserved at high concentration (tipically $10^{-6} - 10^{-7}$ M) and diluted just before the drop casting.

The results of Fig. 3.8 and Fig. 3.9 show that thin shell DR42 are much more sensitive to environmental conditions than thick shell DRs. This is compatible with the models of blinking previously discussed. DR42 are dominated by a type B blinking, characterized by long off periods

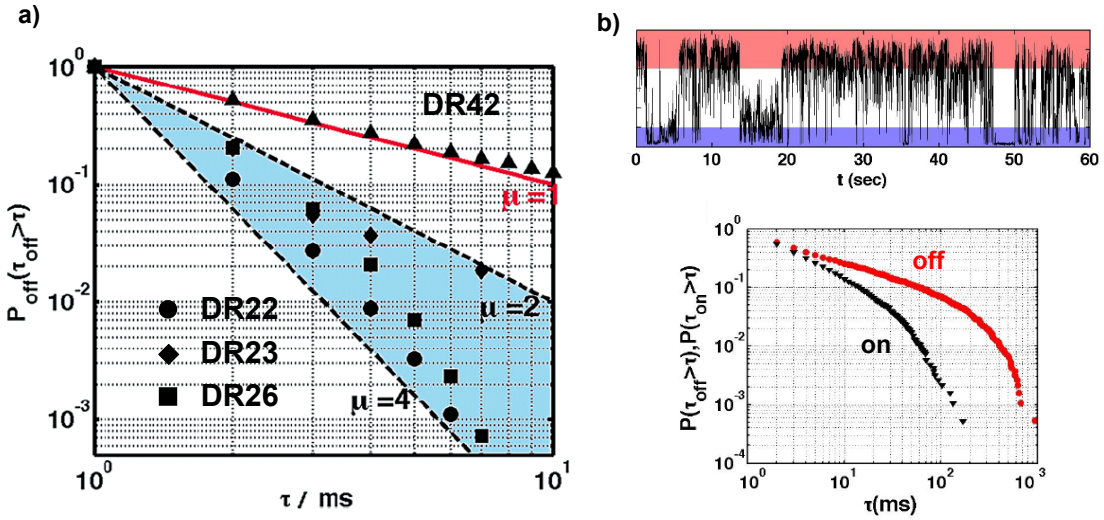

Figure 3.8: (a) Off-times cumulative distributions for thin shell DR42 and thick shell DR22, DR23 and DR26 in a double logarithmic plot. (b) An example of on/off analysis with the bin and threshold method for a single nanocrystal from DR42 sample: PL time-trace $I_{PL}(t)$ with the threshold levels for off and on periods (up) and the cumulative distrbutions $P(t_{on/off} > \tau)$ calculated from the time-trace (down).

and an increased environmental sensitivity due to the thin shell. This behavior coexists with a type A blinking, characterized by fast fluctuations, as shown in the time-trace of Fig. 3.9. Since the Auger effect is still efficient in this kind of structure, the grey states have very low QY and they are not distinguishable from the off states. Therefore the two types of blinking described before are not separable.

3.3.3 Fast grey states dynamics

The presence of grey states is associated with a new dynamics, where a very fast switching between on and grey states is dominant and brings many consequences, as we will see, also on the single photon emission. It is thus necessary to characterize the time scale of these oscillations. This is clearly impossible to do with a classical bin and threshold analysis, because the fluctutations are too fast and there would not be enough data to build an on-time /grey-time distribution.

For this reason we use an approach based on the intensity auto-correlation function $g^{(2)}(\tau)$ as in [97]. $g^{(2)}(\tau)$ is calculated by simply superposing the PL photon counts time-trace $I_{PL}(t)$ detected by a single detector with itself, imposing a delay ranging between 0 and $100ms$. The product $\langle I_{PL}(t)I_{PL}(t+\tau)\rangle$ is time-averaged on a $1s$ range by means of a Matlab code. In order to have the best time resolution we can take a binning time as low as $\Delta t = 0.25ms$. This is limited by our count rates of 100-200 kHz.

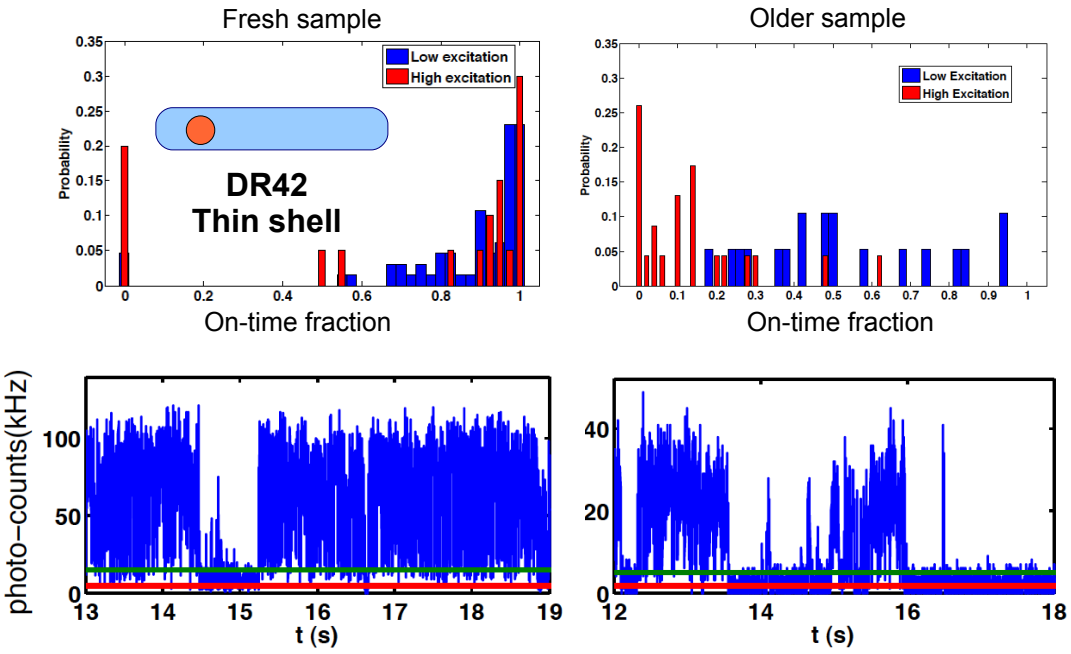

Figure 3.9: Histograms of the on-time fractions for about 30 nanocrystals from DR42 sample at low excitation power (blue) and high excitation power (red). We compare the results for a fresh sample and for a sample left in air conditions for some days.

In order to test the measurement procedure, $g^{(2)}(\tau)$ is first of all calculated for a noise signal, i.e. the fluorescence coming from a region of the glass coverslip without nanocrystals. This fluorescence signal does not show any intensity fluctuations and it can be considered as a nearly Poissonian signal. As expected for a coherent state, $g^{(2)}(\tau)$ is perfectly one for any τ, as it can be seen in Fig. 3.10 c). A very fast decay ($\ll \Delta t = 0.25ms$) at $\tau \approx 0$ is attributed to some artifacts in the computation associated with the intensity of the signal: the higher the signal the lower the effect.

The results of our analysis are exemplified in Fig. 3.10 a) for two different nanocrystals, called nc1 and nc2. In the first case (nc1) $g^{(2)}(\tau)$ tends to a constant value, well above 1, due to the presence of a long off time. In the cases of nc2 the PL shows fast intensity fluctuations and the correspondent $g^{(2)}(\tau)$ goes rapidily to 1, following a nearly exponential decay.
All the measurements can be fitted by an exponential decay plus a constant:

$$f(\tau) = A + Be^{-\frac{\tau}{t_0}}$$

As described in chapter 2, eq. 2.11, an exponential decay is expected for a simple model of two emission states (the bright and the grey states) with finite average durations. Typical decay times t_0=1-2 ms are found for all the DR samples, independently from the core and shell size. In the case of thick shell, non blinking DRs, the constant $A = 1$.

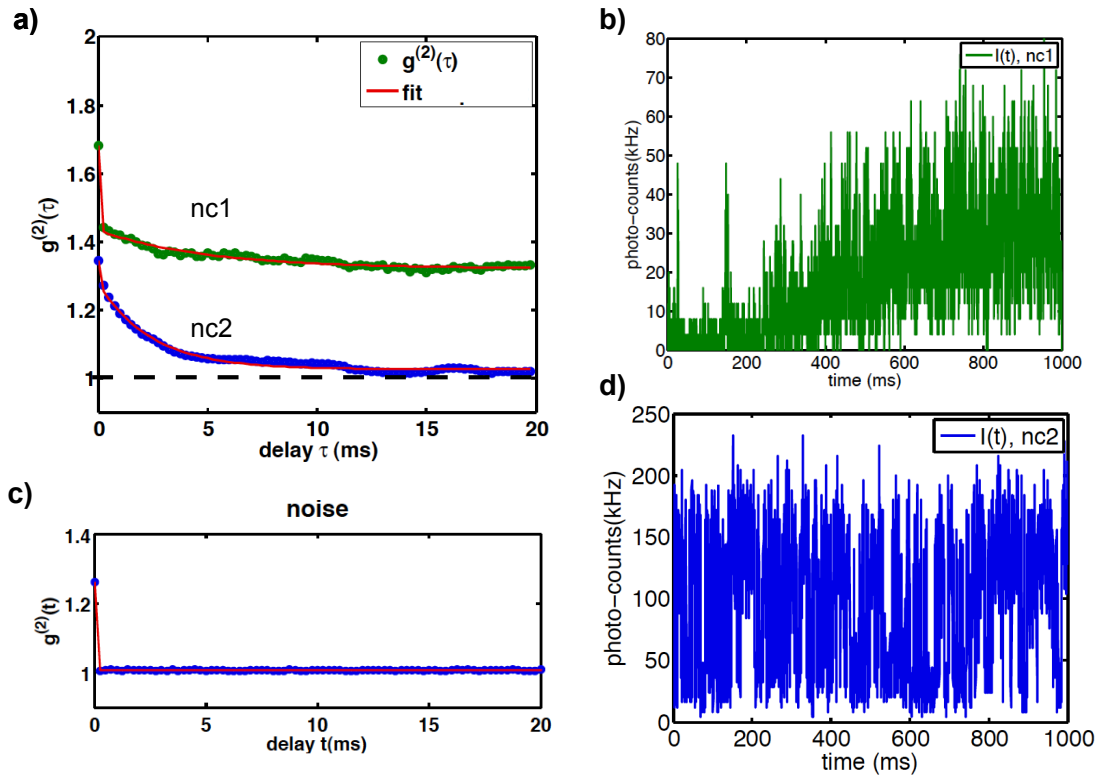

Figure 3.10: a) Examples of intensity auto-correlation function $g^{(2)}(\tau)$ for two different DRs, as calculated from the PL time-traces on the right. Green lines: nc1 showing a long off-grey period. Blue lines: nc2 characterized by fast switching between on and grey states. The auto-correlation functions are fitted by an exponential decay plus a constant (red lines). In the case of long off times a large constant is found, as expected for blinking DRs [97]. Most of non blinking DRs show a behavior similar to nc2: $g^{(2)}(\tau)$ decays to 1 in a typical time of 1-2 ms. c) $g^{(2)}(\tau)$ analysis for a nearly Poissonian noise time-trace. $g^{(2)}(\tau) = 1$ for any time except for a very fast decay around $\tau = 0$, which is attributed to some computational artefacts. b) and d) PL time-traces of nc1 and nc2.

Large constants $A > 1$ are associated with long off periods, typical of blinking DRs like DR42. However an exponential decay is found also for these thin shell DRs. This implies that two different dynamics are present at the same time: a fast switching between states with well defined time-scale occurs together with a non-exponential off-states dynamics.
For blinking CdSe/ZnS nanocrystals no fast exponential decay was found [97]. This is a confirmation that in DRs there is a combination of type A and type B blinking: the first one is dominant in thick shell DRs and the second one in thin shell DRs.

Conclusions In this section we have demonstrated that it is possible to reduce the blinking in DRs by increasing their shell thickness. We characterized the off periods dynamics by calculating

nanocrystals cumulative distributions $P(t_{off} > \tau)$ and on-time fractions. Then we addressed the fast dynamics of the grey states by using the intensity auto-correlation function $g^{(2)}(\tau)$. Off and grey states are interpreted in the framework of the type A and type B models of blinking described in chapter 2.

3.4 Nanocrystals Photo-stability

Up to now we have discussed the blinking behavior and shown how it is detrimental for the development of on demand single photon sources. The blinking is a reversible photo-luminescence bleaching which is usually associated with ionization and an efficient Auger recombination which quenches the PL emission. In addition, a permanent (i.e. much longer than the experimental time scale) PL bleaching can be caused either by multiple ionization events or by an intrinsic photo-chemical instability. Nanocrystals can also enter a low emitting state because of non-radiative processes other than Auger, such as phonon relaxation or energy transfer to trap states.
The resistance of NCs to photo-induced degradation processes is usually referred to as photo-stability.
Photo-stability and blinking are naturally interconnected. They both originate from strong quantum confinement, on one side, and from the interactions of the nano-structure with the environment through its large surface, on the other side.

In the section on blinking, we presented the example of thin shell DR42, which show a great sensitivity to the external environment: the same sample measured some days after the fresh solution was opened has longer blinking period, and photo-bleaches more easily by increasing the excitation power.
Some studied samples, like thick shell DR22 or DR24, are much more robust with respect to chemical- or photo- induced degradation process. For example, once the nanocrystals are drop casted on the coverslip, their PL properties are stable for days, or even for weeks. However, as we will see, a degradation process almost always occurs when the sample is excited at high laser intensity. This can be explained by the efficiency of the non-radiative Auger processes, which transfers energy to the excited charges and thus can favor chemical reactions, creating defect trap states on the surface.
Other samples, like DR21, or other thin shell DRs which we studied but that are not reported in this thesis, show a poor intrinsic optical quality even if the sample is fresh: some single nanocrystals can still be found with interesting QY and single photon emission properties, but these properties are very dispersed within the sample, and most of the DRs are simply bad fluorophores.

We also underlined that the state of conservation of the sample can be crucial. It is necessary to keep the DRs solution at high concentration, otherwise a substantial degradation process occurs, probably caused by the loss of the passivating organic ligands.
The coordinating organic ligands used to passivate the nanocrystal surface strongly contribute to the nanocrystal optical properties as the PL quantum yield or the photo-stability. Unfortunately, the ligands can become uncoordinated from the nanocrystal surface, and as organic molecules, they can be damaged by the exposure to the light sources used for nanocrystal photo-excitation. The ligand loss through physical separation or photochemistry results in uncontrolled changes in QYs and, in the case of irreversible and complete loss, in permanent darkening or photobleaching.

A degradation of the emission properties can also occur because of some chemical reactions caused by the surface properties of the substrate or by the atmosphere to which the DRs are

exposed. For instance, PL has been often observed to decrease if the sample coverslip is put under vacuum, and also differences have been remarked between the deposition on a glass or a washed sapphire microscope coverslip.

In this section, we will first review general tips about photo-stability and its relation with the possibility of single photon emission.
Then we will see how the single DRs emission properties, especially the quantum properties can degrade as a consequence of high intensity photo-excitation. In particular we observe that a good single photon emitter can lose this quantum property as a consequence of a degradation process, such as photo-bleaching.
In the second part, we describe ensemble measurements performed on two specific samples, namely DR22 and DR21. We develop a method which allows to study photo-stability and single photon emission properties at the same time, using an ensemble measurement. It is based on a measurement of PL as a function of the excitation power, according to the model discussed in section 2.4.3.
In order to show the flexibility of this method, we also study the effect of the interaction with an external atmosphere, which is another critical point for all nano-structures having high surface-to-volume ratio. The setup for ensemble measurements was entirely built during my first PhD year in Milan (Italy).

3.4.1 Photo-stability and single photon emission

The photo-stability is highly relevant to the applications of colloidal core/shell nanocrystals.
Compared to alternative fluorophores, such as organic dyes or molecules, colloidal core/shell nanocrystals are characterized by significantly enhanced photo-stabilility.
For example, fluorescent molecules, core-only CdSe samples, as well as thin shell CdSe/ZnS nanocrystals photo-bleach within some seconds, when excited well above the saturation [72].
Photo-induced effects, such as photo-enhanced luminescence, photo-oxidation, photo-bleaching have been extensively investigated. We refer to [122] for a review of photo-stability in dots-in-rod nano-structures.

Many efforts have been done in order to improve the intrinsic photo-stability of colloidal nanocrystals, by means of organic or inorganic chemistry. the suppression of the Auger recombination, together with a high photo-stability, have been demonstrated in giant shell CdSe/CdS NCs [72] [73]. However this improvement in PL stability has lead to a drawback: non-blinking NCs, such as self-assembled quantum dots, are usually no longer good single photon emitters [75].

In order to reach a good trade-off between preserving single photon emission and reaching good photo-stability, many strategies can be pursued: tuning dimension, shape and material of the shell, selecting suitable coordinating ligands [116] [117], applying electrochemical potential or choosing a suitable substrate in order to control the NCs state of charge [65] [67].
All these parameters can be source of great variability in the quantum properties, even within a same sample of NCs. This fact could explain why the mechanisms of photo-induced phenomena are still unclear [123].

For example the presence of oxygen can be detrimental for some kind of NCs [118], in particular core only or thin shell nanocrystals, but it was shown to boost PL for other types [119].

Photo-stability can be assessed by ensemble measurements, for example by exposing the NCs solution to UV light and by observing the PL spectrum. However these kinds of tests do not give any information about quantum optical properties.
On the other hand, measurements on single isolated NCs, which are usually required to assess photon statistics, may not be statistically significant for quantifying the photo-stability of the ensemble. In fact, this kind of measurements usually relies on a pre-selection of bright and photo-stable NCs.

For this reason, a fast and efficient method allowing to evaluate both the photo-stability and the overall single photon source quality of a sample of NCs is expected to be very useful.
Such a method would allow, for instance, to select a sample in which most of the NCs are good single-photon sources from another one in which this property is much more dispersed, avoiding long measurements on single emitters. It can also test the state of conservation of a sample, or its different reactivity when deposited on different substrates.

We will compare two samples, namely DR21 and DR22. These two samples have been chosen because they present a similar behavior in terms of auto-correlation function, spectral properties and radiative lifetime, when measurements are performed on a selection of single nanocrystals. However, ensemble measurements will reveal very different photo-stability properties.

Measurements on single DRs First of all, anti-bunching measurements on single NCs are performed to investigate their single photon behavior. This test is performed on a selection of about 10 NCs which are chosen because they are bright enough to be detected on a CCD camera and because their PL is stable enough to go through an entire session of measurements.
The result of our measurements, depicted in Fig.3.11(a), is that both DR21 and DR22 show a good single photon emission for any studied excitation power.
This is confirmed also by PL measurements as a function of the excitation power, as described in section 2.4.3. As shown in Fig. 3.11, a saturation of the emission while increasing the excitation intensity is observed both for DR21 and DR22.
PL photon counts as a function of the excitation intensity can be roughly fitted by the equation derived in section 2.4.3:

$$I_{PL}(P) = I_{sat}\left(1 - e^{-\frac{P}{P_{sat}}}\right)$$

In this way the excitation power P is converted to a number of injected electron-hole pairs $\langle N \rangle$, as shown in Fig. 3.11. This means that the contribution of the multi-excitons emission is almost negligible, as already observed by comparing DR22 and DR24 in section 3.2, Fig. 3.6.
In DR21 the saturation level I_{sat} is about 60 % lower than in DR22, meaning that their average quantum yield $\langle QY_1 \rangle_t$ is lower.

However not all the nanocrystals survive to high excitation intensity. After excitation at high power ($\langle N \rangle \gg 1$), some NCs start to blink more. Single photon quantum yield QY_1 becomes lower, the grey states more frequent and some DRs irreversibly bleach in a state which is slightly

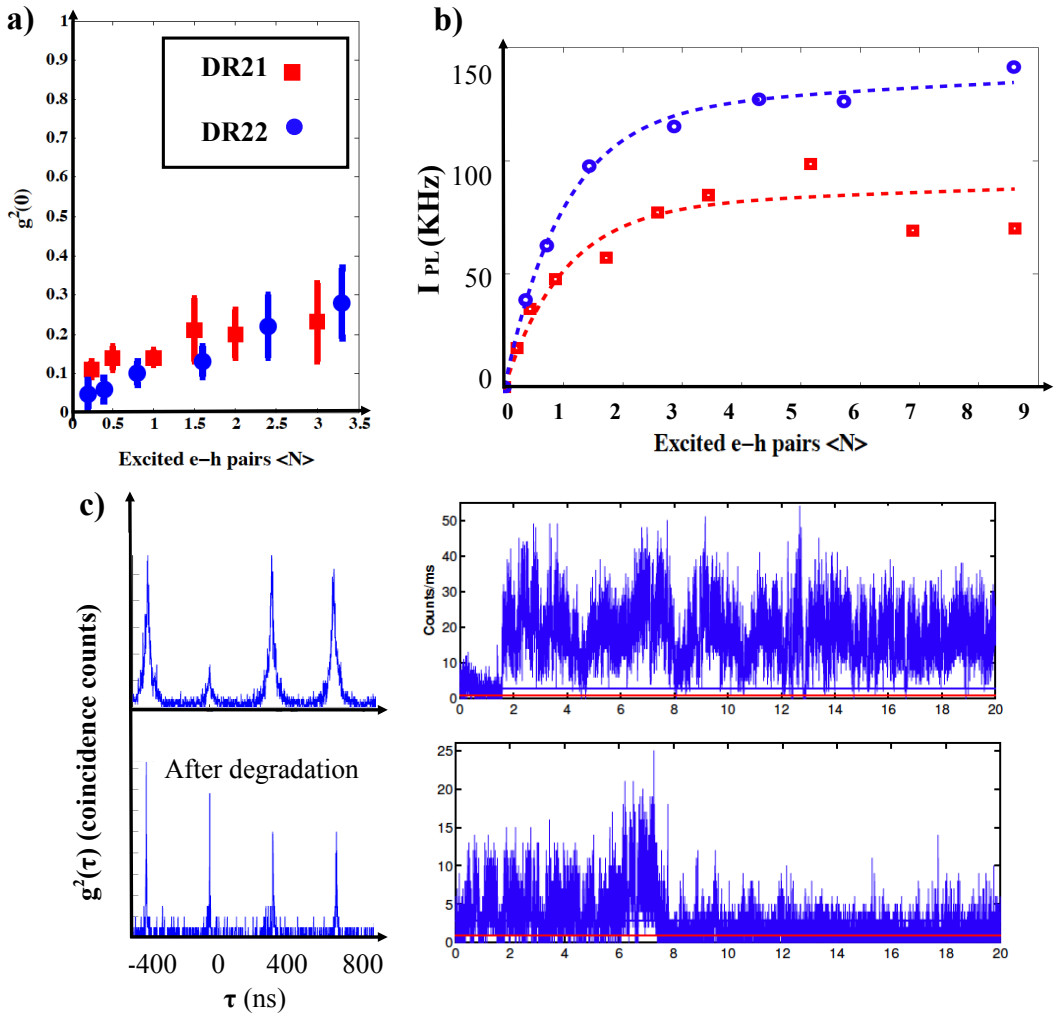

Figure 3.11: (a) $g^2(0)$ measurements as a function of the number of electron-hole pairs $\langle N \rangle$ excited by a laser pulse. Despite their different geometrical structure, DR21 and DR22 show similar behaviors. (b) PL counts as a function of $\langle N \rangle$ for DR21 (red squares) and DR22 (blue dots). Points are average values for about 10 single DRs and both curves are fitted by the exponential of eq.(2.9). I_{PL} for DR21 is about 60% of DR22, which implies that they have a different single photon Quantum Yield QY_1. (c) Example of photo-induced degradation of emission properties. Up: $g^2(\tau)$ and PL time-trace $I_{PL}(t)$ measured at low excitation power, before photo-induced degradation. Down: $g^2(\tau)$ and $I_{PL}(t)$ from the same nanocrystal, at the same excitation power, but after exposure to high pump fluence. In the picture below, total photon counts are less, $g^2(0)$ close to 1, and lifetime is decreased.

above the noise level. In some cases a low residual emission can still be detected. The result is exemplified in Fig.3.11(c): the same NC which exhibited a good single photon emission quality, with a measured average quantum yield $\langle QY_1 \rangle_t$ between 30 and 50%, starts to emit much less.

The average lifetime, which was between 30 and 60 ns, becomes less than 2 ns (comparable to our system resolution) and, above all, $g^2(0)$ becomes closer to 1. A similar photo-induced degradation effect was also observed in [120] for spherical nanocrystals.
This behavior has been observed for almost any sample studied during this thesis, but the threshold intensity for photo-degradation can vary from one sample to another, from one nanocrystal to another and also depends on the state of conservation. For example DR21 seem to be in average less stable than DR22: in Fig. 3.11 (b) the last two points of the curve for DR21 are lower because DRs start to photo-bleach, and the average QY_1 in DR21 is less than in DR22.
However, a quantitative comparison would require a statistically significant sample of DRs. Moreover it worths to point out that a pre-selection of single nanocrystals is naturally made, because only the brightest particles can be actually observed on the CCD camera. There could be within a certain sample of DRs, for example, an entire population of low-emitting particles which cannot be accounted by this kind of analysis on single emitters.

Summarizing, both DR21 and DR22 have a similar behavior in terms of $g^2(0)$ when a selection of bright and stable NCs is performed, as clearly shown in Fig.3.11 (a). However, in both cases, some NCs degrade over time, especially under high excitation.
In single NC measurements it is difficult to see a difference between the two samples, since both of them appear to be good single photon source. We will show that this problem can be circumvented by an ensemble measurement, which can demonstrate that the fraction of good single-photon source NCs is very different in the 2 samples, as well as their intrinsic photo-stability.

3.4.2 Photo-stability ensemble measurements

Setup for Ensemble Measurements The system for NCs ensemble measurements is a home-made confocal microscope, depicted in Fig.3.12(a). It is similar to the one used in single NC $g^2(0)$ measurements, with only one APD detector; the excitation is provided by a commercial 405nm continuous wave diode laser. The beam is enlarged by a telescopic system and then focalized on the sample by means of an air objective with numerical aperture $NA = 0.85$. The objective is embedded into a structure that allows us to pump a gas flow of nitrogen directly onto the glass. DRs from a toluene solution at a concentration of $10^{-7}M$ are drop casted onto a glass cover slip. This density is high enough to collect a good PL signal also at low excitation intensity. By using such a high concentration, which is almost the same as the one used for realizing the TEM images of Fig.3.1, a monolayer of about $10^3 - 10^4$ DRs in 1 μm^2 is obtained. The long organic ligands [16] surrounding DRs keep them at a distance of 2-3 nm which is enough to neglect strong interactions like electron tunneling, while longer range dipole interactions like Forster Resonant Energy Transfer (FRET) [121] are limited by the narrow PL spectrum associated with low size dispersion. This is verified by comparing the spectrum of a monolayer of DRs with the same spectrum previously taken in solution.
The sample is mounted on a piezoelectric ceramic. In this way we can perform a scan of the surface in order to check the uniform distribution of emitters. PL is collected from a central region of the laser beam by means of a $100\mu m$ pin-hole, as illustrated in inset of Fig.3.12(a).

In this way an uniform excitation intensity is ensured. PL is transmitted by a dichroic mirror and sent to an APD. The laser power is controlled by a voltage signal provided via computer. An acquisition card allows monitoring the input power, measuring the reflection of the input polarized beam on a beam splitter. The counts detected by the APD are registered by the same card.

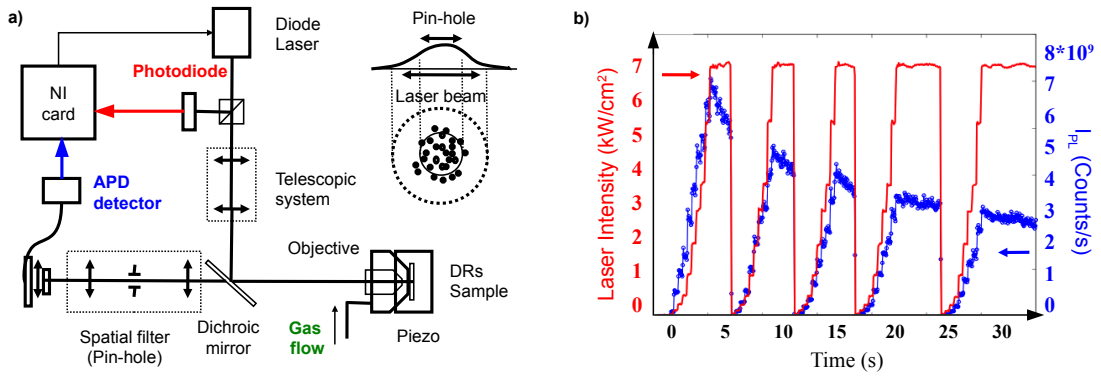

Figure 3.12: (a) Experimental apparatus for NCs ensemble measurements. (b) Decay of the PL of DR21 measured with an APD as a function of time under $7kW/cm^2$ laser excitation. In addition, at selected times t=0, 5, 11, 17 and 24 sec, the laser is suddenly turned off and then turned on again to maximum intensity on a time of 3 to 4 sec. The variation of PL during such an event is shown together with the corresponding input laser intensity.

The NCs are excited at about $7kW/cm^2$, well above the expected saturation for both the samples under study. With this high excitation power, PL in both cases decays with a time constant of the order of a few tens of seconds, showing a degradation of the emission because of the interactions of photo-excited charges with the environment. At 405 nm the absorption is due to a quasi-continuum of excitonic energy levels, so the number of excited electron-hole pairs is nearly proportional to the volume of the NC.
Since the spontaneous decay time of both DR21 and DR22 is almost the same, the same number of excitons is excited per unit volume and per unit time.
In addition, at some specific times, we suddenly decrease the excitation power down to $25W/cm^2$, well under saturation, and we scan it back to the value of $7kW/cm^2$ in a few seconds. PL is measured during this scan as can be seen in the inset of Fig.3.12(b).

As a result, we have access to the variation of PL as a function of the excitation intensity at different times during the progressive degradation of the DRs. These PL curves, measured with an APD, are shown in Fig. 3.13.
The measurement can be performed in a standard atmosphere (in the presence of oxygen and even water molecules) or by continuously fluxing nitrogen onto the sample, thus creating an

inert atmosphere around the nanocrystals.

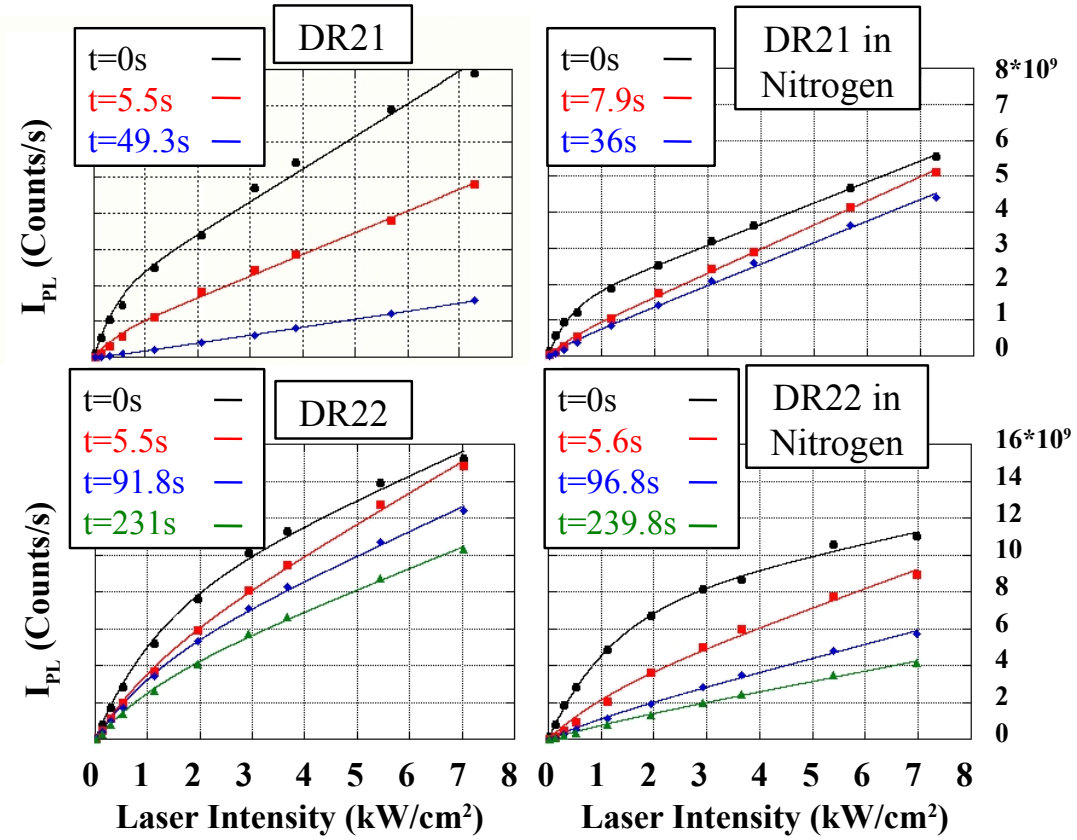

Figure 3.13: Ensemble PL as a function of the laser intensity, at different times during PL degradation induced by continuous $7kW/cm^2$ photo-excitation. Left: in air, right: under a nitrogen flux. Lines: Fits with the function in eq.(3.2).

Results and interpretation It can be seen that ensemble PL plots do not show the saturated behavior described by eq.(2.9) and found in single NC measurements on a selection of DRs, Fig.3.11(b). Moreover, as the photo-bleaching progresses and PL decreases, the shape of the curves tends to a straight line.

The PL curves can be fitted by the function:

$$I_{PL}(P) = \alpha \left(1 - e^{-\frac{P}{P_{sat}}}\right) + \beta P \tag{3.2}$$

The value P_{sat} is the same for all the plots, both for oxygen and nitrogen.
It is fixed by an independent measurement made by a fast scan of the surface by the piezo-electric control. Since each point is excited only for about $100ms$, photo-bleaching can be neglected and a nearly complete saturation is retrieved, as shown in Fig. 3.14 for DR22, which is similar to

that found in single nanocrystal measurements.
This technique also allows to compare the PL efficiency in the presence of nitrogen or of oxygen and thus to rescale the curves in Fig. 3.13. Indeed, the two mesurements in air and in nitrogen in Fig. 3.13 are performed on two different regions, since the photo-bleaching is irreversible, but the density of DRs is not the same everywhere. The maximum of the PL in the presence of nitrogen is scaled to the maximum in the presence of oxygen by the ratio of the maxima found in Fig. 3.14.

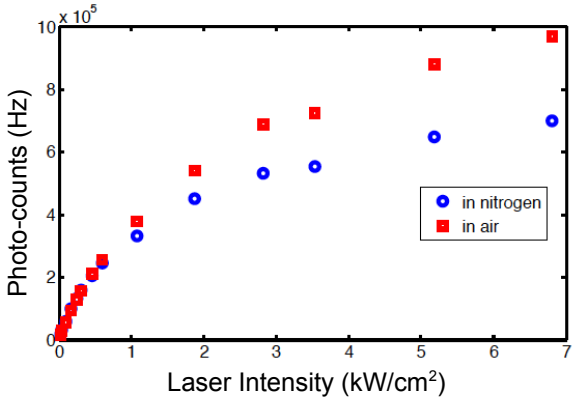

Figure 3.14: Ensemble saturation measurements for DR22: PL is collected while fast scanning the surface for each excitation intensity. Blue points correspond to measurements in nitrogen, red points to a standard atmosphere.

The first term of the fit function in eq. 3.2 is the exponential variation from eq.(2.9), due to the saturation of DRs which are good single photon sources, and the second one gives a linear dependence on the excitation power P.
As we have already discussed in section 2.4.3, the proportionality of the PL signal with the excitation power emerges for emitters in which all the multi-excitonic quantum yield QY_m become comparable.
This linear dependence is consistent with the increase in $g^2(0)$ observed in some single DRs, after the exposure to a high photo-excitation, as it can be seen in Fig.3.11 (c). This loss of the single photon emission character is accompanied by a reduction of the emitted intensity I_{PL}, i.e. by a reduction of QY_1 which makes it comparable to the multi-exciton quantum yields. DRs can also be already in a low emitting state after the synthesis because of an intrinsic quality of the sample.

Therefore, the coefficients α and β in eq.(3.2) can be interpreted as two populations of different DRs n_1 and n_2, the first with high single photon Quantum Yield QY_1 and the second with low overall Quantum Yield QY':

$$I_{PL}(P) = n_1 QY_1 \left(1 - e^{-\frac{P}{P_{sat}}}\right) + n_2 QY' \frac{P}{P_{sat}} \tag{3.3}$$

A priori a linear contribution to $I_{PL}(P)$ could be assigned to a suppression of Auger rates, as

DR21					
Oxygen			Nitrogen		
t(s)	α	β	t(s)	α	β
0	1.6	0.9	0	0.54	0.24
5.5	0.44	0.6	7.9	0.12	0.28
49.3	0	0.2	36	0.07	0.25
DR22					
0	6.6	1.3	0	5.8	0.5
5.5	3.3	1.7	5.6	1.6	0.9
91.8	3.4	1.3	96.8	0.5	0.7
231	2.4	1.1	239.8	0.3	0.5

Table 3.1: Summary of fit parameters extracted by ensemble PL measurements in Fig.3.13, according to eq.(3.2).

observed in 'giant' NCs [75] and in Fig. 3.6 for DR24. However, since ensemble PL decreases in time over the whole duration of the experiment, as can be seen from the curves taken at various times in Fig.3.13, another degradation process must be considered.
This process leads to the decrease of the single exciton quantum yield QY_1 which becomes comparable to all the other multi-excitonic recombination yields QY_m. As pointed out above, this can be associated either with a highly ionized state in which all QY_m (included QY_1) scale as $\frac{\gamma_R}{\gamma_A}$ or with the opening of non-radiative channels, such as the creation of new defects or dangling bonds at the surface, leading to $QY_m \approx \frac{\gamma_R}{\gamma_{NR}}$.
In both cases, the overall PL is expected to decrease and single photon emission quantum properties are gradually lost. In the present case the gradual disappearance of the saturation observed in ensemble PL measurements can be assigned to a combination of the degradation processes and of the change in Auger rate γ_A.

The results from the fit are summarized in table 1.
In most of the cases, an unexpected increase in β coefficient from $t = 0s$ to the second studied time (between 5 and 8 sec) is found. This is mainly due to an experimental artifact. In the first few seconds of excitation, the PL decay time can be indeed very short and become comparable to the minimum time in which the laser intensity can be changed and PL counts collected ($\approx 4s$). A priori, this problem could be overcome by a faster electronic control.

An interesting feature of this ensemble method is that it allows to differentiate our two kinds of nanocrystals DR21 and DR22 better than a single emitter study. In Fig.3.11(a) DR21 and DR22 appeared to have a similar performance as single photon sources, whereas Fig. 3.13 (left panels) shows clearly that they have very different behaviors.
DR21 loose any saturation component after few seconds, while DR22 at $t = 231s$ have a weight of the exponential which is still more than $\frac{1}{3}$ of what it was at $t = 0s$. Furthermore this method allows to study the different behaviour of the nanocrystals in an atmosphere of pure nitrogen, as can be seen in Fig. 3.13 (right panels).

In both samples at $t = 0s$ PL mean intensity is lower when the samples are excited under nitrogen atmosphere.
In the case of DR21, the saturation component disappears very rapidly both under nitrogen and standard air conditions, while nitrogen seems to slow down in some way a degradation process affecting the linear PL component.
In the case of DR22, on the other hand, the presence of oxygen in the atmosphere surrounding the nanocrystals is found to be very important for preserving the single photon character of NCs. The role of the oxygen in preserving both photon statistics and photo-stability, at least under conditions of high excitation, can be interpreted, as suggested by Müller [119], in terms of controlling the NC state of charge. The tendency to hole trapping under photo-excitation, and so the prevalence of negative charged NCs (negative trion), has been recently demonstrated in spherical NCs of CdSe/CdS [81]. Thus, in standard atmospheric conditions, a transfer of electrons to oxygen is possible, which can lead to neutralization of charged, non emissive DRs.

Conclusions and perspectives In conclusion we have described a new ensemble-based experimental method to study the quality of a sample of NCs as single photon source and its photo-stability under condition of high excitation and in the presence or absence of oxygen. We demonstrated the interest of the method by identifying significant differences between two samples of DR with similar performances as single photon sources when single isolated NCs were observed.
This method can easily be applied to any nano-structures that need to be characterized as single photon source. It allows a fast discrimination between different kinds of samples, or different synthesis of the same sample, to test the quality of the conservation of a sample, or its interaction with a substrate.

The previous measurements represent a proof of the validity and of the practical utility of the method, and these results has been recently published [124].
Since the laboratory in Milan, where I built the setup for ensemble measurements, had to move just after I left for Paris, I did not have time to characterize other samples by using this method. For instance, it would be interesting to study the effect of a nitrogen atmosphere on thin shell samples like DR42 and DR76, because they are expected to be more sensitive to photo-oxidation, as suggested by blinking measurements. Also ensemble measurements on thick shell DR24 could reveal a particular behavior, since this sample showed quite high $g^{(2)}(0)$ but apparently should be more photo-stable.

3.5 Single nanocrystal lifetimes

In this section we want to provide a complete characterization of all studied dot-in-rods nanocrystals in terms of their room temperature decay lifetimes.
In time-correlated single photon counting experiments, lifetimes are directly measured by recording the arrival times of photons with respect to the laser excitation trigger. The decay signal is then fitted by a multi-exponential function, and different lifetime constants can be extracted. The measured decay rates (inverse of lifetime) are the sum of radiative and non-radiative rates.

DRs will be studied one by one, and as a function of the excitation power, i.e. of the mean number $\langle N_{eh} \rangle$ of injected electron hole pairs.
In quasi-II type heterostructures like CdSe/CdS DRs the radiative rate γ_R can strongly varies from one nanocrystal to another because of different levels of delocalization of the electronic wavefunction within the shell. Because of this dispersion, lifetime measurements on single DRs can provide much more information than ensemble decays, where different lifetime constants would be simply averaged. Ensemble lifetime measurements would not allow to address the complexity of nanocrystals behavior, at least in thick shell DRs.
As we already discussed, a lifetime analysis can provide many different informations about the fundamental physical processes in a colloidal quantum dots. First of all, the radiative lifetimes can give information about the electron wavefunction delocalization. Secondly, the photo-luminescence intensity fluctuations, observed in the previous sections, are often accompanied by fluctuations of lifetimes, according to the type A models of blinking widely discussed in chapter 2. By comparing the lifetime data and the previous measurements of quantum yield, a qualitative estimation of the radiative and non-radiative lifetimes can be derived.

Fitting procedure The recovery of the decay rates from a multi-exponential fit of the decay curves is a classical problem for the optical characterization of fluorophores, and it has been addressed for example in [128].
There may be many different rates combinations which could describe the corresponding decay curve equally well. For example, any decay curve can be reasonably fitted with a sum of four exponentials [127]. This is why fitting a lifetime decay curve from time correlated single photon counting (TCSPC) is not as trivial as it could appear at first glance.

The experimental decay curves $L(t)$ of single nanocrystals, normalized to the mamimum value at $t = 0ns$, can be fitted by the sum of 2 or 3 exponentials, as illustrated in Fig. 3.15 a):

$$L_{fit}(t) = a_F \exp\left(-\frac{t}{\tau_F}\right) + a_0 \exp\left(-\frac{t}{\tau_0}\right) + a_1 \exp\left(-\frac{t}{\tau_1}\right) \tag{3.4}$$

The weights of the exponential functions are normalized $a_F + a_0 + a_1 = 1$.

A first fast time constant τ_F is upper bounded at 2-3 ns, in order to take into account the fast multi-exciton dynamics and at the same time the fluorescence noise. This fluorescence noise comes from the glass or from some residuals on the coverslip (in the same spectral region of the DRs emission) and gives a spurious lifetime signal of about 3 ns. The weight of the fast component a_F increases at high power, and the values τ_F found by the fit are often between 1

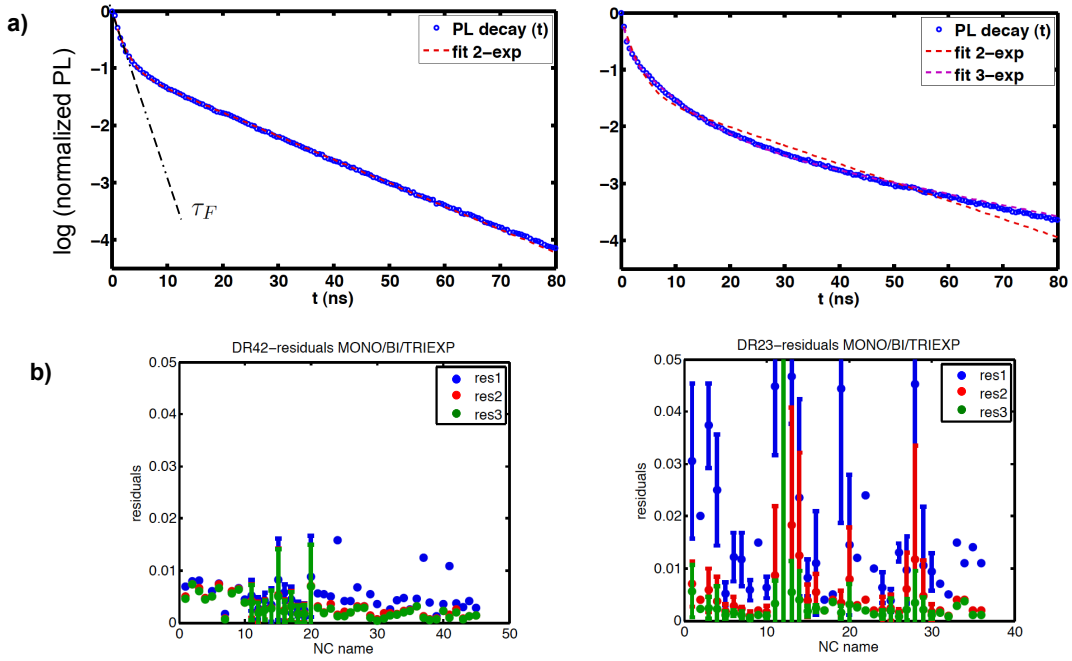

Figure 3.15: a) PL decay curves in logarithmic scale for two single nanocrystals from thin shell DR42 sample (left) and thick shell DR23 (right). In the first case, the plot can be fitted by the sum of 2 exponential functions, the fast component with $\tau_F \simeq 3ns$ takes into account the noise and the multi-exciton decay. In the second case at least 3 exponentials are necessary. b) Normalized residuals from a mono-exponential (blue), a bi-exponential (red) and a 3-exponential (green) fit for a set of single DRs. Error bars are calculated on the values found for different excitation powers. On the left, the residuals for thin shell DR42 show that a mono-exponential fit properly the lifetime for almost all the particles. For thick shell DR23 (on the right), a mono-exponential fit is not consistent for most of the DRs, while a bi-exponential fit gives residuals as low as a 3-exponential fit.

and 2 ns.
τ_F contains informations about the multi-excitons decay, but it will not be considered in our analysis for two reasons. Firstly, the contribution from the multi-excitons decay can not be separated from the spurious lifetime of the noise. Secondly, the temporal resolution of the acquisition card PicoHarp 300 is 512 ps, and thus it is difficult to fit signal with a lifetime of 1-2 ns.
For these reasons, short lifetimes like the bi-excitonic decay cannot be measured by TCSPC, and would require the high temporal resolution given by a Streak Camera.

The rest of the decay curve can be fitted by 1 or 2 exponentials, depending on the specific nanocrystal. We will often refer to this as mono-exponential or bi-exponential fitting, even if we have to remember that there is always an additional fast component τ_F.

Typically, thin shell, blinking DRs, like DR42 or DR76, can be well fitted by a mono-exponential, while thick shell samples, like DR22, DR23 or DR24, need 2 exponentials.
This is coherent with the charging model of fast switching between a grey state, characterized by τ_1, and a bright, neutral state, characterized by τ_0. Since the off periods do not provide any contribution to the PL decay signal, a mono-exponential behavior is a signature of blinking nanocrystals and τ_0 is just the lifetime of the bright state.

In Fig. 3.15 b) we calculated the normalized residuals from a least-squares fitting procedure for many different single nanocrystals. As it is evident, thin shell DR42 can be well fitted by a mono-exponential (plus the fast component), while this fit is bad for most of nanocrystals from DR23 sample. Error bars indicate average on different studied powers.
The absolute goodness of the fit can be evaluated by comparing the residuals with the fit made with a total number of 4 exponentials (green points), which should give a nearly perfect fit [127]. This is a proof that a model based on one emission level for blinking nanocrystals, like DR42, or on two emission levels for non-blinking nanocrystals, like DR23, is adequate.

As mentioned before, a general issue in the lifetime fitting is that the absolute values of the two time constants τ_0 and τ_1 cannot be estimated with high accuracy. In fact, the superposition of two exponentials of the same order of magnitude can be reproduced by several combinations of time constants and weights a_0 and a_1 in eq. 3.4.
However, the existence of two well-defined time constants can be confirmed by using different kinds of analysis, such as studying the evolution of the lifetime with the excitation power or separating the PL signal in different intensity levels (threshold method), as we will describe in the following section.
Moreover, we will often use average lifetimes, which are less sensitive to the specific fitting procedure.

3.5.1 Lifetime and grey state

Fig. 3.16 shows an example of lifetime analysis on a single nanocrystal from thick shell, non blinking DR22 sample. Two thresholds are defined in the PL time-trace in such a way that 1/4 of the total signal comes from the upper part (called high level in figure, blue points) and 1/4 from the lower part of the curve (called low, red points). Since the time scale of the intensity fluctuations is very short (1-2 ms, see section 3.3) a short time binning for photo-counting must be chosen (0.5 ms).
In this way two different decay curves are built with the same number of photon counts and the existence of separated emissive levels can be tested. Fig. 3.16 shows this kind of analysis for different excitation powers.

At low power, $\langle N_{eh} \rangle = 0.4$, the threshold analysis gives the same decay time for the high and the low level. This means that there is only one emission level. We can deduce that at low power only the bright state is present, because the probability of photo-induced Auger ionization is low. By increasing the power a second time constant emerges for the photons coming from the low level, corresponding to the grey state emission. This lifetime τ_1 is better defined for $\langle N_{eh} \rangle = 3.2$, while for $\langle N_{eh} \rangle = 1.6$ the grey state and the bright state are still too mixed to

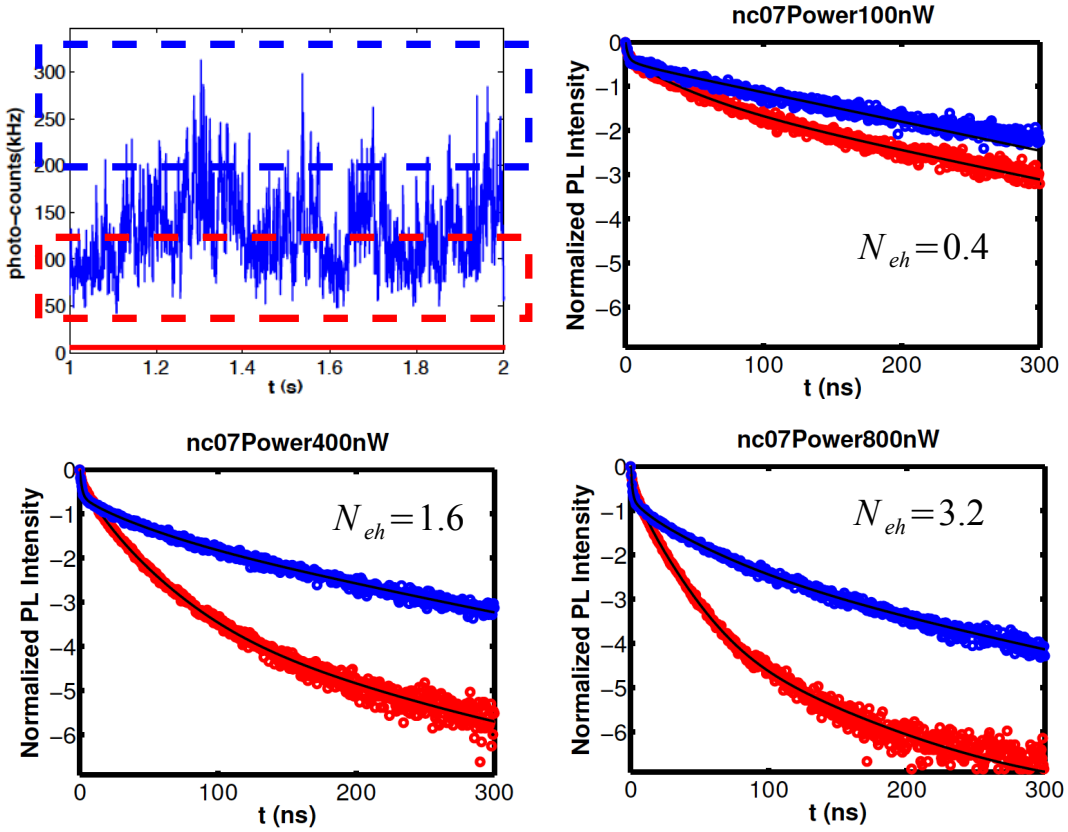

Figure 3.16: Threshold method for the lifetime analysis. Photon counts are selected from different intensity levels of the time-trace, shown in blue (high level) and red (low level) and their decay lifetime is analyzed separately. The results are shown for one selected nanocrystal, excited at different powers, which are reported on the plots. At low power, only one lifetime constant τ_0 can be found, while at higher excitation a shorter constant τ_1 emerge. The high level lifetime τ_0 (blue) is nearly constant while increasing N_{eh}, justifying its interpretation as the bright state lifetime.

estimate τ_1 with good precision. At high power, two nearly mono-exponential decays are found for the high and the low level, with lifetimes $\tau_0 = 150ns$ and $\tau_1 = 20ns$.
Interestingly, the photons from the higher part of the curve show the same long time constant τ_0 for any power. It can be assigned to the bright state.
The weight of a very short time constant $\tau_F \approx 2ns$ increases with the excitation power, coherently with the increasing contribution of radiative multi-excitonic recombinations.

In section 3.2 we found the maximal quantum yield $QY_{max} \approx 100\%$ for most of the nanocrystals, and we associated this value with the bright state quantum yield $QY_1^{(0)}$ (the superscript (0) indicates a neutral state of charge).
This observation implies $\gamma_{NR} \ll \gamma_R$ and so the measured long time constant gives directly the

radiative lifetime:

$$\tau_0 \simeq 1/\gamma_R = \tau_R$$

We can then estimate the Auger rate for the negative trion. According to the scaling equations 2.1, the measured rate γ_i for a state with one hole and two electrons should be:

$$\gamma_i(n_e = 2, n_h = 1) \simeq 2\gamma_R + 2\gamma_A^e = \frac{1}{\tau_1}$$

which gives $\gamma_A^e \simeq 1/60ns^{-1}$.
The quantum yield $QY_1^{(-1)}$ (the superscript (-1) indicates a negatively charged state) for this grey state $X^{(-1)}$ can be derived using the definition in eq. 2.2:

$$QY_1^{(-1)} = \frac{2\gamma_R}{2\gamma_R + 2\gamma_A^e} = \frac{2\tau_1}{\tau_0} \simeq 0.27$$

This value is compatible with the lower intensity level in the time trace of Fig. 3.16, which is about 1/3 of the maximum. The oscillations between the bright state and the grey state determine a measured average single photon quantum yield $\langle QY_1 \rangle_t \simeq 45\%$
However, because of the fast time-scale of intensity fluctuations, it is difficult to estimate the trion $QY_1^{(-1)}$ directly from the photon distribution, which is dominated by the Poissonian shot noise.

Similar analysis have been carried out for all non blinking DRs, showing that the model of fast switching between grey and bright states is coherent with both intensity and lifetime measurements.

3.5.2 Average lifetime as a function of the excitation power

A statistical characterization of the lifetime as a function of the excitation power can reveal information about the dynamics of photo-charging. As we will see in the following, this fact has important consequences on the auto-correlation function, and so on the quality of multi-photon suppression. For this kind of study we will consider an *average lifetime* t_{avg}. Given the experimental decay curve $L(t)$, t_{avg} is defined as follows:

$$t_{avg} = \frac{\int tL(t)\ dt}{\int L(t)\ dt}$$

This quantity can also be calculated from the lifetime fit function $L_{fit}(t)$, as defined in eq. 3.4:

$$t_{avg} = a_F\tau_F^2 + a_0\tau_0^2 + a_1\tau_1^2$$

where a_i (dimensions: inverse of a time) are the normalized weights of the exponential functions used for the fit and τ_i their time constants.
This second definition is more convenient. Indeed, by first fitting the curve $L(t)$, we can get rid of the contribution from multi-photon emission (and of noise of course), which is accounted by the fast component τ_F. Therefore t_{avg} can be redefined as follows:

$$t_{avg} = \frac{a_0\tau_0^2 + a_1\tau_1^2}{a_0\tau_0 + a_1\tau_1} = p_0\tau_0 + p_1\tau_1 \tag{3.5}$$

where

$$p_{0,1} = \frac{a_{0,1}\tau_{0,1}}{a_0\tau_0 + a_1\tau_1}$$

are the so called photon weights, representing the fraction of photon counts from each emission state.

It is easy to demonstrate that t_{avg} is much less sensitive to fitting errors than the specific estimation of $a_{0,1}$ and $\tau_{0,1}$. Of course in the case of a mono-exponential fit, like for DR42, $t_{avg} = \tau_0$.

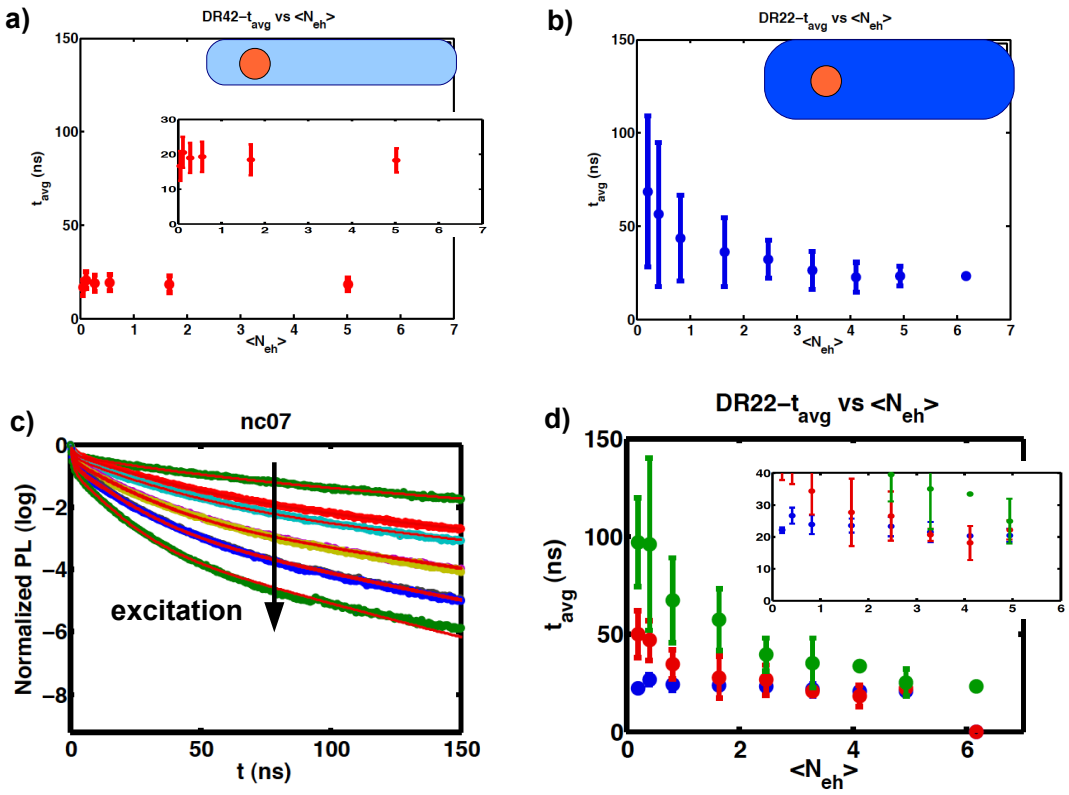

Figure 3.17: Average lifetime t_{avg} as a function of the excitation intensity. a) Lifetimes for thin shell, blinking DR42 are nearly mono-exponential with values around $t_{avg} = \tau_0 \simeq 20ns$, as shown in the inset. t_{avg} does not change with increasing the excitation, since off-periods do not contribute to the decay signal. b) t_{avg} as a function of $\langle N_{eh} \rangle$ for about 12 single nanocrystals from non blinking DR22. t_{avg} decreases as a consequence of the increasing probability of photocharging and thus of the weight of the grey state. c) An example of PL decay curves at different powers. d) The same as in b) but single nanocrystals are grouped together according to their measured radiative lifetime τ_0. In the inset a zoom of low t_{avg} values.

Fig. 3.17 (upper panel) present the evolution of t_{avg} with the number of excited electron-hole pairs for individual DRs from thin shell DR42 and thick shell DR22. The error bars are due to dispersion of lifetimes from one nanocrystal to another, computed on about 10-15 nanocrystals.

This kind of study underlines the importance of an analysis at the single nanocrystal level, with respect to the usual lifetime ensemble measurements.

In the case of nearly mono-exponential DR42, lifetimes of about 20 ns are regularly measured within the sample. No evolution with the excitation intensity can be put in evidence. Even if off periods become more abundant at high power, their contribution to the decay curve remains negligible because of the low signal coming from the off states.

Non-blinking DR22, on the other hand, show a well evident trend with the excitation power, as it is also evident for a specific nanocrystal shown in Fig. 3.17 c).
t_{avg} decreases with the power because the nanocrystals spend more and more time in the grey state. In fact, the dynamics of the switching between the bright and the grey state is determined by the photo-ionization rate, which grows with increasing $\langle N_{eh} \rangle$ because it is a process mediated by the Auger recombination. The relaxation to the neutral state, on the other hand, is normally associated with tunneling back from trap state to the nanocrystal core, and thus it is almost power independent [81].
t_{avg} at low power coincides most of the time with the longer time constant τ_0, which in turns is a good approximation for the radiative lifetime $1/\gamma_R$, assuming negligible γ_{NR}, as described in the previous paragraph:

$$\lim_{<N_{eh}>\to 0} t_{avg} = \tau_0 \simeq \tau_R$$

The large error bars in Fig. 3.17 b) indicate that DR22 are very dispersed in terms of radiative rates γ_R. This is illustrated in the lower part of Fig. 3.17 (d), where nanocrystals with similar lifetimes are grouped together (different colors). For example, the single nanocrystal studied in Fig. 3.17 c) (called nc07) belongs to the green group, with radiative lifetimes between 100 and 200 ns. More statistics would be necessary to determine if distinct populations of nanocrystals exist or if there is a continuous variation of lifetimes within the sample.
Interestingly, a group of nanocrystals (blue dots in Fig. 3.17 d)) with a short lifetime (about 25 ns) show only slight evolution with the excitation.
Actually, since they show an important grey state in the intensity time-trace, one should expect a similar trend as for the green and the red groups. A careful analysis with the threshold method, described in the previous section and exemplified in Fig. 3.16, reveals a short lifetime $\tau_1 \lesssim 4ns$ whose contribution increases for large $\langle N_{eh} \rangle$. This time constant is partially masked by the fast exponential component τ_F, which is excluded from the computation of t_{avg}. This fact leads to a probable overestimation of t_{avg} at high powers.

A qualitative correlation is found between the radiative lifetime τ_0 and the QY of the grey state $QY_1^{(-1)}$, which can vary between 20 and 60% of the bright state $QY_1^{(0)}$: the longer the radiative lifetime of a DR, the higher its $QY_1^{(-1)}$. This is coherent with a volume scaling of radiative and Auger rates, which roughly go inversely with the electron-hole overlap. However γ_R and γ_A^e can not be in a simple proportionality relation. Indeed if $\gamma_A^e = k\gamma_R$ there would be no variation of $QY_1^{(-1)}$ with γ_R, according to the definition:

$$QY_1^{(-1)} = \frac{2\gamma_R}{2\gamma_R + 2\gamma_A^e} \approx \frac{1}{1+k}$$

DRs with long radiative lifetimes are more sensitive to photo-charging: while at low power they seems to be basically neutral (monoexponential lifetime and quasi-Poissonian emission), increasing the power they go into a charged state more and more easily.
On the contrary, DRs with short lifetimes seem to be more robust with respect to photo-charging. The weight of the bright state is still important at high power.

A similar dispersion of radiative rates has been found for other samples with suppressed blinking like DR21, DR23 and, to a less extent, DR24 and DR26, as illustrated in Fig. 3.18.

Results for all DRs Fig. 3.18 summarizes the results of the lifetime analysis for all the DR samples studied in this thesis.
In details:

- DR76 (core diameter d=1.5-2 nm, shell thickness t=3.6 nm and length L=51 nm) show a behavior close to the already commented DR42 (d=3.3 nm, t=4 nm, L=22 nm). They both blink and their grey state can be considered like an off state, so their decay is nearly mono-exponential: $t_{avg} \simeq \tau_0$ and only slightly decreases with increasing the power. With respect to DR42, DR76 present a much longer radiative lifetime, around 50-60 ns, which is probably due to a different confinement regime of the electron wavefunction.

- DR23 (d=3.3 nm, t=7 nm, L=35 nm) and DR26 (d=3.3 nm, t=7 nm, L=58 nm), are like DR22 (d=3.3 nm, t=7 nm, L=22 nm) but their shell is longer, and their lifetimes t_{avg} are less and less dispersed. DR23 lifetimes are most between 25 and 60 ns. DR26 show the shortest average lifetimes, between 20 and 40 ns. Shorter t_{avg} at low power are due to two factors. First, the radiative lifetime $\tau_0 \simeq \tau_R$ is in average shorter in longer rods and this fact will be discussed better in the following. Second, longer rods like DR26 are more likely to be charged, and then the weight of the grey state lifetime τ_1 in the average lifetime t_{avg} is larger for any exciting power. This fact can be explained by the larger surface-to-volume ratio in DR26 compared to DR23 or DR22, which increases the population of surface trap states.

- DR21 (d=4.2 nm, t=7.5 nm, L=42 nm) have a behavior similar to DR22 (d=3.3 nm, t=7 nm, L=22 nm), except that the decrease in lifetime with excitation is faster (more efficient photo-ionization). Radiative lifetimes are even more dispersed than in DR22, see the error bars of t_{avg} values at low power in Fig. 3.18. Values at high power are missing because the photo-bleaching becomes more and more important, and off states and multi-charged states dominate the measurements, as described in section 3.4 about the photo-stability.

- DR24 (d=4.6 nm, t=11 nm, L=29 nm) show long radiative lifetimes and also t_{avg} is still quite long at high power. $\tau_0 \simeq 100ns$ and $\tau_1 \simeq 25ns$, thus they show the highest grey state quantum yield
$$QY_1^{(-1)} = \frac{2\tau_1}{\tau_0} \simeq 50\%$$
This is due to an efficient suppression of the Auger recombination rates due to very thick shell. This is in agreement with the higher average quantum yield $\langle QY \rangle_t = 0.54$ measured in section 3.2 and reported in the table of Fig. 3.6.

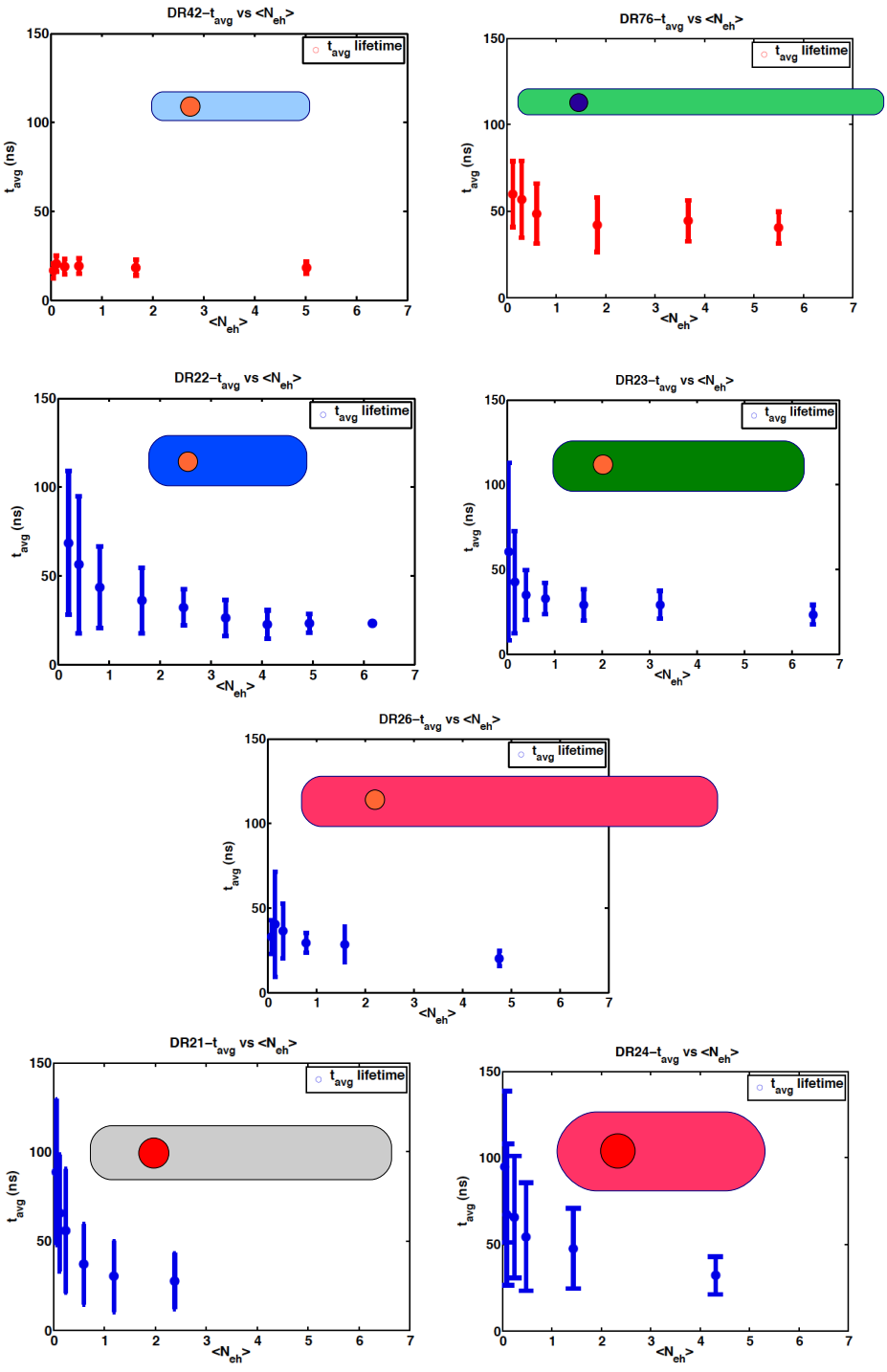

Figure 3.18: Average lifetime t_{avg} as a function of the number of excited electron-hole pairs $\langle N_{eh} \rangle$ for all DR samples. Sketches of the DRs shape and size are in-scale.

Discussion First of all we want to discuss the reasons for the dispersion of radiative lifetimes observed for some of the samples.

As we described in section 2.1.3 there is a connection between the electron wavefunction delocalization and the lifetime, since γ_R is proportional to the electron-hole wavefunction overlap P_{eh}. This fact has been confirmed by measuring the PL spectra on single nanocrystals.
Fig. 3.19 shows an example for two nanocrystals from sample DR23, measured at low power, so that $t_{avg} \simeq \tau_R$. A red-shift of the PL spectrum correlates with a longer lifetime. These observations are coherent with the model of quasi-type II nanostructures discussed in the first chapter: the more localized the wavefunction the larger the effect of the quantum confinement on the energy levels, leading to an increase of the band-edege exciton emission energy. On the contrary, a higher delocalization of the electron into the shell leads to a red-shift of the PL spectra.

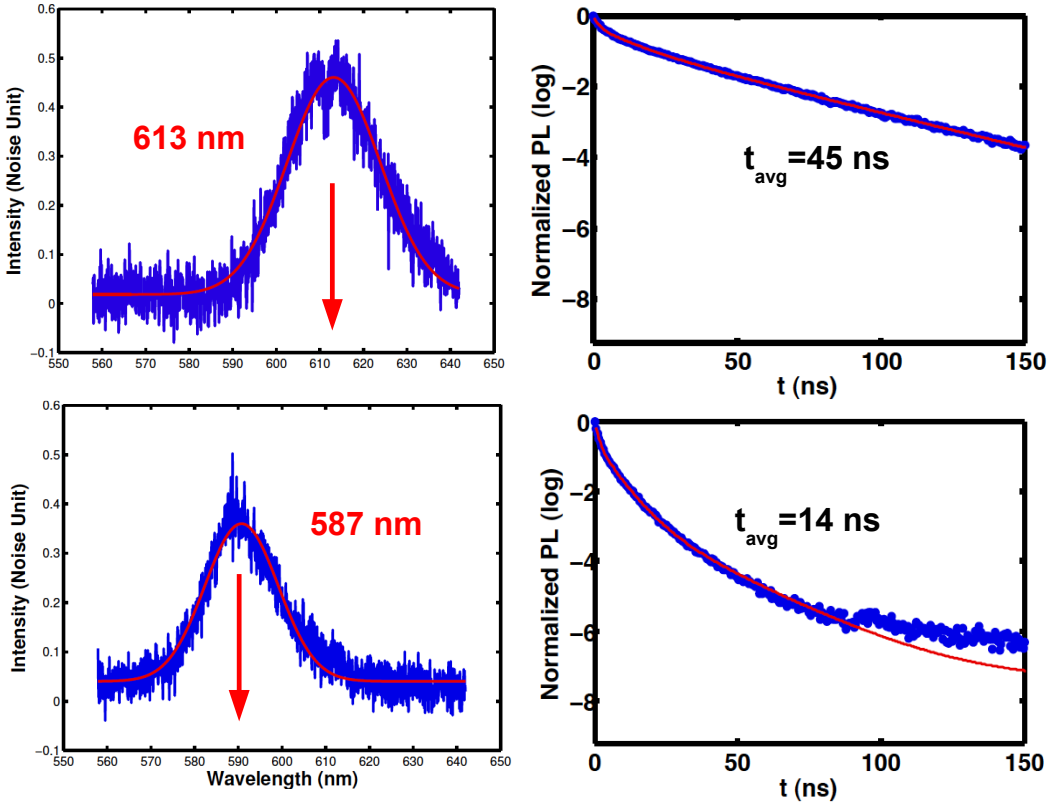

Figure 3.19: PL spectra for two single nanocrystals from sample DR23. The first (up) has long lifetime and a red-shift spectrum (with respect to the ensemble value). The second one (down) is blue-shifted and shows a lower lifetime as well.

In order to understand the behavior of lifetimes in different CdSe/CdS DR nano-structures and within a certain sample of DRs, we can make some speculations about the electronic wave-function.

We can interpret the observed behavior of the exciton lifetime in different geometries of DRs by assuming a quasi-type II band alignment in CdSe/CdS nanocrystals, as we widely discussed in chapter 1. In a quasi-type II band alignment the valence band offset is quite large, while the conduction band offset is nearly zero. Therefore the hole wavefunction is always well confined into the core, while the electron wavefunction can be delocalized more into the core or into the shell, causing a continuous transition from a prevalently type I (both the electron and the hole localized into the core) to a prevalently type II regime. In the type I localization, the radiative lifetime is shorter because the electron-hole overlap integral P_{eh} is closer to 1.

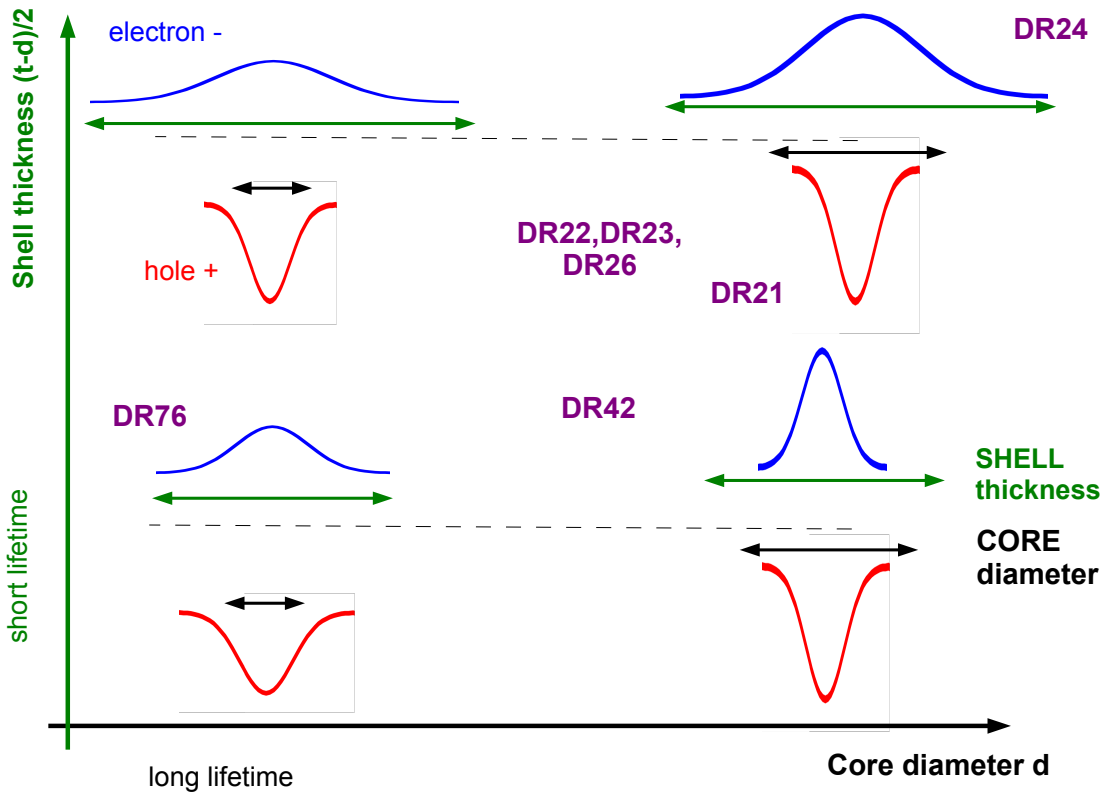

Figure 3.20: A picture of the expected electron and hole wavefuntion localization as a function of the core diameter (x-axis, black) and of the shell thickness (y-axis, green). In magenta the position of the studied DRs in this 2D plot, according to their geometrical parameters.

The core size is thought to be essential in determining the electron delocalization and a transition from type II to type I heterostructure was observed in DRs for a diameter $d > 2.7nm$ [46]. However, in [46] only thin shell DRs were considered.

We can make the hypothesis that a transition from a type II to a type I wavefunction localization depends at the same extent on the core size and on the shell thickness. A thick shell and a small core foster a transition to quasi-type II alignment. This model is schematized in Fig. 3.20.

The shell length, on the other hand, would give a second order effect. Thin shell DR42 (shell thickness is $(t-d)/2 = 0.4$ nm) and DR76 ($(t-d)/2 = 0.9$ nm) are respectively examples of type I and type II localization: the lifetime is short in DR42 (core diameter d=3.3 nm) and long in DR76 (d=1.5-2 nm).

Very thick shell DR24 ($(t-d)/2 = 3.2$ nm) should be type I because of their large core (d=4.6 nm). However their lifetime is long because of the shell thickness, and thus the electron wavefunction can be more delocalized, as illustrated in Fig. 3.20. Also the formation of an alloy at the core/shell interface and the consequent smoothing of the confinment potential can promote the electron delocalization [44].

DR22 (d=3.3 nm), DR23 (d=3.3 nm), DR26 (d=3.3 nm) and DR21(d=4.2 nm) are intermediate cases, where slight differences from one single nanocrystal to another, in the shell thickness ($(t-d)/2 \simeq 1.8$ nm) or equivalently in the core diameter, can determine the prevalent type I or type II character. This would explain the large dispersion both in terms of radiative lifetimes and spectra observed before.

In addition to the precise core size and shell thickness, other factors could contribute to the electron delocalization and to the lifetime, especially for some of the very long lifetimes ($t_{avg} > 150$ ns) observed in DR22 and DR21. We have already mentioned a core/shell alloying process, which, according to [44], should begin at a critical thickness of $\simeq 2$ nm. Morevoer in [38] the authors found that an arrow-shaped shell can completely modify the optical properties: these kinds of morphological differences are a random outcome of the synthesis process and can not be controlled.

The behavior of DR23 and DR26 demonstrate that increasing the length, surprisingly, can push towards a type I localization and to less dispersed lifetimes. Anyway it should be kept in mind that this fact occurs for a core diameter (d=3.3 nm) which is probably at the border between type I and type II structures. In fact, very small core DR76 are for sure type II structures, besides the very long shell.

The localizing effect of the shell length can be assigned, for instance, to a slight change of the conduction band offset or to a band bending effect induced by an internal electric field, associated with larger surface charges, as described in chapter 1.

All these considerations assume that the radiative lifetimes are not strongly influenced by the electronic fine structure, according to recent cryogenic measurements on DRs [42] [43]. This is not necessarily true in thick shell DRs, where cryogenic measurements have never been performed. Low temperature lifetime and spectral studies will be necessary to confirm or disprove some of the proposed interpretations.

3.6 Auto-correlation Function measurements

In this section I will present our experimental results about the intensity auto-correlation function $g^{(2)}(0)$ measured on different kinds of DRs as a function of the excitation power.

We will see that $g^{(2)}(0)$ in suppressed-blinking DRs is dominated by the contribution of grey states: the higher the weight of the grey state, the higher the probability to emit multi-photons. We demontrate that the behavior of $g^{(2)}(0)$ as a function of the excitation power can be well reproduced by evaluating the relative weights of bright and grey states. For instance: a nanocrystal which at low power is prevalently in the bright state shows a very low $g^{(2)}(0)$, which fast increases because the grey state becomes more and more important. A nanocrystal in which the proportion between bright and grey states does not depend much on the power will show a higher $g^{(2)}(0)$ at low power, but a more flat behavior. The same holds for thin-shell, blinking DRs like DR42 or DR76, where the bright state is always dominant because the grey states are almost off states.

As we found before, a grey state can be characterized either by its PL intensity or by its lifetime. Because of the fast time-scale of the intensity fluctuations, it is difficult to set a threshold to select only the grey states and to assess directly their intensity quantum yield $QY_1^{(-1)}$.

In the previous section we showed that the PL lifetimes are a good tool for studying the dynamics of grey states as a function of the excitation power. Therefore we will study $g^{(2)}(0)$ as function of the lifetime. We will develop a theoretical model in order to interpret the correlations found and, in particular, to explain the behavior of $g^{(2)}(0)$ as a function of the excitation power in different DRs.

We will see that low values of $g^{(2)}(0)$ are not only determined by high Auger rates, but also by the ratio between the radiative and the Auger rate: nanocrystals with longer lifetime can easily reach low $g^{(2)}(0)$ values even if the Auger rate is not very efficient.

Because of the dispersion of the radiative lifetimes found within certain samples of DRs in the previous section, a similar dispersion is expected also for the Auger rates, and thus DRs will be analyzed one by one. A sample with low dispersion would be preferable for practical applications, such the implementation of a single-photon source.

Our approach is original and it is not restricted to the study of CdSe/CdS DRs and it could be extended, in principle, to all kinds of nanocrystals, especially those with suppressed blinking.

3.6.1 Auto-correlation Function and grey states

As in the section about lifetimes we start with a simple, qualitative analysis of the auto-correlation function for bright and grey states.

In Fig. 3.21 a) a nanocrystal from DR22 sample is excited at $\langle N_{eh} \rangle \simeq 2$ and coincident counts between the two APDs are collected for 20 s with a time resolution of 2 ns. $g^{(2)}(0)$, as derived in chapter 2, is calculated by taking the ratio between the central peak at delay $\tau = 0$ and the average of the first 4 side peaks. The areas are computed on an interval of $100ns$ around the peaks.

We perform a selection of photons from the PL timetrace of a single DR with a low and a high threshold, like for the lifetime. In Fig. 3.21 b) it is evident that $g^{(2)}(0)$ is much lower for

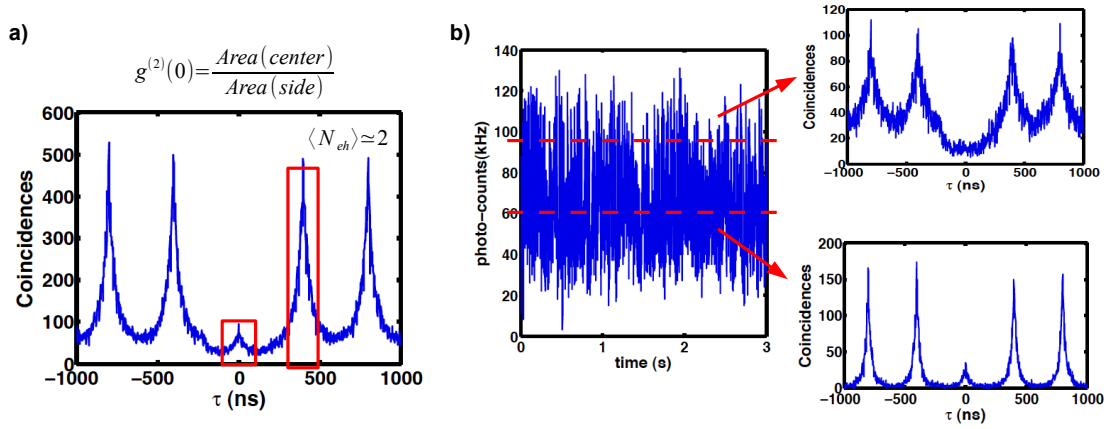

Figure 3.21: a) Sketch of the procedure for a $g^{(2)}(0)$ measurement. $g^{(2)}(0)$ is calculated from the histogram of coincident counts, by taking the ratio between the area of the central peak and that of the side peaks. b) $g^{(2)}(0)$ for a selection of photon counts from the PL time-trace. The zero peak is lower for photons coming from the bright state.

the bright state than for the grey state. This is correlated with a shorter average lifetime.
Higher $g^{(2)}(0)$ values for nanocrystals in a grey state, characterized by low intensity and short lifetime, has already been observed in spherical CdSe/CdS nanoparticles, for example in [129], but, up to our knowledge, this effect has never been investigated in detail.
Similar results are found for every kinds of DRs studied in this thesis, except for samples with a really mono-exponential lifetime (no grey states).

Since the grey state is characterized by its lifetime and since there is a clear trend of the average lifetime with the power, as it is evident in Fig. 3.17, we will study the evolution of $g^{(2)}(0)$ with the excitation power.
If the hypothesis of a correlation between $g^{(2)}(0)$ and the grey state (and thus the lifetime) is correct, we expect that the trend of the auto-correlation function should follow closely the evolution of lifetime. Of course, as we already explained in section 2.4.3, $g^{(2)}(0)$ increases with $\langle N_{eh}\rangle$ also because of the increasing contribution of higher order multi-excitons [75] [105], according to the general expression derived in eq. 2.5. However, as we will see, the behavior up to $\langle N_{eh}\rangle = 3-4$ is well described by the increasing presence of grey states, whereas it could not be explained by the multi-excitonic contribution alone.

3.6.2 Theoretical model

First of all we need a theoretical model in order to make a prevision about the expected correlations between $g^{(2)}(0)$ and the grey state.
We start from the relation between $g^{(2)}(0)$ and quantum yield in nanocrystals, developed in

[105] and completely derived in chapter 2:

$$g^2(0) \approx \frac{\langle QY_2 \rangle_t}{\langle QY_1 \rangle_t} \; for \; N_{eh} \to 0 \tag{3.6}$$

where the QYs for the exciton and the bi-exciton are time-averaged over the bright and the grey states.

The quantum yield for a band-edge state configuration of n_e electrons and n_h holes can be calculated explicitly from the definition of QY_m in eq. 2.2, where m is a shortcut for the total number of electron-hole pairs:

$$QY_m = \frac{n_e n_h \gamma_R}{\gamma_i(n_e, n_h)}$$

The denominator is the measured decay rate, i.e the sum of radiative and non-radiative decay rates, which can be written explicitly using the statistical scaling in eq. 2.1:

$$\gamma_i(n_e, n_h) = n_e n_h \gamma_R + n_e n_h \gamma_{NR} + n_e n_h (n_e - 1)\gamma_A^e + n_e n_h (n_h - 1)\gamma_A^h \tag{3.7}$$

We will use the same notation introduced for the quantum yields of the neutral and the charged exciton $QY_m^{(-i)}$: the subscript m denote the number of electron-hole pairs and the superscript i indicates the sign and the number of the additional charge of the grey state (typically one electron).

Since the bi-exciton lifetime are too short to be experimentally accessible, $\langle QY_2 \rangle_t$ must be estimated by using the statistical scaling of radiative and non-radiative decay rates introduced in eq. 2.1. Thus we have:

$$QY_2^{(0)} = \frac{4\gamma_R}{4\gamma_R + 4\gamma_A^e + 4\gamma_A^h}$$

for the neutral bright state and

$$QY_2^{(-1)} = \frac{6\gamma_R}{6\gamma_R + 12\gamma_A^e + 6\gamma_A^h}$$

for the negatively charged, grey state.

As already mentioned, we assume that other non-radiative decay channels different from Auger are negligible, i.e. $\gamma_{NR} \ll \gamma_R$, because the single exciton quantum yield of the bright state $QY_1^{(0)} \approx 1$, as deduced from measurements of the maximal quantum yield QY_{max} (see section 3.2). The time-average quantum yield of the exciton $\langle QY_1 \rangle_t$ is expressed in terms of measured rates for the bright state $\gamma_0 = 1/\tau_0$ and for the grey state $\gamma_1 = 1/\tau_1$ extracted from the bi-exponential fits described in section 3.5.1:

$$QY_1^{(0)} = \frac{\gamma_R}{\gamma_0} \approx 1$$

and

$$QY_1^{(-1)} = \frac{2\gamma_R}{\gamma_1}$$

The time-averaged values are computed by considering the time spent in the bright and in the grey state, which is given by the photon weights $p_{0,1} = a_{0,1}\tau_{0,1}$ extracted from the lifetime

fit and already used for calculating t_{avg} in eq. 3.5.
The average exciton QY is thus given by:

$$\langle QY_1 \rangle_t = p_0 QY_1^{(0)} + p_1 QY_1^{(-1)} = \gamma_R (p_0 \tau_0 + 2 p_1 \tau_1) = \gamma_R t_b$$

We can thus define another average time t_b as:

$$t_b = p_0 \tau_0 + 2 p_1 \tau_1$$

which is only slightly different from t_{avg}. As we have already observed for t_{avg}, also t_b is robust with respect to the fitting procedure. Provided that the residuals of the fit are small, the values of t_b only slightly depends on the specific values of the weights $p_{0,1}$ and of the time constants $\tau_{0,1}$ found from the fit of $L_{PL}(t)$.

In the same way the average bi-exciton $\langle QY_2 \rangle_t$ can be calculated. Now we will do some approximations which allow to derive a simple expression for $g^{(2)}(0)$ as a function of the measured lifetime. We will see in the following that this approximation is not strictly necessary, but it is very useful to give an intuitive picture of the important physical processes.

Since the measured values for $g^{(2)}(0)$ at low power are quite low for all samples, from less than 0.1 to 0.3 at most, γ_A^h or γ_A^e must be larger than γ_R.
Moreover, since the grey state is quite bright ($20\% < QY_1^{(-1)} < 60\%$) and it is normally assigned to a negatively charged nanocrystal [93] [67] [94] [81], it means that the Auger recombination of the negative trion γ_A^e is of the same order of γ_R. This implies that the Auger recombination of the positive trion is the main responsible for the bi-exciton prevalent non-radiative recombination, and thus $\gamma_A^h \gg \gamma_A^e \approx \gamma_R$.
By neglecting γ_A^e and γ_R in the denominator of QY_2, the time averaged bi-exciton QY becomes simply:

$$\langle QY_2 \rangle_t = (p_0 + p_1) \frac{\gamma_R}{\gamma_A^h} = \frac{\gamma_R}{\gamma_A^h}$$

which means that the bi-exciton QY does not depend on the state of charge within this approximation.
The auto-correlation from eq. 3.6 can be finally calculated:

$$g^{(2)}(0) \simeq \frac{\langle QY_2 \rangle_t}{\langle QY_1 \rangle_t} \simeq \frac{1}{\gamma_A^h t_b} = \tau_A^h \gamma \tag{3.8}$$

where $\gamma = 1/t_b$ for convenience. A basic Auger lifetime $\tau_A^h = 1/\gamma_A^h$ for the positive trion can thus be deduced from $g^{(2)}(0)$ measurements at low excitation power as a function of the lifetime. This allows for a direct comparison of the different kinds of DRs which has been studied up to now in terms of Auger suppression.

The expected bi-exciton lifetime $t_{avg}^{(2)}$ is a time average between the neutral and the charged state. Always assuming $\gamma_R, \gamma_{NR}, \gamma_A^e \ll \gamma_A^h$, $t_{avg}^{(2)}$ can be estimated by applying eq. 3.7:

$$t_{avg}^{(2)} = p_0 \frac{1}{4\gamma_A^h} + p_1 \frac{1}{6\gamma_A^h}$$

As a first approximation it should be between 1/4 and 1/6 of τ_A^h.

Eq. 3.8 tell us that the single photon emission depends on the ratio between the rate γ and the Auger rate. In fact, $g^{(2)}(0)$ can be very small if γ is very small, i.e. if the lifetime is very long, even if the Auger rate is quite small. Small γ are measured if the weight of the bright state p_0 is large, or if the radiative lifetime $\tau_R \simeq \tau_0$ is long.
Moreover, according to eq. 3.8, the performance of a nanocrystal as a single photon emitter must be evaluated also in terms of its tendency to be charged and to get charged by photo-ionization.

Let's now consider some issues and consequences of our theoretical model.
The main assumption for this formula is that $\langle QY_2 \rangle_t$ does not change much whenever the nanocrystal is in the bright or in the grey state. In our approximation this is because the supplementary charge is always an electron and $\langle QY_2 \rangle_t$ only depends on the efficiency of the Auger recombination of positive trions γ_A^h. Anyway, we can also suppose that $\gamma_A^e \approx \gamma_A^h \gg \gamma_R$. In this general case we would obtain:

$$\langle QY_2 \rangle_t = p_0 QY_2^0 + p_1 QY_2^{-1} \simeq \gamma_R \left(\frac{p_0}{\gamma_A^e + \gamma_A^h} + \frac{p_1}{2\gamma_A^e + \gamma_A^h}\right)$$

In the worst case, if $\gamma_A^e \simeq \gamma_A^h = \gamma_A$, QY_2 can change from a maximum value $\gamma_R/2\gamma_A$ (only bright state) to the minimum $\gamma_R/3\gamma_A$ (only grey state), i.e. a 30% variation. QY_1, on the other hand, can change from 1 to 0.2-0.5 that is a factor 2-5.
This is really the worst case. Considering also the contributions of γ_R and γ_{NR} would lead to even smaller variations.
It should be considered that, in a general case, the value τ_A^h in eq. 3.8 is actually given by the sum of positive and negative Auger rates.

Another important assumption of this model is that eq. 3.8 is supposed to hold only for low excitation power, i.e. for $\langle N_{eh} \rangle \to 0$. The physical meaning of this approximation is that multi-order excitons are negligible at low power with respect to bi-excitons, as described in chapter 2. We will see in the next section that our model of eq. 3.8 can reproduce the behavior of $g^{(2)}(0)$ as a function of the lifetime until $\langle N_{eh} \rangle \lessapprox 3$. $g^{(2)}(0)$ as a function of $\langle N_{eh} \rangle$ follows the behavior of t_b (and of t_{avg} as well) for values well above the saturation power, even if the deviation becomes more and more important for high powers. The conclusion is that the behavior of $g^{(2)}(0)$ with the excitation power in nanocrystals with non negligible grey states is dominated by the dynamics of photo-ionization, and that the multi-excitonic contribution should be a second order correction.

Results Fig. 3.22 shows an example of correlations between $g^{(2)}(0)$ and lifetime for the sample DR22. DR22 are taken as an example because they are quite dispersed in terms of lifetime, which allows us to describe different cases. A similar analysis has been performed for all DRs and a summary of the final results will be given in the following section.
12 single DRs are studied at several excitation powers and grouped together, like for lifetime measurements, according to their radiative lifetime: the green ones show the longer lifetime, 100-150 ns, the red ones range between 40 and 60 ns and the blue ones are around 25 ns.
Higher $\gamma = 1/t_b$ correspond to higher $g^{(2)}(0)$. This is true at low excitation (Fig. 3.22 left), but it is even more evident by considering $\langle N_{eh} \rangle$ up to 6 (Fig. 3.22 right).
The slope of the linear fit gives directly the value of τ_A^h which is indicated on the plots for the

different groups of nanocrystals.
Different τ_A^h values for different radiative lifetimes are not surprising, since Auger rates were found to scale with the volume of the exciton [51] and the radiative lifetime is proportional to the spatial electron-hole wavefunctions overlap P_{eh}. Thus $\gamma_A^{h,e}$ and γ_R both depend on the electron delocalization.

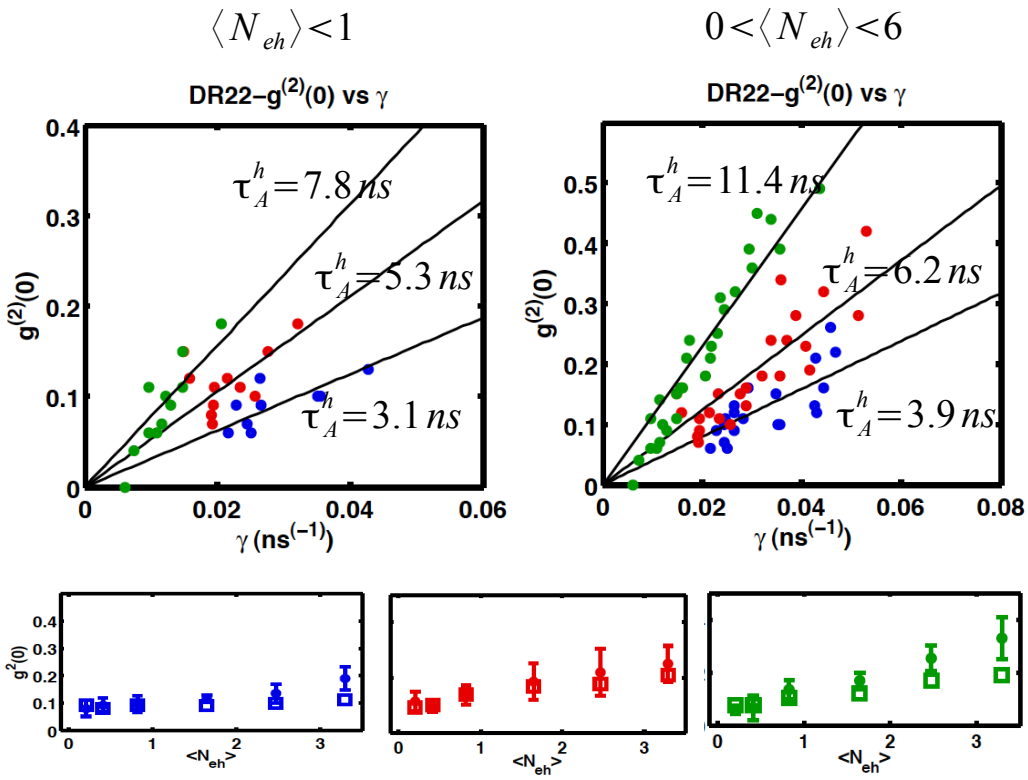

Figure 3.22: $g^{(2)}(0)$ plots as a function of $\gamma = 1/t_b$ for several DRs from sample DR22 and different excitation powers. On the left only low powers are considered while on the right all excitations up to $\langle N_{eh} \rangle \approx 6$ are considered. The data are fitted by the linear relation predicted by eq. 3.8 and the coefficient τ_A^h found from the fit is reported. Different colors correspond to different nanocrystals. In the lower panel, the measured $g^{(2)}(0)$ as a function of power (circles) is plotted together with the values (squares) calculated from eq. 3.8 using the values τ_A^h found above ($N_{eh} < 1$).

By using the values of τ_A^h found in the fit, the evolution of $g^{(2)}(0)$ with the excitation intensity can be well reproduced, as illustrated in the lower part of Fig. 3.22. The blue group (small lifetime) presents a slow increasing of $g^{(2)}(0)$ with $\langle N_{eh} \rangle$, coherently with the slow variation of the average lifetime observed in Fig. 3.17 d). The opposite situation occurs for the green group, where the variation of lifetime with the power is very important, and so it is the probability to

emit more than one photon.

Of course there is a deviation of the measured $g^{(2)}(0)$ values from the predicted ones, which is more and more important at high excitation intensities. This is due, as we already remarked, to the contribution of the high order multi-exciton emission which is neglected in our model. The evolution of $g^{(2)}(0)$ as a function of $\langle N_{eh} \rangle$ is given by eq. 2.5, where QY_m can be calculated from QY_1 and QY_2, using the statistical scaling of radiative and Auger rates as illustrated in section 2.4.3.
This was calculated in [105], finding that for $\langle N_{eh} \rangle \simeq 10$, $g^{(2)}(0)$ should saturate to a value of less than two times its value for $N_{eh} \to 0$. This calculated growth cannot explain the evolution of $g^{(2)}(0)$ for the red and the green groups of nanocrystals in Fig. 3.22, but it is consistent with the slow evolution of the blue group, where the lifetime is almost constant for increasing powers.

The evolution of $g^{(2)}(0)$ can thus be interpreted in terms of grey states and radiative lifetimes. Nanocrystals with long lifetime (green group) have a longer τ_A^h and thus a less efficient Auger effect. At low excitation power they have a low $g^{(2)}(0)$, because they are almost always in the bright state, which has a very long lifetime, $\tau_0 \gg \tau_A^h$, and thus the product $\tau_A^h \gamma$ in eq. 3.8 can also be very low. On the other side, as the power increases and the grey state becomes more and more important, $g^{(2)}(0)$ quickly increases as well.
In nanocrystals with short lifetimes (blue group) τ_A^h is shorter and the weights of the grey and of the bright state depend less on $\langle N_{eh} \rangle$. This implies a flatter behavior of t_b and, as a consequence, of $g^{(2)}(0)$.

Fig. 3.23 shows the trend of $g^{(2)}(0)$ as a function of $\langle N_{eh} \rangle$ for all studied DRs (blue circles). Measurements are performed on a sample of 10-15 nanocrystal for each kind of DR and error bars are mainly due to the dispersion of spectral and lifetime behavior within the sample, as widely discussed in the previous paragraph for the example of DR22.
Red squares are the product $\tau_A^h \gamma$, according to eq. 3.8, where τ_A^h is derived by fitting the $g^{(2)}(0)$ data for all nanocrystals at all powers as a function of $\gamma = 1/t_b$, like in Fig. 3.22.

These curves can be compared directly with the evolution of the average lifetime t_{avg}, illustrated in Fig. 3.18. It is evident that $g^{(2)}(0)$ follows closely the evolution of the lifetime for all kinds of DRs. This is true also for thin-shell and blinking DR42 and DR76, where the lifetime does not change much with the power, and for DR24, which show higher $g^{(2)}(0)$. This fact confirms the general validity of our model.

An important result of these measurements is that both the Auger and the radiative lifetime contribute to the final single photon emission quality. This is evident by comparing DR42 and DR76. DR42 show the lowest τ_A^h but not the lowest $g^{(2)}(0)$. Indeed the radiative lifetime in DR42 is $\tau_0 \simeq 1/\gamma_R \approx 15 - 20ns$, while it is $\tau_0 \simeq 1/\gamma_R \approx 50 - 60ns$ in DR76. Therefore their auto-correlation at low power is comparable or even lower for DR76 since $g^{(2)}(0) \simeq \tau_A^h / t_b$. On the other hand, as already mentioned for DR22 in Fig. 3.22, γ_A^h and γ_R are not independent.

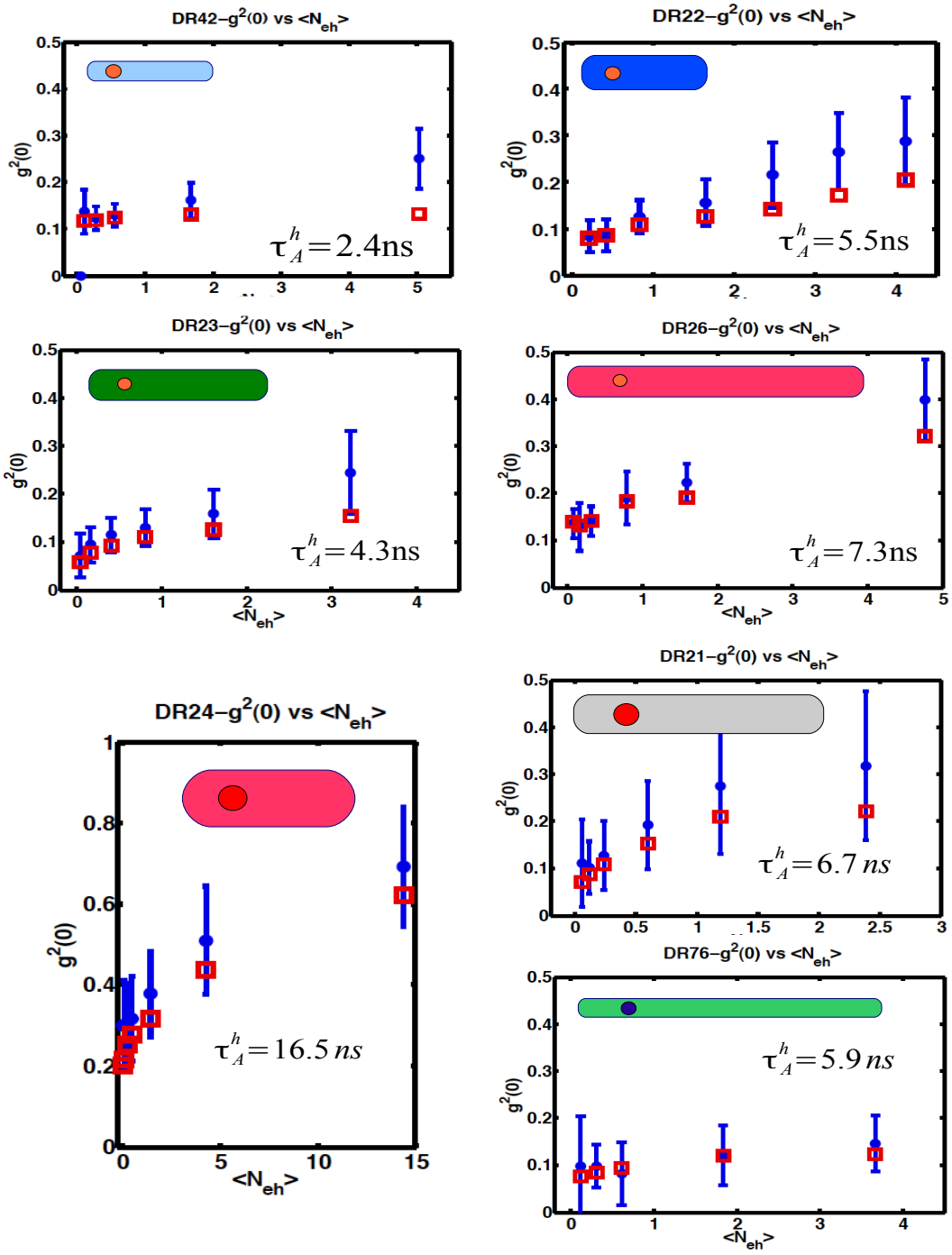

Figure 3.23: $g^{(2)}(0)$ measured on a sample of 10-15 single DRs (blue points), as a function of the number of excitated electron-hole pairs $\langle N_{eh} \rangle$, and our prediction based on eq. 3.8 (red squares).

Even if the Auger rate is correlated with the radiative lifetime, probably they are not proportional. For instance, long shell DR26 in Fig. 3.23 show a higher Auger τ_A^h then DR22 and

DR23 even if, as we already observed, they are characterized by a lower lifetime, see Fig. 3.18. Another example is provided by DR24, which have an Auger time much longer than all the other samples, but a lifetime comparable to DR22 or even DR76.
As we discussed in chapter 2, the Auger effect can be efficiently suppressed by the formation of an alloy layer of CdSeS at the core/shell interface. This process starts to take place for a shell thickness of about 4 mono-layers ($\approx$ 2 nm) according to [82].
The shell thickness is $(t-d)/2 = 3.2$ nm in DR24, 1.9 nm in DR22, DR23 and DR26, 1.7 nm in DR21, 0.8-1 nm in DR76 and 0.4 nm in DR42.
The values of τ_A^h found in Fig. 3.23 shown an evident increase with the shell thickness: $\tau_A^h = 2.4$ ns for DR42 which have the thinnest shell and $\tau_A^h = 16.5$ ns for DR24 which have the thickest shell.
This dependence on the shell thickness was already observed also for the Auger rate of the negative trion, which controls the efficieny of the grey state.

In conlusion, the shell thickness seems to be the dominant factor which determines the efficiency of the Auger effect.
In order to develop a single photon source it is necessary to find a balance between blinking suppression and single photon emission, i.e. between γ_A^e and γ_A^h.

According to Fig. 3.23 DR23 seem to be, among the studied samples, the best compromise for the practical implementation as a single photon source. They combine the lowest τ_A^h among thick shell, non-blinking DRs with a lifetime lower than DR22 and these properties are quite uniform within the sample. Moreover, as we will see in the next section, DR23 also have interesting polarization properties.

3.7 Polarization properties of dot-in-rods

One of the main difference between CdSe/CdS dot-in-rods and spherical particles is that DRs show a linearly polarized emission [40] [17].

The polarization of a single photon emitted by atoms, molecules or quantum dots- depends on the specific character of the dipole transition coupled to the electromagnetic field. As we discussed in chapter 1, a π transition gives rise to linearly polarized fluorescence photons. This is called a 1D transition, or linear dipole. In a macroscopic picture this corresponds to charges which oscillate along a well defined axis, also called the brigth axis. It is the common situation in CdSe nano-rods, even if in this case no single photons are usually emitted [27]. An oscillating dipole can also have a bi-dimensional character, in the sense that the charges oscillate in a specific plane. This is called a 2D, or degenerated dipole, and a 'dark axis' is usually defined, orthogonal to the plane where the dipoles lie.
In 1999 Empedocles [15] determined that the structure of the fundamental transition in spherical CdSe nanocrystal at 10 K is basically 2D. In 1996 Efros [24] had already suggested that nanocrystals should have a fundamental transition made of incoherent σ_+ and σ_- transitions, orthogonal to the crystal symmetry axis (c-axis). However at room temperature, most spherical nanocrystals (which are never really symmetric, but elliptical) show more likely a mixed 2D-1D behavior, with 2D prevalence. The degree of 1D component depends on the relative population of the π transition, which is normally at higher energy within the band-edge levels, and so less populated. CdSe/CdS dot-in-rods, on the other side, have shown a dominant 1D component, as suggested by ensemble polarization measurements [40] [16]. Measurements on single CdSe nano-rods [27] and on nano rod-in-rods [50] revealed a sharp transition from a not polarized 2D dipole emission to a linearly polarized emission for a critical aspect ratio of 1.5-2. Since it was correlated with a change also in the Stokes shift, it was attributed to a swapping of the levels of the CdSe fine structure.

In this section we will describe polarization measurements on single DRs with different geometrical parameters. A defocused microscopy technique will be used in order to determine the orientation of the dipole on the substrate. We will see that most of the DRs show a high degree of linear polarization. Differences among the samples are mainly attributed to the electronic fine structure and thus to the core size. A correlation between polarization and lifetime is also found, suggesting that the electron wavefunction localization (type I or type II) also influences the degree of linear polarization of the PL.

Experimental procedure First of all single DRs are identified by means of a preliminary $g^{(2)}(0)$ measurement in a Hanbury-Brown Twiss configuration. If $g^{(2)}(0) < 0.2$, the polarization analysis is performed by collecting the PL from both the photodiodes.

Polarization measurements are realized with a linear polarizer made of a Half Wave Plate (HWP) and a polarizing beam splitter (PBS) working in a large spectrum of 400-800 nm. For each DR, HWP is turned of $\theta_{HWP} = [0, 90°]$ at constant speed by means of a motorized stage. The PL electric field E undergoes a rotation of two times the angle $\Delta\theta$ between its direction and the fast axis of the HWP, as sketched in Fig. 3.24 a). The PBS therefore selects only one

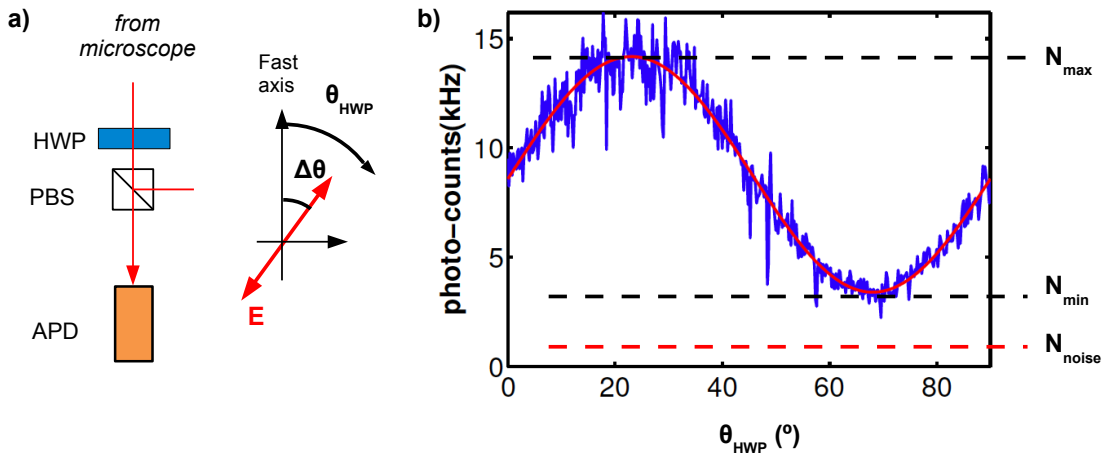

Figure 3.24: a) Setup for linear polarization analysis on the PL from a single DR. One single DR is excited and its emission is collected by a confocal microscope. An half-wave plate (HWP) coupled to a polarizing beam splitter (PBS) work as a polarization analyzer: the HWP is rotated by an angle θ_{HWP}, changing the electric field E direction by $2\Delta\theta$, while the PBS transmits only the horizontal component. b) A typical polarization measurement: in blue the signal detected from the APD while rotating the HWP, in red the fit according to eq. 3.9.

polarization component (the vertical direction). This system allows to scan one complete period (180°), as illustrated in Fig. 3.24 b) for one singe nanocrystal. The resulting curve is thus fitted by the function:

$$N(\theta) = N_0 \left(p \cos^2(\theta_{HWP} + \theta_0) + \frac{1-p}{2} \right) + N_{noise} \tag{3.9}$$

This is just the Malus law for a partially polarized beam, whose *degree of polarization* p is given by:

$$p = \frac{N_{max} - N_{min}}{N_{max} + N_{min} - 2N_{noise}}$$

$p = 1$ for a completely linearly polarized beam. The measured degree of polarization depends on the intrinsic properties of the emitter, but also on other observational parameters, especially the angle between the dipole axis and the optical axis of the objective, and the objective numerical aperture NA.
For a perfect 1D dipole, p can range from 1 for the dipole axis parallel to the substrate (and so perpendicular to the microscope optical axis) to 0 for the dipole axis perpendicular to the substrate.

3.7.1 Defocused microscopy

In order to estimate the position of the DRs on the glass coverslip, we use a defocused imaging technique, sketched in Fig. 3.25 a).

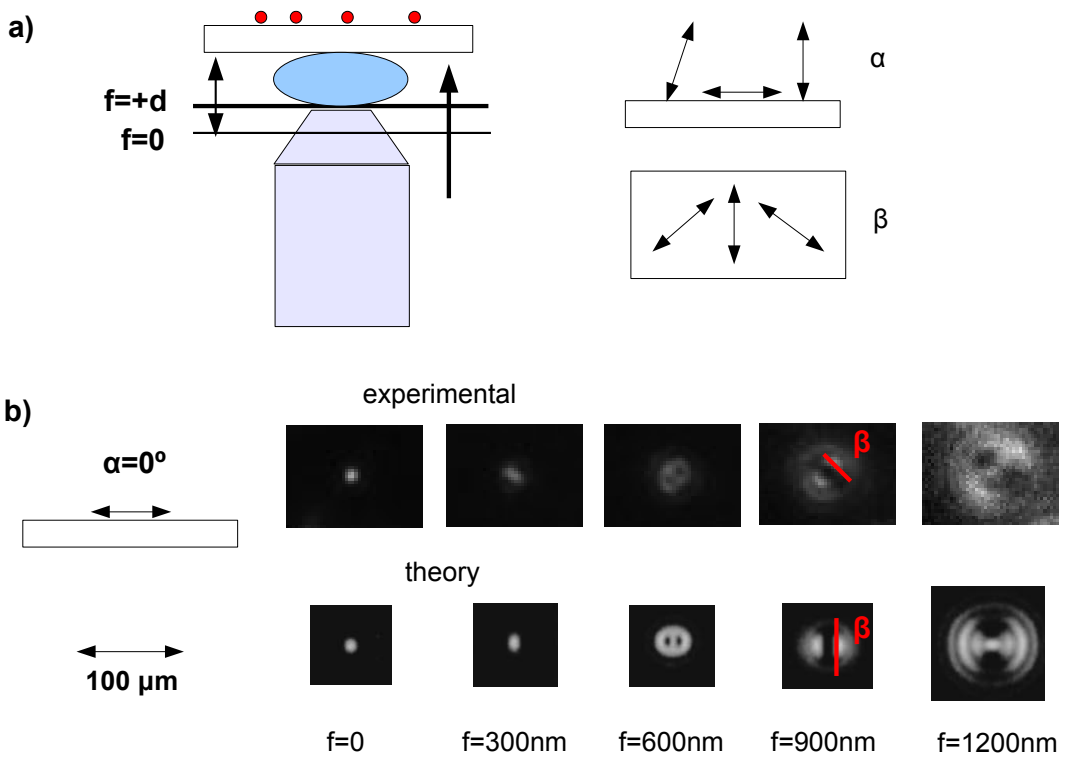

Figure 3.25: a) Defocused microscopy technique for studying the orientation of the DRs on the coverslip surface: an oil immersion objective is moved from the focal distance $f = 0$ towards the sample $f = +d$, and the sample is imaged on a CCD camera. The orientation of the dipole axis on the substrate is defined by two angles α and β. b) The case of a dipole parallel to the surface ($\alpha = 0$): images of a single DR at several defocusing distances f (up) show a good consistency with the theoretical prevision for a 1D dipole [130].

This microscopy technique consists in measuring the transversal distribution of the radiated emission in an out-of-focus plane. Since the radiation pattern of a dipole is not spatially isotropic, this image can provide information about the spatial orientation of the dipole.
Defocused images are usually realized by moving the objective towards the sample but moving the CCD camera image plane would give the same result.
The expected defocused images for 1D dipoles on an air/glass interface and observed by a NA=1.4 oil objective were calculated by Bohmer [130] as a function of the dipole axis orientation with respect to the substrate (α) and on the substrate plane (β). We found a good agreement with these predictions, as shown in Fig. 3.25 b) for the case of a dipole parallel oriented to the surface ($\alpha = 0$) and for several sample-objective distances.

Fig. 3.26 shows a typical image of the sample in-focus and $600nm$ out of focus. Most of the DRs images correspond to dipoles with their axis lying on the surface. Defocused images allows thus to estimate the azimuthal orientation β of the dipoles on the surface (red lines in figure), which is correlated with the phase θ_0 measured in polarization analysis, see eq. 3.9.

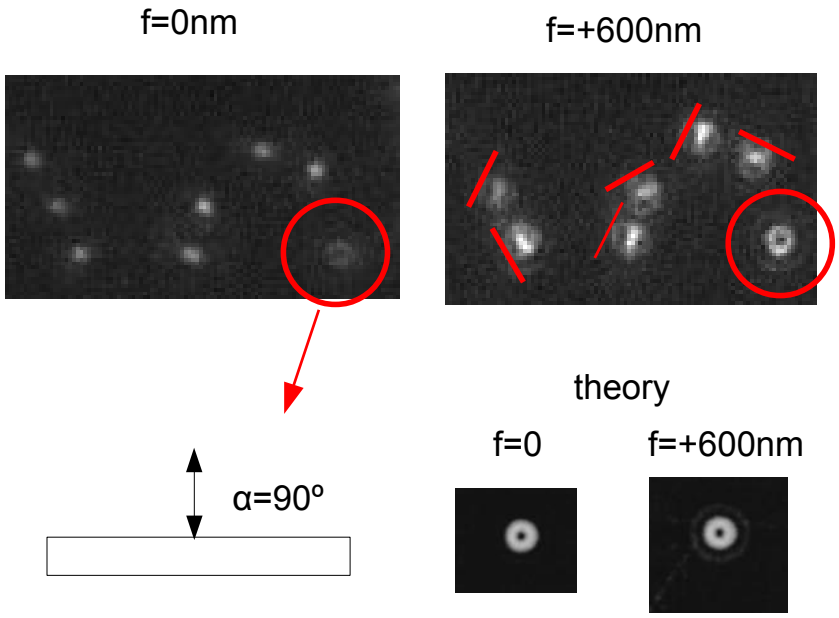

Figure 3.26: A defocused image at $d = +600nm$ allows to assess the orientation of the DRs: the donut shape corresponds to a DR in a vertical position $\alpha = 90°$, as predicted by [130]. Most of the DRs lye on the surface, and the defocused image allows to estimate the orientation β of the dipole axis (red lines).

Sometimes a 'donut' diagram is observed. According to [130], this pattern corresponds to a dipole completely perpendicular to the surface, $\alpha = 90°$as sketched in Fig. 3.26. In this case a degree of polarization $p = 0$ is always measured. The case of DRs oriented with a generic angle α with respect to the surface would give different kinds of defocused images, which are only rarely observed. The conclusion is that DRs, because of their cylindrical symmetry, are more likely to lye down on the surface on the long side of the shell. Sometimes it could be energetically more convenient to lye on the rod minor base, because it is more chemically polar than the side surface, but intermediate situations are not likely. This observation is coherent with previous observations on T.E.M. images [16].

Results and discussion In polarization-resolved single particle measurements, DRs are excited and observed by means of a NA=0.95 air objective. The degree of measured linear polarization indeed decreases with increasing the collection angle of the objective. All measurements are performed with the same objective, which makes them comparable. The absolute value of the polarization could be found back by a proper theoretical model, taking into account both the objective collection and the effect of the air/glass interface [131]

The excitation intensity is kept between $\langle N_{eh} \rangle = 1$ and $\langle N_{eh} \rangle = 2$, in order to maximize the photon counts rate, while keeping a low probability to emit multi-photons. However, we also performed some measurements at higher excitation intensity, and we did not notice any significant variation of the degree of polarization.

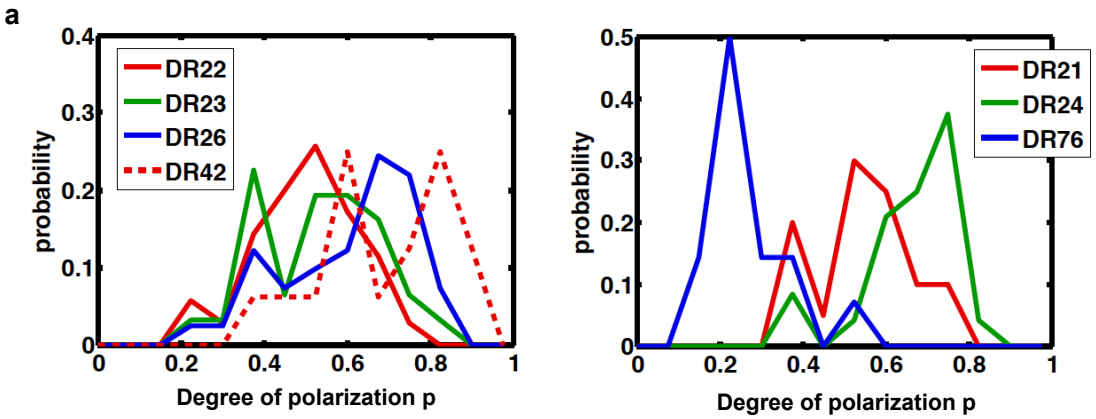

b)

name DR sample	Core Diameter d(nm)	Shell Aspect Ratio (AR)	degree of polarization
DR42	3.3	5.5	**0.69** ± 0.17
DR22	3.3	3.1	**0.5** ± 0.13
DR23	3.3	5.0	**0.53** ± 0.15
DR26	3.3	8.3	**0.6** ± 0.15
DR21	4.2	5.6	**0.55** ± 0.12
DR24	4.6	2.6	**0.66** ± 0.12
DR76	1.5-2	14.2	**0.28** ±0.1

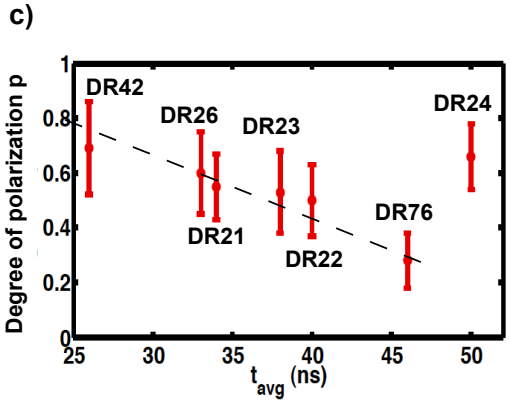

Figure 3.27: a) Distribution of the degree of polarization d measured for about 20 single nanocrystals, for all the DR samples. The large width of the histograms is only pratially due to random errors in the measurement process, while it comes mainly from an intrinsic dispersion of values within a sample. b) A table summarizing the geometrical features of the studied DRs and the measured degree of polarization d. c) Average d plotted as a function of the average lifetime t_{avg}. The dashed line is just a guide for the eyes.

The results of our measurements are summarized in Fig. 3.27. The table summarizes the degree of polarization p measured for each DR sample and averaged on about 20 single nanocrystals.

Fig. 3.27 a) shows the distribution of p values for each sample of DRs. The width of the distribution, expressed by the standard deviation (sigma), is only partially due to random errors associated with the measurement process. There are of course some polarization curves which cannot be well fitted by eq. 3.9. This happens especially for blinking samples like DR42 and

DR76, because the presence of off-periods makes tricky the fitting procedure. However, most of the plots look like the image in Fig. 3.24, where the fit well reproduces the data and p can be estimated with a very good precision.
Therefore the large dispersion of p values found in Fig. 3.27 is most likely associated with an intrinsic dispersion of the degree of polarization within each sample, analogous to what found for the lifetimes, and probably there is a connection between these two observables.

The average degree of polarization shows no evident correlations with the aspect ratio AR of the shell, as it is evident from the table of Fig. 3.27 b). Once again, the core size seems to play a major role. For instance, small core DR76 are not polarized, despite their huge AR, while large core DR24 are very well polarized, even if the have a quite low $AR = 2.6$.
However, all the ARs considered here are much larger than 1.5-2, the critical value for a transition from a 2D dipole emission to a linear 1D dipole emission, suggested in [27] for nano-rods.
On the other hand, we found a correlation between p and the average lifetime t_{avg}, as shown in Fig. 3.27 c). This suggests that the electronic structure of the CdSe core, and especially the fine structure due to the hole state degeneracy, must play a main role, as well as the electron wavefunction delocalization.

In the conclusion of section 3.5 we gave an interpretation of the behavior of the lifetime from one sample to another and within a certain sample of DRs, based on the transition from a prevalently type-I (localization of the electronic wavefunction into the DR core) to a prevalently type-II (partial delocalization of the wavefunction into the shell).
The results of the polarization measurements are coherent with such a picture, where type-I nano-structures like DR42 are more polarized than type-II like DR76, and the transition between these two cases is gradual. Like for the lifetime, the length of the shell, given the same thickness and core diameter (d=3.3nm), can only slightly change the degree of polarization, see DR22, DR23 and DR26. This effect is probably associated with a change of the internal electric field, due to the larger surface or to a higher interfacial strain, or with a better dielectric confinement or with a waveguide effect, due to the shell anisotropy.
DR24 are an exception: even if their lifetime is long they show a high degree of polarization. This observation corroborates the hypothesis that DR24 are prevalently type-I because of their large core dimension and that their long lifetime is mainly due to the thickness of the shell.

Conclusions and perspectives In this section we performed single particle measurements of the degree of linear polarization in different samples of DRs. Most of the DRs, except DR76, are quite well polarized, in particular $50 < p < 60\%$ for non blinking DR22 , DR23 and DR26. This is a good result for their application as polarized single photon emitters. We want to underline that p could be further increased, by using a lower NA objective.

Like for the lifetime measurements, also the polarization properties in DRs seem to be mainly determined by the core size. Our results suggest that the degree of polarization in DRs depend on the electron wavefunction delocalization: type-I structures are expected to generate better polarized photons. This is an orginal result, even if its physical reason is not clear yet. In fact, many previous works suggested that a separation between the carriers should lead to a better degree of polarization [27] [16] [17]. We can argue that the electron delocalization is not a

sufficient condition, because the elctronic wavefunction could be just symmetrically distributed around the core, like in spherical CdSe/CdS nanocrystals [39], and no linear polarization is emitted in this case. Moreover, according to the model of the envelope function described in chapter 1, the band-edge electron should always have a s-simmetry. The calculations for CdSe nano-rods and prolate quantum dots suggest that the fine structure is dominated by the degeneracy of the p-type hole orbitals. The hole ground state is mainly determined by the dot shape factor, and it is thought to be responsible for the observed degree of polarization.
According to these considerations, we can speculate that, in the case of DRs, a small core (DR76) is nearly spherical, while a larger core (DR24) could be more prolate.
However, it is not clear yet if there is a sharp transition from 2D dipoles to 1D dipoles or if the passage is more gradual, and, if there is such a transition, when it occurs and why.

Given the large dispersion of p values, a larger statistics would be necessary to correlate the degree of polarization of each single nanocrystal to their lifetime by means of a model, as we have done for $g^{(2)}(0)$ and lifetime. Such analysis could confirm a correlation between the electron delocalization and the degree of polarization. This could be an important achievement in the field of DRs.

Moreover, we did not study yet the polarization properties of the absorption: in all the measurements, DRs are excited by means of a circularly polarized laser beam at 405 nm. Studying the absorption at different wavelength can hopefully provide more informations about the role of the core and of the shell on the fine structure of the fundamental transition.
Also, polarization measurement as a function of the temperature could help to separate the contribution of the electronic structure from that of the geometrical factors, which should not depend on the temperature.

Bibliography

[1] A.I. Ekimov et Al., *Quantum size effect in semiconductor microcrystals*, Solid State Comm. 56, 921 (1985)

[2] C. B. Murray et Al., *Synthesis and characterization of nearly monodisperse Cde (e = s, Se, Te) semiconductor nanocrystallites*, J. Am. Chem. Soc., 115(19) 87068715 (1993)

[3] S. Coe et Al., *Electroluminescence from single monolayers of nanocrystals in molecular organic devices*, Nature 420, 800803 (2002).

[4] M.E. Akerman et Al., *Nanocrystal targeting in vivo*, Proc. Natl. Ac. Sci. USA 99, 1261712621 (2002)

[5] M. Dahan et Al., *Diffusion dynamics of glycine receptors revealed by single quantum dot tracking*, Science 302, 442 (2003)

[6] S. Kim et Al., *Near-infrared fluorescent type II quantum dots for sentinel lymph node mapping*, Nature Biotechnology 22, 9397 (2004)

[7] V. Klimov et Al., *Optical gain and stimulated emission in nanocrystal quantum dots* Science 300, 1434 (2000)

[8] P. Lodahl et Al., *Controlling the dynamics of spontaneous emission from quantum dots by photonic crystals*, Nature 430, 654657 (2004)

[9] D. V. Talapin et Al., Chem. Rev., 110, 389 (2010)

[10] H. Kimble et AL., *Photon antibunching in resonance fluorescence*, Phys. Rev. Lett. 39, 691 (1977)

[11] B. Lounis and W. E. Moerner, *Single photons on demand from a single molecule at room temperature* Nature 407, 291 (2000)

[12] R. Brouri et Al. , *Photon antibunching in the fluorescence of individual color centers in diamond*, Optics letters 25, 1294 (2000)

[13] S. Kako et Al., *A gallium nitride single-photon source operating at 200 K*, Nature materials 5, 887892 (2006)

[14] Efros A. *Luminescence polarization of CdSe microcrystals*, Physical Review B 46, 7448 (1992).

[15] Empedocles S. et Al., *Three-dimensional orientation measurements of symmetric single chromophores using polarization microscopy*, Nature 399, 126 (1999).

[16] Carbone L. et Al, *Synthesis and Micrometer-Scale Assembly of Colloidal CdSe/CdS nano-rods Prepared by a Seeded Growth Approach*, Nano Letters, 7, 2942, (2007)

[17] Pisanello F. et Al., *Room temperature-dipole like single photon source with a colloidal dot-in-rod*, Applied Physics Letters, 96, 033101 (2010).

[18] P. Michler et Al., Science 290, 2282 (2000)

[19] M.Nirmal et Al., Nature 383, 802 (1996)

[20] S.A. Empedocles, Phys. Rev. Lett. 77, 3873 (1996)

[21] B. Malher et Al., Nat. Mater. 7, 659 (2008)

[22] Krahne R. et Al., *Physical properties of elongated inorganic nanoparticles*, Physics Reports, 501, 75 (2011).

[23] Moreels I., *Band-Edge Exciton Fine Structure of Small, Nearly Spherical Colloidal CdSe/ZnS Quantum Dots*, ACS Nano, vol 5, n. 10, 8033 (2011).

[24] Efros A.L. et Al., *Band-edge exciton in quantum dots of semiconductors with a degenerate valence band: Dark and bright exciton states*, Physical Review B, 54, 4843

(1996).

[25] Katz D. et Al., *Size-Dependent Tunneling and Optical Spectroscopy of CdSe Quantum Rods*, Physical Review Letters, vol. 89, n. 8, (2002).

[26] Le Thomas N. et Al., *Exciton Fine Structure in Single CdSe nano-rods*, Physical Review Letters, 94, art. n. 016803 (2005).

[27] Hu J. et Al., *Linearly Polarized Emission from Colloidal Semiconductor Quantum Rods*, Science, vol 292, (2001).

[28] Shabaev A. et Al., *1D Exciton Spectroscopy of Semiconductor nano-rods*, Arxiv (2004)

[29] Van de Hulst H.C., *Light scattering by Small particles*, Dover, New York (1981)

[30] Leatherdale C.A. et Al., *On the absorption cross section of CdSe nanocrystals quantum dots*, Journal of Physical Chemistry B, 106, 7619, (2002).

[31] Li X.Z., Physical Review B, 66 (2002).

[32] Reiss P., *core/shell semiconductor nanocrystals*, Small, n. 2, 154, (2009).

[33] Hines M.A. et Al., Journal of Physical Chemistry, 100, 468-471, (1996).

[34] Peng X., *Epitaxial Growth of Highly Luminescent CdSe/CdS core/shell Nanocrystals with Photostability and Electronic Accessibility*, Journal of the American Chemical Society, 119, 7019, (1997).

[35] Steiner D. et Al., Nano Letters, 8, 2954 (2008).

[36] Börnstein L., *Numerical Data and Functional Relationship in Science and Technology*, New Series, Group III, edited by K. H. Hellwege, vol. 17, Pt. B Springer, New York (1982).

[37] Li J. et Al., Applied Physics Letters, 84, 3648 (2004).

[38] Borys N. et Al., Science, 330, 1371 (2010).

[39] Garcia-Santamaria F. et Al., *Suppressed Auger Recombination in Giant Nanocrystals Boosts Optical Gain Performance*, Nano Letters, 9 (10), 3482-3488 (2009).

[40] Talapin D.V. et Al., Nano Letters, 3, 1677 (2003).

[41] Rossi M.Z., Nanoscale, 2, 931 (2010).

[42] Rainó G., *Probing the wavefunction delocalization in CdSe/CdS Dot-in-rod nanocrystals by time and temperature resolved Spectroscopy*, ACS Nano, 5 (5), 4031-6 (2011).

[43] Rainó G., *Controlling the exciton fine structure splitting in CdSe/CdS DR nanojunctions*, ACS Nano , vol. 6, n. 3 (2012).

[44] Garcia-Santamaria F., *Breakdown of volume scaling in auger recombination in CdSe/CdS Heteronanocrystals: the role of the core/shell interface*, Nano letters, 11, 687-693 (2011).

[45] Rossi M.Z., *Suppression of Biexciton Auger Recombination in CdSe/CdS Dot/Rods: Role of the Electronic Structure in the Carrier Dynamics*, Nano Letters, 10, 3142-3150 (2010).

[46] Sitt A. et Al., *Multiexciton Engineering in seeded core/shell nano-rods: transfer from type-I to type-II regimes*, Nano Letters, vol. 9, n. 10, 3470 (2009).

[47] Müller J. et Al., *Wave Function Engineering in Elongated Semiconductor Nanocrystals with Heterogeneous Carrier Confinement*, Nano Letters, 5 (10), 2044-2049 (2005).

[48] Müller J., *Monitoring surface charge migration in the spectral dynamics of single CdSe/CdS nanodot/nano-rod heterostructures*, Physical Review B, 72, 205339 (2005).

[49] Morello, *Intrinsic optical non-linearity in colloidal seeded growth CdSe/CdS nanostructures: Photoinduced screening of the internal electrical field*, Physical Review B, 78, 19513 (2008).

[50] Sitt A. et Al., *Highly Emissive Nano Rod in-Rod Heterostructures with Strong Linear Polarization*, Nano Letters, 11, 2054 (2011).

[51] Klimov V., Science, 287, 1011-1013 (2000).

[52] Efros A., *Auger Processes in Nanosize Semiconductor Crystals*, Arxiv (2002).

[53] Robel I., Physical Review Letters, 177404, (2009).

[54] Smith A.M. et Al., *Semiconductor Nanocrystals: Structure,Properties, and Band Gap Engineering*, Account of Chemical Research, vol. 43, n. 2, 190 (2010).

[55] Luo Y. et Al., *Electronic Structure of the CdSe/CdS core/shell nano-rods*, ACS Nano, vol 4, n. 1, 91 (2010).

[56] Chen Y. et Al., Journal of the American Chemical Society, 130 , 5026 (2008).

[57] Mahler B. et Al., Nature Materials, 7, 659 (2008).

[58] Talapin, D. V. et Al., *Seeded Growth of Highly Luminescent CdSe/CdS Nano-Heterostructures with Rod and Tetrapod Morphologies*, Nano Letters, 7 (10), 2951 (2007).

[59] Peng X. et Al., *Shape control of CdSe nanocrystals*, Nature, vol. 404 (2000).

[60] Cordones A. et Al., *Mechanisms for charge trapping in single semiconductor nanocrystals probed by fluorescence blinking*, Chemical Society Reviews, DOI: 10.1039/c2cs35452g (2013).

[61] Frantzuzov P., *Universal emission intermittency in quantum dots, nano-rods and nanowires*, Nature Physics, vol. 4 (2008).

[62] Nirmal M. et Al., Nature, 383, 802 (1996).

[63] Efros A.L. et Al., Physical Review Letters, 78, 1110 (1997).

[64] Frantsuzov P.A. et Al., Physical Review Letters, 103, 207402 (2009).

[65] Galland C., *Two types of luminescence blinking revealed by spectroelectrochemistry of single quantum dots*, Nature, 479, 203 (2011).

[66] Gomez D.E., *Optical properties of single semiconductor nanocrystals*, Chemical Physics, 8, 4989 (2006).

[67] Qin W., *Evidence for the Role of Holes in Blinking: Negative and Oxidized CdSe/CdS Dots*, ACS Nano, 6, 9125 (2012).

[68] Hohng S. et Al., *Near-Complete Suppression of Quantum Dot Blinking in Ambient Conditions*, Journal of the American Chemical Society, 126, 1324 (2004).

[69] Jeong S. et Al., *Effect of the thiol-thiolate equilibrium on the photophysical properties of aqueous CdSe/ZnS nanocrystal quantum dots*, Journal of the American Chemical Society, 127, 10126-7 (2005).

[70] Early K.T. et Al, *Blinking suppression and intensity recurrences in single CdSe-oligo(phenylene vinylene) nanostructures : experiment and kinetic model*, Nanotechnology, 18, 424027 (2007).

[71] Fomenko V. et Al., *Solution Control of Radiative and Nonradiative Lifetimes : A Novel Contribution to Quantum Dot Blinking Suppression*, Nano Letters, 8, 287 (2008).

[72] Chen Y. et Al., Journal of the American Chemical Society, 130 , 5026 (2008).

[73] Mahler B. et Al., *Towards non-blinking colloidal quantum dots*, Nature Materials 7, 659 (2008).

[74] Wang X. et AL., Nature, 459 , 686 (2009).

[75] Park Y.S. et Al., Physical Review Letters, 106 , 187401 (2011).

[76] Buil S. et Al., Journal of Physics B: Atomic, Molecular and Optical, 42, 114003 (2009).

[77] Zhao J. et Al., Nano Letters, 12, 4477 (2012).

[78] Jin S. et Al., *Suppressed blinking dynamics of single QDs on ITO*, ACS Nano, 4, 1545 (2010).

[79] Zhao J. et Al., *Challenge to the charging model of semiconductor-nanocrystal fluorescence intermittency from off-state quantum yields and multiexciton blinking*, Physical Review Letters, 104, 157403 (2010).

[80] Rosen S. et Al., *Transient fluorescence of the off state in blinking CdSe/CdS/ZnS semiconductor nanocrystals is not governed by Auger recombination*, Physical Review Letters, 104, 157404 (2010).

[81] Galland C., *Lifetime blinking in nonblinking nanocrystal quantum dots*, Nature Communications, 3:908, DOI: 10.1038/ncomms (1916).

[82] Santamaría F.G., *Breakdown of Volume Scaling in Auger Recombination in CdSe/CdS Heteronanocrystals: The Role of the core/shell Interface*, Nano Letters, 11, 687-693 (2011).

[83] Zhao, *Biexciton QY heterogenities and correlations to exciton QY blinking*, Nano letters (2012).

[84] Kharchenko V.A. et Al., *Auger relaxation processes in semiconductor nanocrystals and quantum wells* , Journal of Luminescence, 70, 158-169 (1996).

[85] Califano, *Hole Surface Trapping in CdSe Nanocrystals: Dynamics, Rate Fluctuations, and Implications for Blinking*, Nano Letters, dx.doi.org/10.1021/nl3016279, 12, 4508-4517 (2012).

[86] Zhang K. et Al., *Continuous Distribution of Emission States from Single CdSe/ZnS Quantum Dots*, Nano Letters, 6, 843 (2006).

[87] Fisher B.R. et Al., *Emission Intensity Dependence and Single-Exponential Behavior in Single Colloidal Quantum Dot Fluorescence Lifetimes*, Journal of Physical Chemistry B, 108, 143 (2004).

[88] Jha P.P. et Al, *Trion decay in colloidal quantumdots*, ACS Nano, 3, 1011 (2009).

[89] Spinicelli P., *Bright and Grey States in CdSe-CdS Nanocrystals Exhibiting Strongly Reduced Blinking*, Physical Review Letters, 102, 136801 (2009)

[90] Gomez D.E. et Al., *Exciton to trion transitions in single CdSe/CdS core/shell nanocrystals*, ACS Nano 3, 2281 (2009).

[91] Krauss S. et Al., *Polarizability, and Photoionization of Single Semiconductor Nanocrystals*, Physical Review Letters, 84, 1638 (2000).

[92] Thomas N.L. et Al., Applied Physics Letters, 89, art. n. 263115 (2006).

[93] Kambhampati P.J., Journal of Physical Chemistry C, 115, 22089-22109 (2011).

[94] Campos F.G., *Hole Surface Trapping in CdSe Nanocrystals: Dynamics, Rate Fluctuations, and Implications for Blinking* , Nano Letters, 12, 4508-4517 (2012).

[95] Fleury L. et Al., Physical Review Letters, 84, 1148 (2000).

[96] Efros A.L. et Al., *Random Telegraph Signal in the photo-luminescence Intensity of a Single Quantum Dot*, Physical Review Letters, 78, 1110 (1997),

[97] Messin G., *Bunching and antibunching in the fluorescence of semiconductor nanocrystals*, Optics Letters, vol. 26, n. 23 (2001).

[98] Kuno M. et Al., *Nonexponential blinking kinetics of single CdSe quantum dots: A universal power law behavior*, Journal of Chemical Physics, 112, 3117 (2000).

[99] Crouch C.H. et Al., Nano Letters, 10, 1692S (2010).

[100] Lounis B., Chemical Physics Letters, 329, 399 (2000).

[101] Michler P., Nature, 406, 968 (2000).

[102] Klimov V.I., Science, 287, 1011 (2000).

[103] Brokmann X., Applied Physics Letters, 85, 712 (2004).

[104] Fisher B., *Room-Temperature Ordered Photon Emission from Multiexciton States in Single CdSe core/shell Nanocrystals*, Physical Review Letters, 94, 087403 (2005).

[105] Nair G., *Biexciton Quantum Yield of Single Semiconductor Nanocrystals from Photon Statistics*, Nano Letters, 11, 1136 (2011).

[106] Yamamoto Y., *Single photon sources for quantum information systems*, Progress in Informatics, n. 1 (2005).

[107] Gerry C. et Al., *Introductory Quantum Optics*, Cambridge University Press (2005).

[108] Verberk R. et Al., *Photon statistics in the fluorescence of single molecules and nanocrystals: Correlation functions versus distributions of on- and off-times*, Chemical Physics, vol. 119, n. 4 (2003).

[109] Müller M., *Introduction to Confocal Fluorescence Microscopy, SPIE-The International Society for Optical Engineering*, Bellingham, Washington, 2nd edn (2006).

[110] Becker W., *Advanced Time-Correlated Single Photon Counting Techniques*, Springer-Verlag, Berlin Heidelberg, Germany (2005).

[111] Pisanello F. et Al., *Non-blinking single photon generation with anisotropic colloidal nanocrystals: towards room-temperature efficient colloidal quantum sources*, Advanced Materials 25, 1974 (2013).

[112] Carbone L. et Al., Nano Today, 5, 449 (2010).

[113] Yu W.W. et Al, *Experimental Determination of the Extinction Coefficient of CdTe, CdSe, and CdS Nanocrystals*, Chemistry of Materials, 15, 2854 (2003).

[114] Lukosz W., *Light emission by magnetic and electric dipoles close to a plane dielectric interface. III. Radiation patterns of dipoles with arbitrary orientation*, Journal of the Optical Society of America, 69, 1495 (1979).

[115] Brokmann X., *Proprietes de fluorescence de nanocristaux de CdSe individuels*, PhD Thesis (2004).

[116] Biebricher A. et Al., Journal of Physical Chemistry B, 110, 5174-5178 (2006).

[117] Hartmann L. et Al., ACS Nano, 6, 9033 (2012).

[118] Van Sark W. et Al., ChemPhysChem, 3, 871 (2002).

[119] Muller J. et Al., *Air-induced fluorescence bursts from single semiconductor nanocrystals*, Applied Physics Letters, 85, n. 3, 381 (2004).

[120] Xu X. et Al., Applied Physics B, 94, 577 (2009).

[121] Forster T., Naturwissenschaften, 33, 166 (1946).

[122] Wen X., *Studies of the photostability of CdSe/CdS dot-in-rod nanoparticles*, Journal of Nanoparticles Research, 14, 1278 (2012).

[123] Guo. W.H., Journal of the American Chemical society, 125, 3901 (2003).

[124] Vezzoli S., Optics Communications, 300, 215 (2013).

[125] McGuire J.A. et Al., *New aspects of carrier multiplication in semiconductor nanocrystals*, Accounts of Chemical Research, 41, 1810-1819 (2008).

[126] Klimov V.I. et Al., *Scaling of multiexciton lifetimes in semiconductor nanocrystals*, Physical Review B, 77, 195324 (2008).

[127] Ware W.R., in *Photochemistry in Organized and Constrained Media*, VCH Publishers Inc., New York (1991).

[128] Schlegel G., *Fluorescence Decay Time of Single Semiconductor Nanocrystals*, Physical Review Letters, vol. 88, n. 13 (2002).

[129] Spinicelli P., Physical Review Letters, 102, 136801 (2009).

[130] Bohmer M. et Al., Journal of the Optical Society of America B, vol. 20, n. 3 (2003).

[131] C. Lethiec et Al., *Three-dimensional orientation measurement of a single fluorescent nanoemitter by polarization analysis*, arXiv:1301.4063v1 (2013)